

# **Viscoelasticity at Microscopic and Macroscopic Scales: Characterization and Prediction**

by  
Lingxing Yao

A dissertation submitted to the faculty of the University of North Carolina at Chapel Hill in partial fulfillment of the requirements for the degree of Doctor of Philosophy in the Department of Mathematics.

Chapel Hill  
2007

Approved by:

M. Gregory Forest, Advisor

Sorin M. Mitran, Advisor

Timothy C. Elston, Committee Member

Richard McLaughlin, Committee Member

Ruhai Zhou, Committee Member

© 2007  
Lingxing Yao  
ALL RIGHTS RESERVED

# Abstract

**LINGXING YAO: Viscoelasticity at Microscopic and Macroscopic Scales:  
Characterization and Prediction.**

**(Under the direction of M. Gregory Forest and Sorin M. Mitran.)**

In this dissertation, we build mathematical tools for applications to the transport properties of human lung mucus.

The first subject is the microscopic diffusive transport of micron-scale particles in viscoelastic fluid. Inspired by the technique of passive microrheology [58], we model the motion of Brownian beads in general viscoelastic fluids by the generalized Langevin equation (GLE) with a memory kernel (the diffusive transport modulus). The GLE is a stochastic differential equation, which admits a discrete formulation as an autoregressive (AR) process. We further use exponential series for the memory kernel in the GLE, in which case the GLE has an explicit formulation as a vector Ornstein-Uhlenbeck process. In this framework, we can develop fast and accurate direct algorithm for pathogen transport in viscoelastic fluids, and the Kalman filter and maximum likelihood method give a new method for inversion of the memory kernel from experimental position time series. The framework is illustrated with multimode Rouse and Zimm chain models.

In the second topic, we revisit the classical oscillatory shear wave model of Ferry *et al.* [23], and extend the theory for active microrheology of small volume samples of viscoelastic fluids. In Ferry's original setup, oscillatory motion of the bottom plate generates uni-directional shear waves propagating in the viscoelastic fluid. Our colleague David Hill built a device to handle small volume viscoelastic samples. We extend the Ferry analysis to include finite depth and wave reflection off the top plate. We further consider nonlinear viscoelastic constitutive laws.

The last problem considered is the numerical simulation of viscoelastic fluid flow, which will eventually be used to predict bulk transport of mucus layers. We start with the analysis of the system of model equations and demonstrate the difficulty of a robust numerical scheme. We develop an extension of projection method, which involves a new

treatment of stress evolution based on stress splitting in the numerical scheme and show the advantage over previous work.

# Acknowledgments

I would like to express my deep gratitude to my advisor Dr. M. Gregory Forest who introduced me into the world of complex fluids and always helps me with his deep insight to the problems. Without his kind help and support, this dissertation would not have been possible. I also want to thank my co-advisor Dr. Sorin M. Mitran for his useful suggestions and all the inspiring discussions with him. Working with him benefits my research in many ways. My special thanks also go to Dr. Timothy C. Elston, whose instructive and stimulating suggestions are always of great help to me, and it is a great pleasure to learn from him and work with him.

I am very grateful to Dr. John Fricks of Penn State University for all the discussions we have had and what I learned from him through our collaboration. Dr. Ruhai Zhou of Old Dominion University helped me a lot when I started my research on soft matters and he always encourages me to work on challenging problems.

Faculty members in the UNC applied mathematics program are very helpful and friendly to me, and I want to express my appreciation to them: Dr. Richard M. McLaughlin and Dr. Roberto Camassa helped me to understand fluid problems better and I have enjoyed the discussions with them. Dr. Jingfang Huang is always kind and helpful in answering my questions and giving me useful suggestions. Dr. David Adalsteinsson has been always a good resource for me in solving the computing problems on MAC.

I also would like to thank the staff in the Mathematics Department, specially Brenda Beatha for her unfailing assistance throughout my graduate years.

My friends at the Department of Mathematics have always offered a friendly atmosphere and I am really happy for those years of study.

I thank my parents for their continuous and unconditional support of all my undertakings. And finally I want to thank my wife, Longhua, who has always supported me with her caring, encouragement and love.

# Table of Contents

<b>Abstract</b>	<b>iii</b>
<b>List of Figures</b>	<b>viii</b>
<b>1 Introduction: basic concepts and methodology</b>	<b>1</b>
1.1 Motivation: the Virtual Lung Project . . . . .	3
1.2 Fundamentals of viscoelasticity . . . . .	5
1.3 Proposals at micro and macro scales . . . . .	8
1.3.1 Small length scale problem . . . . .	8
1.3.2 Study of bulk properties . . . . .	11
<b>2 Microscopic scale: the Microrheology in time domain</b>	<b>13</b>
2.1 Viscous model: Langevin equation . . . . .	16
2.1.1 Solution to Langevin equation . . . . .	16
2.1.2 Discrete Langevin equation : AR representation . . . . .	18
2.1.3 Full system of position & velocity . . . . .	19
2.2 Brownian particle in viscoelastic media . . . . .	20
2.2.1 Generalized Langevin equation . . . . .	21
2.2.2 Fluctuation-Dissipation theory . . . . .	22
2.2.3 Reformulation of the GLE . . . . .	23
2.2.4 Analysis on the covariance matrix $S$ . . . . .	27
2.3 Direct simulation: theory and examples . . . . .	30
2.3.1 Numerical calculation of correlation function . . . . .	30
2.3.2 Example of Rouse and Zimm chain models . . . . .	32
2.4 Inversion based on the GLE formulation . . . . .	35
2.4.1 The MLE method on the velocity of Langevin equation . . . . .	35

2.4.2	Kalman filter for systems including positions . . . . .	38
2.5	Comparison between MLE and M-W framework . . . . .	41
<b>3</b>	<b>Shearwave modeling and computation</b>	<b>46</b>
3.1	Shear wave models . . . . .	47
3.1.1	Stokes second problem . . . . .	49
3.1.2	Shear wave model in linear viscoelastic fluids . . . . .	50
3.1.3	Upper Convected Maxwell and Giesekus models . . . . .	51
3.2	Analytical results . . . . .	53
3.2.1	Solution to the viscous problem . . . . .	53
3.2.2	Solution to linear viscoelastic problems . . . . .	54
3.3	Solutions to nonlinear model at special limits . . . . .	60
3.3.1	Hyperbolic structure . . . . .	60
3.3.2	Characteristic boundary conditions . . . . .	62
3.3.3	Upper Convected Maxwell solution . . . . .	65
3.4	High resolution numerical computation . . . . .	66
3.4.1	Numerical scheme . . . . .	66
3.4.2	Experimental design guidelines . . . . .	68
<b>4</b>	<b>Numerical simulation at continuum level</b>	<b>73</b>
4.1	Viscoelastic fluid flow models . . . . .	74
4.1.1	Note on viscous case . . . . .	75
4.1.2	Constitutive law for extra stress . . . . .	76
4.1.3	Current numerical scheme and the difficulty . . . . .	79
4.2	Extension of the projection method for viscoelastic fluid flows . . . . .	81
4.2.1	System of model equations . . . . .	81
4.2.2	Gauge formulation . . . . .	83
4.3	Analysis on extra stress and the new numerical scheme . . . . .	89
4.3.1	Stress tensor decomposition . . . . .	90
4.3.2	Numerical scheme based on the stress decomposition . . . . .	92
4.3.3	Analysis on the FENE-P model . . . . .	93
<b>5</b>	<b>Conclusions</b>	<b>97</b>
	<b>Bibliography</b>	<b>100</b>

# List of Figures

2.1	Comparison on MSD of GLE model with different number of memory modes: effect of superposition of modes . . . . .	34
2.2	Scaling for MSD of the GLE model with 22 modes Zimm kernel: different power law behavior . . . . .	36
2.3	MSD of sample paths by GLE model with 4 modes Rouse model . . . .	40
2.4	Storage and loss moduli results of different number of exponential modes	43
2.5	Comparison on complex modulus recovered by M-W and MLE method	44
2.6	Comparison of shear relaxation modulus and relaxation time recovered by M-W and MLE method . . . . .	45
3.1	Shear wave model setup . . . . .	47
3.2	Schematic sketch of asymmetric lower boundary condition for velocity, with effect of net shift to the right showed . . . . .	64
3.3	Numerical results of symmetric lower boundary condition . . . . .	69
3.4	Numerical results of the asymmetric lower boundary condition, and stationary top plate boundary condition . . . . .	71
3.5	Numerical results with the asymmetric lower boundary condition and the open-cell top boundary condition . . . . .	72
4.1	Dumbbell model . . . . .	77
4.2	Cavity simulation for Oldroyd-B model . . . . .	87
4.3	Cavity simulation for Oldroyd-B model (continue) . . . . .	88



# Chapter 1

## Introduction: basic concepts and methodology

The main concerns of this thesis surround the rheology of human lung mucus. The research presented here has arisen from the Virtual Lung Project (VLP) in UNC, whose long term goal is [33]: *to develop an integrated computational model that will be able to predict and evaluate truly effective therapeutic strategies*. The specific topics addressed are: (1) bulk rheological characterization; (2) diffusive transport of pathogens; and (3) bulk hydrodynamic transport.

Human lung mucus covers and protects most of the airway surface in the lung. The mucus layer is transported in healthy humans by coordinated cilia, and in compromised situation, by cough. The clearance of pathogen trapped in mucus is a critical defense mechanism of the lung system. The three topics addressed in this thesis contribute to the overall predictive goal of the VLP, namely to model the simultaneous flow of the mucus layer and the diffusion of pathogens inside the mucus layer.

One of the key points in the study of lung system is that the length scales of the objects vary from micron/nano meter to centimeter. Even a focus on just mucus layer presents multi scale challenges. As a consequence of this complexity of structure, the rheological properties manifest different characterization at corresponding scales and then request proper treatments based on those features. For the main subjects we want to address: the stochastic characterization of diffusion of pathogen in mucus layer makes the tools of statistical analysis more plausible; and the clearance of mucus layer

of human lung, will be likely better modeled by the hydrodynamic transport equations coupled with bulk constitutive laws of polymeric system.

According to the fact of scale dependence, we are trying to identify our targets at micro and macro scales, and then present the corresponding statistical and deterministic methods. At microscopic scale, Mason and Weitz [58] initiated the passive microrheology protocol to measure the complex modulus with micron size beads embedded in material as tracers. Mason and Weitz's method (M-W method) was originally intended to infer bulk viscoelastic properties from diffusive fluctuations of tracer beads. This was later realized to be problematic, since a probe particle will modify the local environment depending on chemical interactions of the viscoelastic media. Hence, the method is ideal for studying diffusive properties, one of the key issues in human lung defense. As proposed by Forest and Elston [26], we start the study from the dynamics of single bead in complex fluid and model the randomness of the material response with prescribed stochastic process, the formulation will help us set up framework that allow us do easy inversion based on time evolution of bead positions and then reveal the local environment detected by the beads, and we also get fast and stable direct prediction based on those information we collect. The deterministic information, or say ensembles average, could also be calculated easily [26].

Inversion of rheological property in controlled experiments is always important in the characterization of viscoelasticity. Our colleagues (D. Hill and Richard Superfine from VLP) build micro, parallel-plate rheometer, and use bead tracking to measure shear wave propagation features. We then study the active microrheology of the experiment of the device. We note the problem we are faced is small volume samples of viscoelastic fluids, and special care should be taken for the finite dimension. We revisit the classical oscillatory shear wave model of Ferry *et al.* [23, 1], and extend it to include the effect of finite depth within linear viscoelasticity and then to include the nonlinearity with nonlinear constitutive laws.

The last topic we treat here is the transport of the mucus layer itself. Due to the highly elastic effect from polymeric intergradient of mucus, the transport show strong non-Newtonian (viscoelastic) signatures. For numerically solving the non-newtonian behavior of the mucus flow, it is very important to cast proper numerical scheme to fully resolve the system. There are lots of previous works on the issue of numerical study of viscoelastic transport (cf. [67], there is a nice summary about numerical schemes proposed), and they all face difficulty of getting stable results for high Weissenberg

number fluid flow. We present a new scheme which handles the time evolution of velocity profile together with stress growth based on the correct physical interpretation of stress components, and we treat the update of the whole system physically and expect the better performance of our new method. We will show the numerical results to verify our proposals.

In the Introduction, we present the basic background and give the fundamental concepts. In Chapter 2, we review the passive microrheology and present our treatment of microscopic diffusion in viscoelastic materials based on the generalized Langevin equation model. In Chapter 3, we focus on inverse methods to determine bulk rheological properties of the mucus layer, based on an extension of Ferry’s classical shear wave experiment [24] to finite depth and nonlinearity. In Chapter 4, we give a new numerical scheme based on a proper treatment of the elastic stress in a canonical nonlinear model of viscoelastic flow. We conclude in Chapter 5 with a list of current and future projects.

## 1.1 Motivation: the Virtual Lung Project

The discussion in this section is based on the UNC Virtual Lung Project (VLP) [33].

The lung system behaves as the interface for the air and human body: it inhales air and then exchanges oxygen. During breathing, various foreign objects including bacteria, viruses, and dust particles enter and must be cleared. Pathogens are usually trapped by lung mucus and cleared by mucus transport. Between the mucus layer and the lung tissue, periciliary liquid (PCL) lies, which serves as a bathing solution for the cilia.

From the above description, we see it is critical to keep lung system functional and healthy. But there are some diseases causing failure of mucus transport and increase the probability for people of getting infections. Cystic fibrosis (CF) is one kind of genetic diseases that makes patients’ cilia lose functionality and prevents cilia development. Without functional cilia, mucus transport in lung system will be very difficult and the defense functionality of lung system is greatly jeopardized. Traditional treatment for cystic fibrosis patients focus on the modification of transport properties of the ASL to speed up the mucus clearance. The VLP aims to develop a computational model to

the efficiency of drugs delivery, and the improvement on therapeutic treatment for CF patients' pulmonary system. For example, the model of the transport of drugs through the airway surface liquids (mucus and PCL) by diffusive and advective processes will make a better understanding of drug delivery in lung available and help to improve the drug efficiency by a better prediction of diffusive behavior of drugs.

In human mucus, the diffusive transport properties are greatly affected by different types of biological macromolecules, which are usually called mucin. Those high dispersity and high molecular weight bio-polymers contribute to the elastic properties of the mucus and make the thin mucus layer viscoelastic in nature. So the model of diffusive transport of small particles in the mucus layer demands the capability describing diffusion in complex material. We will use the first part of this manuscript to present the method we proposed for this model problem. And we note here that the model we set up is capable of modeling viscoelastic diffusion and presents easy inversion on the parameters that are required to reconstruct diffusive properties.

For the mucus clearance, hydrodynamic transport is very important. We know one driving source is from epithelial cilia which grow on the surface of living cells and are immersed in the PCL layer, which is low viscosity fluid. Those thousands of cilia are about  $7\mu m$  long and beat in a frequency of  $10 \sim 15\text{Hz}$ . Single cilium beating costs biological energy (ATP) and forms fast stroke and slow relaxation cycle during one period of beat. When the beating of large amount of cilia synchronizes, the collective motion forms a *metachronal* wave with much longer wave length than cilia height at the bottom of mucus layer and supply the primary driving source to the mucus transport. At the current stage of research progress, the details of momentum or stress communication between cilia and mucus movement remain quite primitive, i.e., the boundary conditions for the mucus and PCL/cilia interface is not fully understood yet. Instead, we focus on a simple problem where the mucus layer is isolated, and we study its flow by virtue of different driving force. These models and codes are used in conjunction with experiments by David Hill and Rich Superfine to first characterize the viscoelastic properties of mucus, and *then* to use those constitutive equations to simulate bulk transport. We note another driving force of mucus clearance is from the air drag induced by cough. The maximal air flow speed of cough could reach meter per second, but the continuous branching of the lung system will significantly reduce the of air speed, and we know this driving is not the primary driving force.

In healthy lung system, the advection transport of mucus is propelled by cilia beat-

ing and air drags, as we mentioned above. Those cilia are immersed in the PCL and the PCL is low viscosity newtonian fluid and makes the beating more effective. Experiments on cell cultures show that the cilia beating generates shear velocity profile in mucus layer and the cilia force exerted on the mucus layer display asymmetric cycle that form metachronal waves and the propulsion force or stress will be transformed to mucus layer. The major difficulty now is that the stress applied by cilia directly on the mucus is not clear due to lack of detail understanding of interaction between cilia tip and mucus layer. Even there are some experimental evidences showing there might be a thin layer ‘lubricant’ underneath mucus layer and above cilia tips, whether the cilia carpet slide under mucus or actually the tips penetrate into the mucus layer is not confirmative. Blake’s [77] contraction layer model will make more sense if the lubricant layer is confirmed. At the moment, it will be wise for us to isolate the model to the motion of the mucus layer itself, and to take reasonable assumption on the stress level exerted by cilia wave to the mucus layer to close the model system. We will take a nonlinear viscoelastic model and computation of the mucus flow phenomena as the second part of the thesis. The full coupling of cilia motion and mucus flow will be our future research topic.

## 1.2 Fundamentals of viscoelasticity

Since the models being applied are all based on the viscoelasticity of the material, we will present basic conceptual pictures in this part of introduction. All the contents of this section are fundamental rheological concepts and can be found in standard rheology textbooks. The restate of those concepts is just for the preparation to the derivation of model later, and the references we are following here are mainly those classics of Bird[7], Ferry[24], Larson[46] and Macoscko[54].

The key feature of viscoelastic materials is their response to the stress/force applied to them. For viscous fluid, we know the shear stress  $\tau$  is proportional to the velocity  $v_x$  (velocity along  $x$  coordinate) gradient, with a constant  $\eta_s$  (viscosity, constant in the sense independent on the velocity or the gradient),

$$\tau_{xy} = \eta_s \frac{dv_x}{dy}. \quad (1.1)$$

We note in viscoelastic materials, the configurations of molecules are much more complicated than in simple viscous fluid, and the dimension of the molecules in viscoelastic fluids are usually very large compared to molecules in simple fluid. While under strain or stress, the change of configuration of those huge macromolecules will store stress and relax. This feature leads to the fact that the response of viscoelastic material to stress depends not only on current deformation state, but also on whole deformation history of the material, and this relation is usually casted as

$$\tau_{xy}(t) = \int_{-\infty}^t G(t-s) \frac{dv_x(s)}{dy} ds, \quad (1.2)$$

where  $G(t)$  describes the dependence of history of deformation and is usually called relaxation modulus, and we can define  $\eta_0$ , the zero shear rate viscosity as

$$\eta_0 = \int_0^{\infty} G(t) dt \quad (1.3)$$

We note  $G(t)$ , determined by viscoelasticity of materials, can be complicated function. And we also see if  $G(t)$  is replaced by Dirac Delta function, e.g.  $G(t) = \eta_s \delta(t)$ , the relation (1.2) is reduced to (1.1), hence the viscous stress is recovered. To better understand this concept, we choose the simple Maxwell model as an illustration. According to the Maxwell model, relaxation modulus  $G(t)$  of the Maxwell material is ( $\lambda$  is the relaxation time)

$$G(t) = G_0 e^{-\frac{t}{\lambda}} \quad (1.4)$$

By taking derivative with respect to time  $t$  on both sides of (1.2), the relation can be written as

$$\frac{d\tau_{xy}}{dt} + \frac{1}{\lambda} \tau_{xy} = G_0 \dot{\gamma} = G_0 \frac{dv_x}{dy}, \quad (1.5)$$

where  $\dot{\gamma}$  is the rate of strain. The equation of (1.5) for Maxwell model defines the evolution of the extra stress component  $\tau_{xy}$ .

In general, the shear modulus is the characterization of the viscoelasticity of materials and can not be assumed as a simple exponential function. The main focus on the modeling of complex fluid is to get the modulus information and other related properties can be derived afterwards. For the purpose of numerical simulation, this modulus

is also important since it defines the relationship between the stress components and the rate of strain, which is the key part for describing the fluid transport. We note that the shear modulus can be approximated by a series of exponential functions with relaxation time,  $\lambda_i$ , and the weighting constants  $G_i$  (the Maxwell modes)

$$G(t) = \sum_{i=1}^N G_i e^{-t/\lambda_i} \quad (1.6)$$

In the experimental side of reality, the transformation signals of  $G(t)$  are more easily measured and then more important. The physical interpretation of the transformation can be explained based on the viscoelastic response to sinusoidal input information. And the formal mathematical definition can be formulated by the unilateral Fourier transformation, and is termed as complex modulus which is the shear modulus information in the frequency domain

$$\begin{aligned} G^*(\omega) &= i\omega \int_0^\infty G(s) e^{-i\omega s} ds = G' + iG'' \\ &= \int_0^\infty \omega G(s) \sin \omega s ds + i \int_0^\infty \omega G(s) \cos \omega s ds \end{aligned} \quad (1.7)$$

in which  $G'(\omega)$  is termed as storage modulus and  $G''$  as loss modulus. And we can also define complex viscosity  $\eta^*$

$$\eta^*(\omega) = \eta' - i\eta'' = \frac{G^*}{i\omega} = \frac{G''}{\omega} - i\frac{G'}{\omega} \quad (1.8)$$

where  $\eta'$  is dynamic viscosity.

Most of the frequency dependent experiments will give us complex modulus at discrete frequency, and for the purpose of simulation of complex fluid flow, we expect to invert those experimental information back to time domain for our model calculation. Currently, the commonly used inversion techniques usually posit formula of shear modulus and fit with unknown time and modulus. For example, the most popular inversion of relaxation spectrum takes the approximation of the series of Maxwell model and the

important complex modulus is

$$G' = \omega \int_0^\infty G(s) \sin \omega s ds \xrightarrow{\text{Maxwell}} \sum_{k=0}^N G_k \frac{\omega^2 \lambda_k^2}{1 + \omega^2 \lambda_k^2} \quad (1.9)$$

$$G'' = \omega \int_0^\infty G(s) \cos \omega s ds \xrightarrow{\text{Maxwell}} \sum_{k=0}^N G_k \frac{\omega \lambda_k}{1 + \omega^2 \lambda_k^2}. \quad (1.10)$$

We should note all the concepts here are at macroscopic state and are used when we present the inversion of viscoelasticity by shear wave model in the thesis.

## 1.3 Proposals at micro and macro scales

### 1.3.1 Small length scale problem

The microscopic structure of material determines the local environment of small particles embedded in the material. For modeling purpose, we assume micron size passive beads embedded in mucus can detect the signal corresponding to the diffusive property at the length of interest, and then we can use tracer particles to refer the fluids information. We want to model the tracer dynamics so we can further predict the diffusion of drug or bacteria in mucus. Instead of dealing with macroscopic rheological problem, the idea of microrheology, introduced by Mason and Weitz, of using thermal fluctuation of tracer embed in complex fluid to infer the rheological property at microscopic scales, is sketched in the following first. And then, inspired by the idea of microrheology, we focus on the simulation and inverse characterization of viscoelastic system at small scales, and propose our tools to microscopic diffusions.

In the model of the diffusion of Brownian particles in viscous fluids, one can think the tiny disturbances to Brownian beads are the collective effects of huge number simultaneous interactions arising from collisions between beads and small molecules of viscous fluid. Naturally, one would assume the random effect can be averaged to a force randomly applied on the tracer by the viscous fluid. Then the motion of Brownian particles is determined by this random driving force and the drag force experienced by the particles. Those two type of forces are actually from the same origin and Einstein



established the their relation with the well known fluctuation dissipation (F-D) relation [13, 40]. We note the mathematical model for Brownian particle is the well known Langevin equation [13, 9].

Following this conceptual picture of molecule collisions, we can expect the behavior of the passive tracer dispersed in complex fluids is more complicated than that of Brownian particles immersed in viscous fluid. We know, in the surrounding environment of beads in complex fluid, there are not only small molecules which apply fast dissipative forces to the tracer, but also some bigger (compared in size to the bead itself) objects which will cause elastic retardation of the bead motion. The immediate consequence is that the drag force on the retarded tracers will not be just proportional to the velocity as in viscous fluid, but usually dependent on the history of the tracer velocity too. The more proper way of describing this erratic motion is proposed long time ago, which is a phenomenological description by the generalized Langevin equation (cf. [41, 40, 92, 13, 29]), with a kernel function representing the memory effect of materials on the bead velocity and a random force modeling the randomly driving sources of the fluid. As analogous to the case of the Brownian motion in viscous fluids, we expect the connection between the random force  $f$  and the memory effect. And at least at or near the equilibrium state, the general fluctuation dissipation (F-D) theorem informs us the correspondence [13, 41, 29].

Starting from the model of the generalized Langevin equation, Mason and Weitz [58, 57] introduced the idea of microrheology. In that theoretical work, they made the assumption that the Stokes-Einstein relation can be extended to all frequency instead of only zero frequency, which is usually referred as the generalized Stokes-Einstein relation. They also ignored the inertia effect of small tracer beads (radius  $a$ ) in the model by arguing the inertia can be neglected as long as the frequency ( $\omega$ ) is not high enough to make the inertia important to their experiments. Together with some causality assumptions on the correlation of force and velocity, they established the correspondence between the complex modulus of the material,  $G^*(\omega)$ , and the unilateral Fourier transformation ( $\mathcal{F}_u$ ) of the mean square displacement (MSD,  $\langle \Delta^2 r(t) \rangle$ ) of passive tracers [58]:

$$G^*(\omega) = \frac{k_B T}{\pi a i \omega \mathcal{F}_u \{ \langle \Delta r^2(t) \rangle \}}, \quad (1.11)$$

where  $k_B$  is the Boltzmann constant and  $T$  is the temperature.

Measurements on positions of thermally passive tracers in viscoelastic fluids can be

ensemble averaged to get the MSD. From the MSD information we can determine the complex modulus thereafter with the relation (1.11). After obtaining complex modulus, the discrete relaxation spectrum in time domain can be obtained by the standard inverse characterization methods developed in bulk rheology. This methodology is quite successful for some applications as they reported in the series of papers [58], but concerns about the applicability to material with heterogeneity and biological system are soon raised[43], and people realize the particle diameter relative to the equilibrium length scales of the polymer solution [85]. For the biological system we are interested in, the way of expressing this situation is that the bead fluctuations reflect the linear viscoelastic moduli of the host soft matter, the bead geometry, and bead-solvent chemical interactions.

When we revisit this microrheology framework from the very beginning, we realize that the generalized Langevin equation is a proper model equation for Brownian motion in viscoelastic materials because it can include the memory effect on velocity retardation in the dynamics of passive tracers. Then the fluctuation dissipation theorem should be the key point of characterizing complex fluid systems since it gives the explicit connection between material property (thermal force of material to the tracer) and the measurable dynamics (tracer trajectories of positions). If we can link model descriptions of the material property and the memory effect based on the underlying law of fluctuation dissipation theorem, we will establish the proper way of connecting material property and measurable dynamics.

Inspired by the passive microrheology idea, we model the motion of Brownian beads (or similar objects) by the generalized Langevin equation and we can choose proper stochastic process to represent the random force. The memory kernel corresponding to the random process will be the determined based on the fluctuation dissipation theorem to close our model system. The parameters defining the stochastic process will also be fitting parameters in the model system to recover the material property.

In this framework, we study the GLE from the point of view of stochastic equation and take it as a representation for time evolution of bead positions. The time series of positions can then be analyzed with powerful statistical tools established for other statistical subjects. Since there are stable and accurate regression tools available, we will get good fitting inversion results in this statistical model. We will explain this idea and focus on the modeling and analysis in the first problem discussed in this dissertation.

### 1.3.2 Study of bulk properties

At continuum level, the hydrodynamic momentum equation governs the motion of fluids

$$\rho\left(\frac{\partial \mathbf{v}}{\partial t} + (\mathbf{v} \cdot \nabla) \mathbf{v}\right) = \nabla \cdot (-p\mathbf{I} + \boldsymbol{\tau}), \quad (1.12)$$

where  $\rho$  is the material density and  $p$  is the hydrostatic pressure.  $\boldsymbol{\tau}$  in (1.12) is the extra stress, which can include viscous and elastic parts and is described by proper constitutive laws according to choices of material models. For experimental and theoretical investigations of complex material, different type of constitutive relations are proposed to capture the characteristics of viscoelasticity, and at macroscopic scale, they are mainly presented either in differential equation form or integral equations. For example, the Oldroyd-B differential constitutive law is defined as

$$\lambda_1 \overset{\nabla}{\boldsymbol{\tau}} + \boldsymbol{\tau} = 2\eta_0(\mathbf{D} + \lambda_2 \overset{\nabla}{\mathbf{D}}), \quad (1.13a)$$

Or the linear integral constitutive law

$$\boldsymbol{\tau}(t) = \int_{-\infty}^t G(t-s) \mathbf{D}(s) ds, \quad (1.13b)$$

where  $G(t)$  is shear modulus. In (1.13a), the convected derivative  $\overset{\nabla}{\boldsymbol{\tau}}$  is defined as

$$\overset{\nabla}{\boldsymbol{\tau}} = \frac{\partial \boldsymbol{\tau}}{\partial t} + (\mathbf{v} \cdot \nabla) \boldsymbol{\tau} - \nabla \mathbf{v} \cdot \boldsymbol{\tau} - \boldsymbol{\tau} \cdot \nabla \mathbf{v}^T, \quad (1.14)$$

and rate of strain tensor  $\mathbf{D}$  is defined as:

$$\mathbf{D} = \frac{1}{2}(\nabla \mathbf{v} + \nabla \mathbf{v}^T). \quad (1.15)$$

With incompressibility constraint  $\nabla \cdot \mathbf{v} = 0$ , equations (1.12) and (1.13a) or (1.12) and (1.13b) will give us complete system for viscoelastic model. And we further note with dimension reduction, the system will be greatly simplified and analyzed in detail. By virtual of the simplification, we will study the shear wave model as a tool of inversion for viscoelastic property and prediction of one dimension transport.

For more general situations, no matter which type of constitutive equations adopted, we have to solve the momentum equation and the evolution equation for extra stress as a whole system, and analytical results are usually not available. So we try to use the numerical solution as a tool for flow predictions. From previous results presented in the literature, we see it is very difficult to get stable numerical results for viscoelastic fluid dynamics problems. When people set up numerical schemes to simulate those applications like polymer processing, film generation, and injection molding, they face the ‘mysterious’, so called ‘high Weissenberg number’, difficulty [67, 35]. The Weissenberg number basically describes the extent of how elastic the fluid can be, and is usually defined as

$$We = \frac{UL}{\lambda}, \quad (1.16)$$

where  $\lambda$  is the relaxation time and  $U$  is a characteristic fluid velocity and  $L$  is a characteristic length.

Finite element, finite difference, and finite volume methods are proposed to get numerical solutions of viscoelastic fluid flow, but almost all of them encounter the failure of convergence at high Weissenberg number, where the fluid is believed with high elasticity. The methods capturing the hyperbolicity of the system soon were suggested [35], and the well-posedness property of the discretization was taken into consideration too. After decades of exploration, finite element method gains most achievements and is the most popular tool for numerical simulations of polymer processing now. There are streaming-upwind/Petrov-Galerkin (SUPG), elastic viscous stress splitting (EVSS) schemes proposed and quite successfully achieve computational results for higher Weissenberg number flow, but they can not remove the finite Weissenberg barrier.

There are various sources of errors introduced by numerical procedures, and the predominant one is caused by the violation of the incompressibility constraint during the computation. In such cases of violation, spurious waves will be generated by numerical errors and propagate in the system, and finally contaminate the numerical solution. We propose [61] a new systematic treatment for the evolution of extra stress, by which we can explain the reason of convergence breakdown in previous numerical works. Our scheme ensures the incompressibility constraint satisfied at each time step even for highly elastic fluids, and then the ‘high Weissenberg’ difficulty is overcome. We will discuss the analysis and numerical scheme in detail in the last part of the dissertation.

# Chapter 2

## Microscopic scale: the Microrheology in time domain

In the Introduction, we emphasize our first focus on small scale thermal diffusion in mucus. Our goal is to construct a model so we can explore the diffusion property of materials by parameter inversion and so we can also simulate diffusive processes by using those model parameters.

The inspiring proposal of passive microrheology initiated by Mason and Weitz[58] extend the rheological study of materials to micro scale. The experimental measurements of passive microrheology are not on bulk deformation of materials but noisy and small amplitude disturbance of micron/nano meter size thermally fluctuated beads embedded in soft matters. (cf. [58, 28]) The method is ideally suited for characterization of a microscopic viscoelastic modulus governing diffusive transport of Brownian particles and is chosen as our starting point of study here.

Microrheology is now a popular method for applications in molecular and cellular biology for its capacity of dealing with the microscopic length scales and experiment sample with small quantities. The fundamental idea behind passive microrheology is to establish the connection between the strength of thermal fluctuations experienced by a Brownian particle and the storage and loss properties of the surrounding medium. As in viscous fluids, the exploration corresponds to measuring the diffusion coefficient of a small spherical particle with known radius, and thus the fluid viscosity by the Stokes drag law. For viscoelastic fluids as we are dealing with, Mason and Weitz [58] reach the relation (1.11) with passive microrheology technique. The theoretical model

utilized for the Brownian particles are the generalized Langevin equation (GLE), and the generalized Stokes-Einstein relation. Mason and Weitz illustrated the inference of frequency-dependent loss (viscous) and storage (elastic) moduli by frequency binning and ensemble averaging of mean-square displacement of tracer beads. The microscopic shear modulus function, is recovered in the frequency (Laplace transform) domain, presumably providing the same information gained with bulk rheometers (cf. [24]).

Now people believe the bead geometry (compared to the equilibrium length scale of polymeric material) and the phobicity or attraction of polymer chains to beads affect the bead fluctuation too and the direct inference from bead dynamics may actually include the effect of viscoelastic moduli and bead-solution chemical interactions [85, 43, 26]. However, the application that motivates our research is a direct and inverse description of *the diffusion of individual pathogenic particles (e.g., bacteria, environmental particulate, proteins) in biological liquids, cells, and tissues*. We can restrict our interest in the diffusive transport property of a specific pathogen and we want to recover it by the GLE model of Brownian beads with the path data.

The goal of direct simulation of diffusive transport requires the physical properties expressed in time domain instead of in frequency domain. We notice that in frequency-space methods as proposed in the original microrheology framework (the inertial is also neglected there), we are faced with the problem of recovery from Laplace (or unilateral Fourier) transform information of the modulus. Inversion of Laplace transforms is known as a difficult subject with many sources of numerical and analytical inaccuracy. This practice difficulty is not critical for getting values of storage and loss moduli at discrete frequencies as in transformation of microrheology, but it is potentially fatal for numerical Laplace inversion of the entire time-dependent function. This issue of accuracy, first from converting time series path data to frequency space, and then from inverting back to the time domain, is one motivating reason for us to pursue a time-domain inverse characterization of the memory kernel, based directly on the primitive experimental time series data. Another motivation for time-domain methods is the possibility of inversion from much smaller data sets, e.g., single paths which may not be sufficient for frequency binning whereas statistical analysis of individual time series data may prove sufficient. Finally, for very small volume materials there will be constraints on the amount of sample path data that can be collected, which may not be statistically significant for ensemble averaging.

For these reasons above, we have explored here new time-domain methods, which

enable us to direct model and invert diffusive property in time domain. These tools will subsequently be applied to model anomalous diffusion in pulmonary liquids, which is the context in which this work began as part of the Virtual Lung Project at UNC. We will present proof-of-principle illustrations of our time-domain methods, for the generalized Langevin models. We will lay out the theoretical framework and then illustrate the method with example of data numerically generated by GLE model, and the comparison between ‘exact’ and recovered parameters is followed. We also compute mean-squared-displacement statistics directly from our formulation of the GLE, and show agreement with ensemble averaging of path data.

The model here is based on the discrete treatment of (generalized) Langevin equation. Basically we just take the discretization of the stochastic equation (SDE) as autoregressive (AR) process. And the inverse characterization strategy utilized here is the maximum likelihood estimation (MLE) which is developed for time series analysis. The tools will give us estimates of the diffusive transport parameters directly from single or multiple time trajectories of Brownian particles; and standard errors for those estimated parameters; and we could also get goodness of fit criteria. Thus, the methods convey whether the presumptive memory kernels accurately fit the data, or in practice, how many discrete modes are needed to get a best fit. To carry the analysis, we consider an exponential series approximation to the memory kernel, which turns out to be particularly efficient for both inversion and direct simulations. As we notice here, the framework we propose here could be combined with ensemble averaging of the original microrheology method to get better results.

We note here that the results reported in this chapter are mainly from the collaboration with John Fricks, Tim Elston, and Greg Forest, the work is summarized in [26]. In the following text, we will first recall the Langevin equation for Brownian beads in viscous fluids as an introduction to the statistical concepts and physical quantities we are adopting. The emphasis there is to address the treatment of stochastic process and discuss the simple version of fluctuation dissipation theory for later extension. Then we extend our study to beads in viscoelastic fluid and introduce generalized Langevin equation, where the important fluctuation dissipation theorem is presented and utilized. We present the detailed discussion for a single mode case as illustration of the methodology. After present the framework, we then show the deterministic prediction by virtual of the new GLE formulation and demonstrate with examples of simulating viscoelastic material with Zimm/Rouse polymer chain. The inversion scheme of MLE

based on the formulation then is proposed, and tested for numerical generated data. At last, we discuss the case where external deterministic force presents.

## 2.1 Viscous model: Langevin equation

The Langevin equation is the model equation describing the motion of dilute solution of Brownian particles in viscous fluid. The dilute assumption is made to avoid the bead-bead interaction for the particles; and in that circumstance, the source of force upon Brownian particles are only due to the molecules of solvent, which are much smaller than the Brownian beads. The Langevin equation takes the point of view from Newton second law and divides the force into two pieces: resistance force proportional to the bead velocity; and random force. We can see the resistance to the particle motion is an average effect of the instantaneously collisions between small solvent molecules and the Brownian particle, and we just assume the simple Stokes drag law hold for this case; and the remain part of the total force is random in nature due to the uncertainty of the collisions. Given a bead of diameter  $a$ , and mass  $m$ , the Langevin equation for its velocity  $v$  (1d) is formulated as

$$m \frac{dv}{dt} = -\xi v + f(t), \quad (2.1)$$

where  $\xi$  is the friction coefficient given by the Stokes drag law  $\xi = 6\pi a\eta$ ,  $\eta$  is the viscosity of the fluid, and  $f$  represents the random force on the bead, which acts as the propelling source for the Brownian beads. If we denote the position of beads  $x(t)$ , then we should have

$$v(t) = \frac{dx(t)}{dt}, \quad (2.2)$$

and

$$x(t) = x(0) + \int_0^t v(s) ds. \quad (2.3)$$

### 2.1.1 Solution to Langevin equation

The analysis in this subsection could be found in any standard statistical physics text, the purpose of restating it is to prepare us for the model formulation and the introduction of the statistical treatment we provide for the GLE model next.



We can expect there is underlying relationship between the friction force and the random force in Langevin equation of (2.1) because the two forces have the same origin: molecule collisions. To better understand these two related subjects,  $f(t)$  is mathematically treated as a stochastic process in time. We want to impose necessary physical assumptions on the random process and then given the property of  $f$ , we try to further understand the property of  $v(t)$  of the Brownian system. Then we may find out the relationship between the random force and the drag resistance, and make our understanding clear.

As expected, the fluctuating force  $f$  should be averaged to zero when the system is in steady state, since no preference could be assumed then. Also, in viscous solvent, we could assume the characteristic time of solvent collision is much smaller than the beads motion, so the random force is Delta correlated in time. With those assumptions taken, it is natural to use white noise for the random force  $f(t)$ , and then equation (2.1) is the Ornstein-Uhlenbeck process. And from texts, [13, 41, 92], we can see (equipartition law for equilibrium is used)

$$\langle f(0)f(t) \rangle = k_B T \xi \delta(t), \quad (2.4)$$

where  $\delta(t)$  is the Dirac Delta function. This equation defines the connection between the force correlation and the Stokes drag law (friction coefficient), and is the inspiring relation for our further extension to more general problems.

The Ornstein-Uhlenbeck process (2.1) can be written in stochastic integration form (take  $\alpha = \xi/m$ )

$$v(t) = e^{-\alpha t} v(0) + \int_0^t e^{-\alpha(t-s)} f(s) ds, \quad (2.5)$$

which is a quadrature solution to stochastic differential equation (2.1). And the velocity autocorrelation function is

$$\langle v(s)v(s+t) \rangle = k_B T e^{-\alpha t}. \quad (2.6)$$

The mean square displacement (MSD) can also be evaluated:

$$\langle (x(t) - x(0))^2 \rangle = \frac{2k_B T}{\alpha m} \left[ t - \frac{1}{\alpha} (1 - e^{-\alpha t}) \right]. \quad (2.7)$$

By analyzing (2.7), we can see the ballistic and diffusive behavior.

The solution (2.5) describes the single particle dynamics, and we can see from (2.6) and (2.7) that all the average information of (2.5) of the Langevin equation could be derived given the Brownian bead property ( $a$  and  $m$ ) and viscous fluid property ( $\eta$ ).

### 2.1.2 Discrete Langevin equation : AR representation

Whenever the Brownian particle is observed, the experimental results are on discrete time points. To simulate the experimental path data, we want to realize the system with a discrete model of Langevin equation (2.1) with time step  $\Delta$ . The usual way of simulating is to model the velocity of Brownian particles in viscous fluids by discretizing (2.1) using an Euler approximation:

$$v_n = (1 - \alpha\Delta)v_{n-1} + \sigma\sqrt{\Delta}\tilde{\epsilon}_n, \quad (2.8)$$

where  $v_n = v(n\Delta)$ ,  $\sigma = \sqrt{2k_B T\xi/m^2}$ , and  $\tilde{\epsilon}_n$  are standard normal random variables and independent each other at different times. So  $v_n$  is actually represented as a first order autoregressive (AR) process, in which the current velocity  $v_n$  is dependent on previous one and a normal random variable.

We notice the nice properties that the Ornstein-Uhlenbeck process (2.1) has: it is Gaussian, Markovian, and stationary. So we try to take the advantage of those properties and explore the solution (2.5), to avoid discretization error. Similar as (2.8), we present the *exact* discrete version of Langevin equation (2.1):

$$v_n = e^{-\alpha\Delta}v_{n-1} + \epsilon_n, \quad (2.9)$$

where  $\epsilon_n$  is a sequence of independent Gaussian normal random variables with variance

$$s(\Delta) = \sigma^2 \frac{1 - e^{-\alpha\Delta}}{2\alpha}. \quad (2.10)$$

We see (2.8) is the first order approximation of (2.9). (By using Taylor expansion about  $\Delta$  in (2.9), we get (2.8) back.)

Compared to (2.8), the advantages of the discretization (2.9) are obvious. We can

generate particle trajectories accurately at each time step, the probability distribution is exact without numerical approximate error. This way of discretization will be used repeatedly for more complicated model process in following text, and we will construct accurate direct simulation model and inversion based on this discrete representation.

### 2.1.3 Full system of position & velocity

In real bead tracking experiments, observations are usually on positions of Brownian particles and the velocity is calculated by numerically differentiation. To avoid the error introduced by differencing data, as proposed in [26], we will formulate a system equation to include position dynamics in our representation too.

If we couple (2.3) and (2.1) and write them into vector form as

$$\frac{d}{dt}Y(t) = AY + KW(t), \quad (2.11)$$

where

$$Y = \begin{pmatrix} x(t) \\ v(t) \end{pmatrix}, \quad A = \begin{pmatrix} 0 & 1 \\ 0 & -\alpha \end{pmatrix}, \quad K = \begin{pmatrix} 0 & 0 \\ 0 & \sigma \end{pmatrix}, \quad (2.12)$$

and  $W(t)$  is a 2d Gaussian white noise process. The *quadrature solution* to equation (2.11) is [66]

$$Y(t) = e^{At}Y(0) + \int_0^t e^{A(t-s)}KW(s)ds. \quad (2.13)$$

We notice the matrix exponential  $e^A$  and  $e^{At}$  can be formulated as

$$e^A = \begin{pmatrix} 1 & e^{-\alpha} \\ 0 & e^{-\alpha} \end{pmatrix}, \quad e^{A\Delta} = \begin{pmatrix} 1 & \Delta e^{-\alpha\Delta} \\ 0 & e^{-\alpha\Delta} \end{pmatrix}, \quad (2.14)$$

Similarly as in scalar case for velocity Langevin equation, the process (2.11) is Gaussian and uniquely defined by its mean and covariance. Given an initial condition  $Y_0 = Y(0)$  and a time step increment  $\Delta$ , we can determine the exact distribution of  $Y_1 = Y(\Delta)$  and by iteration define a vector AR process, as in (2.9) above. For general iteration, we note that conditioning on  $Y_{n-1}$ , the distribution of  $Y_n$  is Gaussian with mean  $e^{A\Delta}Y_{n-1}$

and covariance matrix [66, 31]

$$S(\Delta) = \int_0^\Delta e^{A(\Delta-s)} K K^T e^{A^T(\Delta-s)} ds. \quad (2.15)$$

From the definition of covariance matrix, it is straightforward to generate exact realizations of the stochastic process at finite time intervals, with the assumption that we can accurately calculate  $S$ . For  $A$ ,  $K$  in (2.12) and the property of  $e^A$  in (2.14), it is trivial calculation on 2 by 2 matrix to get matrix form of  $S$  and we put its components here:

$$\begin{aligned} S_{11} &= \frac{1}{4\alpha^3} \left( -1 - 2\Delta e^{\Delta\alpha} \alpha (1 + \Delta e^{\Delta\alpha} \alpha) + \right. \\ &\quad \left. e^{2\Delta\alpha} (1 + 2\Delta(-1 + e^{\Delta\alpha}) \alpha (1 + \Delta(-1 + e^{\Delta\alpha}) \alpha)) \right), \\ S_{12} &= \frac{e^{\Delta\alpha} (-1 - 2\Delta e^{\Delta\alpha} \alpha + e^{2\Delta\alpha} (1 + 2\Delta(-1 + e^{\Delta\alpha}) \alpha))}{4\alpha^2}, \\ S_{21} &= S_{12}, \\ S_{22} &= \frac{e^{2\Delta\alpha} (-1 + e^{2\Delta\alpha})}{2\alpha} \end{aligned} \quad (2.16)$$

For a particle starting from state  $Y_{n-1}$ , we generate a Gaussian vector  $\epsilon_n$  with covariance matrix  $S$  of (2.15) and add it to the dependent part of  $e^{A\Delta} Y_{n-1}$  to get  $Y_n$ , and then the simple iteration formulated as:

$$Y_n = e^{A\Delta} Y_{n-1} + \epsilon_n. \quad (2.17)$$

Thus, we have an autoregressive (AR) representation for the vector process  $Y_0, \dots, Y_N$  analogous to the scalar process (2.9).

## 2.2 Brownian particle in viscoelastic media

As for the problem of Brownian particle thermally driven in viscoelastic fluids, we have to extend the standard Langevin equation model to deal with the complexity arising from the delayed retardation. When we discuss the situation of typical viscoelastic materials in which the embedded Brownian particle's surrounding molecules are comparable to Brownian bead themselves in size, the standard Langevin Equation

(2.1) will fail to capture effect of the velocity retardation on the drag force. In order to incorporate the effect that drag force is accumulatively dependent on the history of Brownian bead's velocity, the time dependent drag coefficient function is introduced and we then have the generalized form of Langevin Equation, the generalized Langevin equation (GLE) to work with.

### 2.2.1 Generalized Langevin equation

Compared with (2.1), in which the drag law is assumed proportional to velocity, the phenomenological description of generalized Langevin equation introduces the convolution of velocity history as followed

$$m \frac{dv(t)}{dt} = - \int_0^t \psi(t - \tau) v(\tau) d\tau + R(t), \quad (2.18)$$

where  $\psi(t)$  now is a function in time and is usually called memory function or kernel, and the random force  $R$  here is not white noise any more but colored random process.

In [29], one special example of generalized Langevin equation is discussed thoroughly: the kernel function is simple exponential decay:

$$m \frac{dv(t)}{dt} = - \int_0^t G_0 e^{-(t-s)/\lambda} v(\tau) d\tau + R(t). \quad (2.19)$$

By using Fourier transformation, Hansen et. [29] give explicit velocity autocorrelation function as

$$\langle v(t)v(s) \rangle = \frac{c^2 \lambda^3}{m^2 \beta (1 - \beta)} e^{\frac{1-\beta}{2\lambda}|t-t'|} - \frac{c^2 \lambda^3}{m^2 \beta (1 + \beta)} e^{\frac{1+\beta}{2\lambda}|t-t'|}, \quad (2.20)$$

and then the mean square displacement formula is followed

$$\begin{aligned} \langle [x(t) - x(t')]^2 \rangle &= \frac{4k_B T}{m} \left\{ \frac{2\lambda}{1 - \beta^2} |t - t'| - \frac{2\lambda^2(3 + \beta)}{(1 - \beta^2)^2} \right. \\ &\quad \left. + \frac{\lambda^2}{\beta(1 - \beta^2)^2} \left( e^{-\frac{1-\beta}{2\lambda}|t-t'|} (1 + \beta)^3 - e^{-\frac{1+\beta}{2\lambda}|t-t'|} (1 - \beta)^3 \right) \right\}, \end{aligned} \quad (2.21)$$

where  $\beta = \sqrt{1 - 4c\lambda^2}$  and  $c = 6\pi a G_0/m$ . For sufficiently short times, the MSD (2.21) exhibits ballistic behavior,  $\langle [x(t) - x(0)]^2 \rangle \approx k_B T t^2/m$ , and for sufficiently long times, diffusive scaling emerges,  $\langle [x(t) - x(0)]^2 \rangle \approx 2k_B T t/m\lambda c$ . For intermediate times, a power law fit of the MSD yields a range of exponents depending on the window in which one chooses to fit.

We note the parameter  $\beta$  can be purely imaginary, as pointed out in [29], which is clear from the formula (2.21). Oscillations are predicted in the velocity correlation and MSD whenever physical parameters obey  $4c\lambda^2 > 1$ . The direct numerical evidence of oscillation is the appearance of a pair of complex eigenvalues for matrix  $A$ .

This GLE model phenomenon predicts high frequency (short time) oscillations in Brownian bead path data, *even after ensemble averaging of path time series*, which translates to a source of high frequency error of MSD in experiment measurement because of the phase mismatch between these inherent oscillations and experimental sampling time. The relatively large error bars of MSD at high frequencies thus appear to be inherent for GLE processes with exponential series kernels, and cannot be eliminated by simply running the experiments for longer times.

## 2.2.2 Fluctuation-Dissipation theory

Even the drag law in complex fluids depends velocity retardation, and is more complicated than the case of viscous fluids, we still expect the direct connection between the memory kernel  $\phi(t)$  and the random force  $R(t)$  in the GLE (2.18). The result, which is given by the fluctuation dissipation theorem, is intensively discussed in [41, 92].

The fluctuation dissipation theorem can be formulated as following [41, 40, 92]

$$\langle R(t)R(s) \rangle = k_B T \psi(t - s), \quad t > s, \quad (2.22)$$

where  $k_B$  is the Boltzmann constant and  $T$  is the temperature. We note the relation (2.4) can be viewed as the special case of this relation with the Delta function as the memory kernel, and we also notice if  $\psi(t) = \delta(t)$ , the generalized Langevin will reduce to standard Langevin (2.1).

This fluctuation dissipation theorem gives the direct link between random force  $R$  and kernel function  $\psi(t)$  at thermal equilibrium state. This theory then essentially

connects the dynamics of embedded beads with material property, and if one of  $R$  and  $\psi$  is given, we can figure out the other by using fluctuation dissipation theory. For our purpose of direct and inverse characterization, if we can construct proper random force  $R$  and kernel function  $\phi$  that satisfy GLE and FD, with undetermined fitting parameters, we then can *solve* the GLE dynamics system, and we will have the ability to manipulate the inversion and then predict the direct simulation.

To simplify the statistical calculation, we will normalize the generalized Langevin equation (2.18) by using FD theory (2.22) to

$$\frac{dv(t)}{dt} = - \int_0^t \xi(t-\tau)v(\tau)d\tau + \sqrt{\frac{k_B T}{m}}f(t), \quad (2.23)$$

where correlation of force  $f$  follows

$$\langle f(t)f(s) \rangle = \xi(t-s), \quad t > s. \quad (2.24)$$

Throughout the remainder of this chapter when we refer to the memory kernel, we will mean  $\xi(\cdot)$ , which is  $\psi$  in (2.18) scaled by  $1/m$ .

### 2.2.3 Reformulation of the GLE

As we can expect, the generalized Langevin equation (2.18) with general type kernel function  $\psi$  is hard to solve. Back in 60s of last Century, Zwanzig (cf. [90, 91, 63, 62]) developed the ‘projection operator’ technique to solve GLE formally for general type memory kernel function. But for our purpose, it is awkward to work in that formal framework. Our intention of solving the model problem is, as proposed by Forest and Elston [26]: if we can construct a series random processes to model the random force, and if we can impose the correlation function of those processes as the kernel  $\xi$  in (2.23) by using fluctuation dissipation theorem, we then can also ‘solve’ the generalized Langevin equation, and the order of accuracy is determined by the approximation of the random force, or kernel function.

In this section, we show that for a certain class of memory kernels, specifically a sum of exponentials, the generalized Langevin equation can be expressed as a set of coupled linear SDEs *of the same form as* (2.11), in which the velocity and position

are the first two components. Therefore, all Langevin equation properties and techniques carry over immediately to the GLE. In particular, we can: 1) apply maximum likelihood methods for parameter estimation by taking advantages of random system representation; 2) exactly simulate the stochastic process instead of low-order numerical integration; and 3) write down explicit formulas for statistical quantities of interest, such as autocorrelation functions for position and velocity.

So we suppose the memory kernel in GLE of (2.23) is a single exponential function with physical parameter,

$$\xi(t) = ce^{-\frac{t}{\lambda}}, \quad c = \frac{6\pi aG}{m}, \quad (2.25)$$

which corresponds in “bulk” linear viscoelasticity to a single-mode Maxwell fluid with modulus  $G$  and relaxation time  $\lambda$ . (Note:  $\lambda G = \eta_0$  is the zero strain rate viscosity of a simple Maxwell fluid.) In (2.25),  $a$  is the particle radius. The noise  $F(t)$ , (2.23-2.24), for an exponential kernel can be expressed as an Ornstein-Uhlenbeck process,

$$\frac{dF(t)}{dt} = -\frac{1}{\lambda}F(t) + \sqrt{\frac{2c}{\lambda}}f(t), \quad (2.26)$$

where  $f(t)$  is white noise. Note that the Langevin equation is obtained in the limit  $\lambda \rightarrow 0$ , that is, (2.26) becomes (with  $\xi_0 = 6\pi a\eta_0$ )

$$F(t) = \sqrt{\frac{2\xi_0}{m}}f(t). \quad (2.27)$$

Analogous to the scalar Ornstein-Uhlenbeck process (2.1) and by taking advantage of (2.25), the system (2.23-2.26) may be solved explicitly. Again, to apply the statistical tools we adopted in previous section, we try to setup vector version of AR process for the GLE, analogous to the Langevin case (2.9). To see this, we define the auxiliary variable  $Z(t)$

$$Z(t) = \int_0^t e^{-\frac{t-\tau}{\lambda}} V(\tau) d\tau, \quad (2.28)$$

which yields

$$\frac{dZ(t)}{dt} = -\frac{1}{\lambda}Z(t) + V(t). \quad (2.29)$$



Now, the full system can be written in matrix form as

$$\frac{d}{dt}Y(t) = AY(t) + KW(t) \quad (2.30a)$$

with

$$A = \begin{pmatrix} 0 & 1 & 0 & 0 \\ 0 & 0 & -c & \sqrt{\frac{k_B T}{m}} \\ 0 & 1 & -\frac{1}{\lambda} & 0 \\ 0 & 0 & 0 & -\frac{1}{\lambda} \end{pmatrix}, \quad K = \begin{pmatrix} 0 & 0 & 0 & 0 \\ 0 & 0 & 0 & 0 \\ 0 & 0 & 0 & 0 \\ 0 & 0 & 0 & \sqrt{\frac{2c}{\lambda}} \end{pmatrix} \quad (2.30b)$$

$$Y(t) = (X(t), V(t), Z(t), F(t))^T, \quad (2.30c)$$

and  $W(t)$  is a vector of independent white noise processes.

This system (2.30a)-(2.30c) is *identical* in form to (2.11), and therefore another vector Langevin equation, whose quadrature solution is given by (2.13) and (2.15) with these  $Y$ ,  $A$  and  $K$ . Following the Langevin example above, we can now generate the corresponding viscoelastic AR process for a Brownian particle with this specified memory kernel, starting from  $Y_0 = Y(0)$ .

More generally, suppose the memory kernel  $\xi^N(t)$  is given by an  $N$ -mode exponential series:

$$\xi^N(t) = c_1 e^{-\frac{t}{\lambda_1}} + c_2 e^{-\frac{t}{\lambda_2}} + \dots + c_N e^{-\frac{t}{\lambda_N}}, \quad (2.31)$$

where  $c_i = 6\pi a G_i / m$ . Similarly, the total noise  $F^N(t)$  can be written as

$$F^N(t) = F_1(t) + F_2(t) + \dots + F_N(t), \quad (2.32)$$

where each  $F_i(t)$  is an independent Ornstein-Uhlenbeck process characterized by the  $i^{th}$  relaxation time  $\lambda_i$ . That is,

$$\frac{dF_i(t)}{dt} = -\frac{1}{\lambda_i} F_i(t) + \sqrt{\frac{2c_i}{\lambda_i}} f_i(t), \quad (2.33)$$

where  $f_i(t), i = 1, \dots, N$  are independent white noise processes.

Therefore,  $F^N(t)$  is a mean-zero Gaussian process with covariance consistent with

the fluctuation-dissipation theorem,

$$\langle F^N(t)F^N(s) \rangle = c_1 e^{-\frac{t-s}{\lambda_1}} + c_2 e^{-\frac{t-s}{\lambda_2}} + \dots + c_N e^{-\frac{t-s}{\lambda_N}}. \quad (2.34)$$

This formulation of the GLE yields once again a vector Langevin process of the form (36), with the following definitions for  $Y$ ,  $A$  and  $K$ :

$$Y = \begin{pmatrix} X(t) \\ V(t) \\ Z_1(t) \\ \dots \\ Z_N(t) \\ F_1(t) \\ \dots \\ F_N(t) \end{pmatrix}, A = \begin{pmatrix} 0 & 0 & 1 & \dots & 0 & 0 & \dots & 0 \\ 0 & 0 & -c_1 & \dots & -c_N & \sqrt{\frac{k_B T}{m}} & \dots & \sqrt{\frac{k_B T}{m}} \\ 0 & 1 & -1/\lambda_1 & \dots & 0 & 0 & \dots & 0 \\ \dots & \dots & \dots & \dots & \dots & \dots & \dots & \dots \\ 0 & 1 & 0 & \dots & -1/\lambda_N & 0 & \dots & 0 \\ 0 & 0 & 0 & \dots & 0 & -1/\lambda_1 & \dots & 0 \\ \dots & \dots & \dots & \dots & \dots & \dots & \dots & \dots \\ 0 & 0 & 0 & \dots & 0 & 0 & \dots & -1/\lambda_N \end{pmatrix}, \quad (2.35)$$

$$K = \begin{pmatrix} 0 & 0 & \dots & 0 & 0 & 0 & \dots & 0 \\ 0 & 0 & \dots & 0 & 0 & 0 & \dots & 0 \\ 0 & 0 & \dots & 0 & 0 & 0 & \dots & 0 \\ \dots & \dots & \dots & \dots & \dots & \dots & \dots & \dots \\ 0 & 0 & \dots & 0 & 0 & 0 & \dots & 0 \\ 0 & 0 & \dots & 0 & 0 & \sqrt{\frac{2c_1}{\lambda_1}} & \dots & 0 \\ \dots & \dots & \dots & \dots & \dots & \dots & \dots & \dots \\ 0 & 0 & \dots & 0 & 0 & 0 & \dots & \sqrt{\frac{2c_N}{\lambda_N}} \end{pmatrix} \quad (2.36)$$

Again, an *exact solution of this system* is given in the form (2.13) and (2.15) with these matrix formulas. Thus, all properties of the Langevin equation have been extended to the GLE for the class of N-mode exponential series kernels. Likewise, the machinery from Section 2 applies for generating direct realizations of GLE processes and performing statistical analysis of time series for partial observations (of position).

These formulas are valuable to the extent we can numerically calculate the matrix

exponential  $e^A$ . The special form of  $A$ , equation (2.35), lends itself to an explicit and straightforward determination of the eigenvalues and eigenvectors, for any mode number  $N$ . Furthermore, this calculation only has to be done once, both to generate the direct process (or statistics of the process), and to perform parameter inversion for each  $N$ . The procedure of computing the spectrum and then the covariance matrix are given in the Appendix of [26].

#### 2.2.4 Analysis on the covariance matrix $S$

We discuss how the covariance matrix  $S$  in equation (2.15), with  $(2n+2) \times (2n+2)$  coefficient matrices  $A$  and  $K$  defined as in equation (2.35), can be numerically calculated accurately and efficiently. The only difficulty is in finding all  $2n+2$  eigenvalues of  $A$ ; the remaining steps are straightforward. First we factor out the simple zero eigenvalue with the position equation coupled. For simplicity, we introduce parameters

$$c_i = \frac{6\pi a G_i}{m} = \frac{6\pi a \eta_i}{m \lambda_i}, \quad \sigma_i = \sqrt{\frac{k_B T}{m}}, \quad \kappa_i = \sqrt{\frac{2c_i}{\lambda_i}}. \quad (2.37)$$

Clearly,  $n$  eigenvalues,  $\{-1/\lambda_i\}_{i=1}^n$ , are obvious. The remaining  $n+1$  are determined by the roots of the polynomial equation

$$P(x) = x \prod_{i=1}^n \left(x + \frac{1}{\lambda_i}\right) + \sum_{i=1}^n c_i \prod_{j \neq i}^n \left(x + \frac{1}{\lambda_j}\right) = 0. \quad (2.38)$$

If we rewrite the above polynomial (2.38) by dividing it with  $\prod_{i=1}^n (x + 1/\lambda_i)$ , we have a new function

$$Q(x) = x + \sum_{i=1}^n \frac{c_i}{x + 1/\lambda_i}, \quad (2.39)$$

which has the same roots as  $P(x)$ . Recall  $0 < \lambda_1 \cdots < \lambda_n$ . Clearly  $Q(x)$  changes sign, and therefore has one zero, in each interval  $(-1/\lambda_i, -1/\lambda_{i+1})$ . These are easily found by iteration. This yields  $n-1$  eigenvalues, denoted  $\{x_i\}_{i=1}^{n-1}$ , and only 2 remain.

The polynomial  $P(x)$  of Eq. (2.38) has the form (2.38) as

$$P(x) = (x^2 + bx + c) \prod_{i=1}^{n-1} (x - x_i) = 0, \quad (2.40)$$

where  $c$  and  $b$  are given explicitly from  $\{-1/\lambda_i\}_{i=1}^n, \{x_i\}_{i=1}^{n-1}$ :

$$\begin{aligned} c &= (-1)^{n-1} \frac{P(0)}{\prod_{i=1}^{n-1} x_i} = \frac{\sum_{i=1}^n c_i \prod_{j \neq i}^n \frac{1}{\lambda_j}}{\prod_{i=1}^{n-1} |x_i|} > 0, \\ b &= -c - 1 + \frac{\prod_{i=1}^n (1 + \frac{1}{\lambda_i})(1 + \sum_{i=1}^n c_i \frac{1}{1 + \frac{1}{\lambda_i}})}{\prod_{i=1}^n (1 - x_i)} > 0. \end{aligned} \quad (2.41)$$

This completes the calculation of all  $2n + 2$  eigenvalues. The sign of  $b^2 - 4c$  determines the 2 remaining zeros, and all eigenvalues have non-negative real part. If the two roots are complex conjugates,  $A$  is only diagonalizable in the complex space.

Similarly, for the matrix  $As$  in equation (2.15), where  $s$  is a scalar, all the eigenvalues scale explicitly with  $s$  and the eigenvectors remain the same.

For  $n = 1, 2, 3$ , there are analytical formulas for the roots of the polynomial. In the single mode case,  $n = 1$ , the eigenvalues are

$$\omega_1 = -\frac{1}{\lambda}, \quad \omega_2 = -\frac{1}{2}(1/\lambda + \sqrt{\frac{1}{\lambda^2} - 4\alpha}), \quad \omega_3 = -\frac{1}{2}(1/\lambda - \sqrt{\frac{1}{\lambda^2} - 4\alpha}), \quad (2.42)$$

with easily calculated eigenvectors. The covariance matrix  $S$  (2.15) can thus be calculated in closed form.

For general  $n$ , from equation (2.40) and (2.41), a very fast and efficient numerical scheme is found for the eigenvalues and eigenvectors. Given this detailed spectral information for  $A$ , we can pre-compute the covariance matrix  $S$ , as follows:

First we assume the matrix  $A$  has full span of eigenvectors  $R$  (its inverse is  $R^{-1}$ ),

$$A = R\Lambda R^{-1}, \quad A^2 = AA = R\Lambda R^{-1}R\Lambda R^{-1} = R\Lambda^2 R^{-1} \quad (2.43)$$

where  $\Lambda$  is a diagonal matrix whose diagonal components are the eigenvalues of  $A$ .

By definition,

$$e^A = \sum_{n=0}^{\infty} \frac{A^n}{n!} = \sum_{n=0}^{\infty} \frac{R\Lambda^n R^{-1}}{n!} = R\left(\sum_{n=0}^{\infty} \frac{\Lambda^n}{n!}\right)R^{-1} = Re^{\Lambda}R^{-1}, \quad (2.44)$$

where we see  $e^{\Lambda}$  is diagonal and the covariance matrix  $S$  can be written as

$$\begin{aligned} S &= R\left(\int_0^{\Delta} e^{\Lambda u} R^{-1} K K^T (R^{-1})^T e^{\Lambda^T u s} du\right) R^T \\ &= R\left(\int_0^{\Delta} e^{\Lambda s} M e^{\Lambda s} ds\right) R^T, \end{aligned} \quad (2.45)$$

where we define  $M = (R^{-1}K)(R^{-1}K)^T$ .

Next, we consider the integral representation for the covariance matrix. We take advantage of the above properties of the matrix  $A$ , as follows. Denoting by  $e^{\omega_i s}$  the  $i$ th diagonal component of the diagonal matrix  $e^{\Lambda s}$ , where  $w_i$  is the  $i$ th eigenvalue of matrix  $A$ , and  $M_{ij}$  the  $i$ th row and  $j$ th column component of matrix  $M$ , we see immediately

$$\begin{aligned} e^{\Lambda s} M e^{\Lambda s} &= (M_{ij} e^{w_i s})_{(2n+1) \times (2n+1)} e^{\Lambda s} \\ &= (M_{ij} e^{(w_i + w_j) s})_{(2n+1) \times (2n+1)}, \end{aligned} \quad (2.46)$$

where  $M_{ij} e^{(w_i + w_j) s}$  is the  $i$ th row, and  $j$ th column component of the integrand matrix. So, in general

$$\begin{aligned} S &= R\left(M_{ij} \int_0^{\Delta} e^{(\omega_i + \omega_j) s} ds\right) R^T \\ &= R\left(M_{ij} \frac{e^{(\omega_i + \omega_j) \Delta} - 1}{\omega_i + \omega_j}\right) R^T, \end{aligned} \quad (2.47)$$

and after all the eigenvalues  $\omega_i$  of  $A$  are determined, the integral form of  $S$  can be pre-calculated according to the above result and the integration of the matrix function can be avoided.

If we include the bead position  $X(t)$  in the system of equations, the eigenvalues of  $A'$  include  $\{-1/\lambda_i\}_{i=1}^n$ , and the remaining  $2n + 2$  are determined by the roots of the

polynomial equation

$$P_d(x) = x \left( x \prod_{i=1}^n \left( x + \frac{1}{\lambda_i} \right) + \sum_{i=1}^n c_i \prod_{j \neq i}^n \left( x + \frac{1}{\lambda_j} \right) \right) = 0. \quad (2.48)$$

Compared to the system in the previous subsection, the only difference is an extra zero eigenvalue and all other analytical results carry over.

## 2.3 Direct simulation: theory and examples

From the result of (2.47), we can avoid the numerical integration of the covariance matrix, and this is a great advantage, derived from the vector AR representation formulation of GLE, for the direct simulation of Brownian bead trajectory in viscoelastic fluids. We can see the simulation has lots of applications in pathogen transport in biological soft materials.

Analogous to (2.17), vector form of GLE (2.30a) can be formulated to a discrete process in the same way: starting from  $Y_0 = Y(0)$ , the iteration is defined as

$$Y_n = e^{A\Delta} Y_{n-1} + \epsilon_n, \quad (2.49)$$

where matrix  $A$  is defined in (2.30b), and most importantly, the covariance matrix of the vector normal random noise  $\epsilon_n$  is determined (2.47). If we have fixed constant time steps in a simulation, which is the usual case, covariance  $S$  can be calculated only once for the simulation, so the only cost of numerical calculation in the simulation is matrix vector multiplication. Also, fast and accurate parallel subroutines for matrix multiplications can be applied to increase the performance of the simulation.

### 2.3.1 Numerical calculation of correlation function

We can calculate the velocity correlation function (and the position correlation function if we include the position  $X(t)$  into our original vector SDE) since the velocity is the first component of the vector  $Y(t)$ .

So

$$\begin{aligned}
\langle Y(t)Y(t') \rangle &= \left\langle \left( e^{At}Y(0) + \int_0^t e^{A(t-s_1)}KW(s_1)ds_1 \right) \right. \\
&\quad \left. \left( e^{At'}Y(0) + \int_0^{t'} e^{A(t'-s_2)}KW(s_2)ds_2 \right)^T \right\rangle \\
&= \langle e^{At}Y(0)(e^{At'}Y(0))^T \rangle + \\
&\quad \left\langle \int_0^t ds_1 \int_0^{t'} ds_2 e^{A(t-s_1)}KW(s_1)(e^{A(t'-s_2)}KW(s_2))^T \right\rangle
\end{aligned} \tag{2.50}$$

By applying the property of correlation of white noise, we could get

$$\begin{aligned}
\langle Y(t)Y(t') \rangle &= e^{At} \langle Y_0 Y_0^T \rangle e^{A^T t'} \\
&\quad + \int_0^t \int_0^{t'} ds_1 ds_2 e^{A(t-s_1)} K (\delta(s_1 - s_2) I) K^T e^{A^T(t'-s_2)}
\end{aligned} \tag{2.51}$$

It is clear that our analysis of the eigensystem of matrix  $e^A$  would help here, and we just recall

$$e^A = R e^\Lambda R^{-1}, \tag{2.52}$$

where  $R$  is the eigenvector matrix and  $R^{-1}$  is its inverse, and  $\Lambda$  is a diagonal matrix whose diagonal components correspond to the eigenvalues of matrix  $A$ . Since the first term at the right side of above (2.51) will be usually zero, we would rewrite (2.51) as

$$\langle Y(t)Y(t') \rangle = R \left( \int_0^t \int_0^{t'} \delta(s_1 - s_2) e^{\Lambda(t-s_1)} M e^{-\Lambda(t'-s_2)} ds_1 ds_2 \right) R^T \tag{2.53}$$

where  $M = (R^{-1}K)(R^{-1}K)^T$ .

Again, by analyzing the components of the above matrix integral, we notice that

$$(e^{\Lambda(t-s_1)} M e^{-\Lambda(t'-s_2)})_{i,j} = M_{ij} e^{\lambda_i(t-s_1) + \lambda_j(t'-s_2)}, \tag{2.54}$$

where  $\lambda_i$  is the  $i$ th eigenvalue of matrix  $A$ , and  $M_{ij}$  represents the  $i$ th row and  $j$ th column component of the matrix  $M$  defined above.

Indeed, in the formula of calculating the autocovariance matrix (2.53), we can re-

arrange the integration a little to

$$\langle Y(t)Y(t') \rangle = R \left( \int_0^\infty \int_0^\infty \delta(s_1 - t - s_2 + t') e^{\Lambda s_1} M e^{\Lambda s_2} ds_1 ds_2 \right) R^T, \quad (2.55)$$

and the  $(i, j)$  component of the integral of matrix is

$$\begin{aligned} & \int_0^\infty \int_0^\infty ds_1 ds_2 \delta(s_1 - t - s_2 + t') M_{ij} e^{\lambda_i s_1 + \lambda_j s_2} \\ &= \begin{cases} M_{ij} \frac{-e^{\lambda_i(t-t')}}{\lambda_i + \lambda_j} & \text{For } t' > t > 0 \\ M_{ij} \frac{-e^{\lambda_j(t'-t)}}{\lambda_i + \lambda_j} & \text{For } 0 < t' < t \end{cases} \end{aligned} \quad (2.56)$$

Now we can get the correlation of velocity (and position) directly from (2.56), if we know the relaxation spectrum, since the integrals are easily computed and the eigenvector matrix are determined after we get the relaxation spectrum is prescribed. This result means we can evaluate the MSD and velocity correlation function given the memory kernel spectrum, and it then provides us an easy way to study the effect of memory kernel modes on the scaling law of MSD. Based on the result of (2.56), we can see the velocity (and position) correlation function is the coupling effect of the different relaxation mode. And the coupling is surely nonlinear and we may discuss it with spectral analysis of the matrix and get more information.

### 2.3.2 Example of Rouse and Zimm chain models

We consider special cases of polymeric material of Rouse and Zimm model here, as the examples to illustrate the use of the GLE model to model dynamics of beads in viscoelastic fluids. A classical model describing polymer dynamics due to Rouse (cf. [69, 8, 45, 70]) yields a special class of  $N$ -mode moduli for which GLE diffusive transport properties are explicitly solvable. A 4-mode Rouse kernel is implemented now to further illustrate the AR and maximum likelihood direct and inverse strategy, and to benchmark our direct simulations against exact MSD scaling laws. In the Rouse model, polymer chains are treated as spherical masses connected by Hookean springs of equilibrium length  $b$ . Beads in Rouse chain only interact with each other through the connecting springs and are not affected by the solvent effect of the motion of other



beads. The Zimm model (cf. [89, 8, 70]) incorporates hydrodynamic interactions among the beads, which leads to different exponential relaxation spectra; a Zimm kernel is presented next. Yet more complex molecular models incorporate overlap and entanglements of the polymer chains, or even chemical interactions between the Brownian particle and its local environment. Our focus of the examples here is to model the fluctuations, not to dissect the various sources; thus, our goal is to find the best GLE kernel to fit measured fluctuations, or to simulate fluctuations for a prescribed kernel.

In the Rouse model, each bead has friction coefficient  $\xi_b$  and the shear modulus and relaxation time of the  $i$ th mode are given by [46]:

$$G_i = G_0 = \nu k_B T, \quad \lambda_i = \frac{\xi_b}{16k_B T \beta_b^2 \sin^2(i\pi/2(N+1))}, \quad (2.57)$$

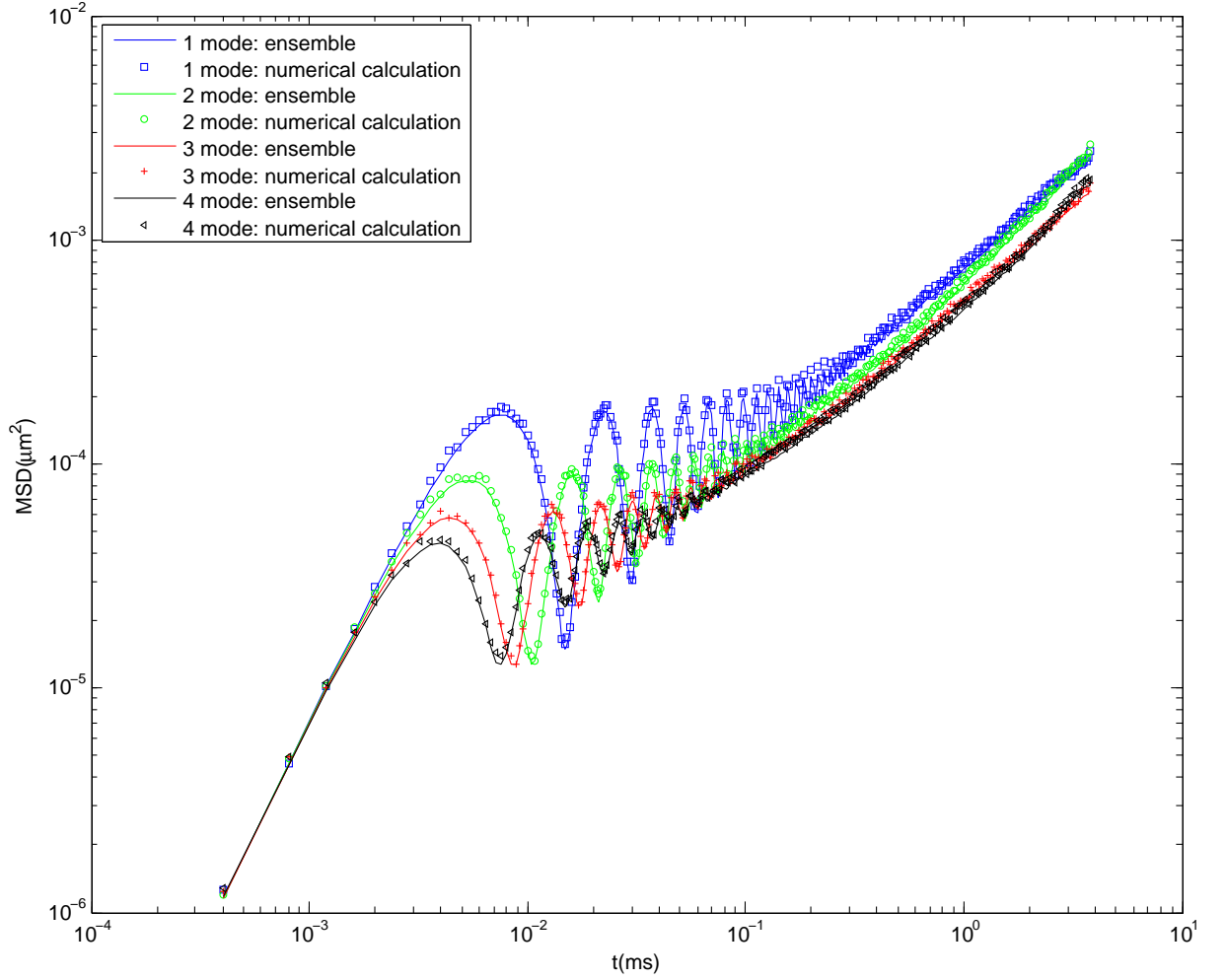
where  $\nu$  is the number density of the polymer chain and  $\beta_b = 3/(Nb^2)$ . In the example to follow, we choose  $\nu = 2\%$ , which is roughly on the same magnitude as mucin concentration in healthy human mucus. We now specify all parameter values in the 4-mode Rouse-GLE model. The passive bead is  $1\mu m$  in diameter of mass  $m = 1.05 \times 10^{-9} mg$ . The single modulus parameter (each exponential has the same modulus or pre-factor) is given by  $G_0 = G = 1.035 \times 10^{-5} mg/ms^2 \mu m$ , so that our parameters are  $c = c_i = 6\pi a G_0 / m = 4.44 \times 10^{-4} (ms)^{-2}$ . The Rouse relaxation times are (2.57):  $\lambda_1 = .02415$ ,  $\lambda_2 = .04294$ ,  $\lambda_3 = 0.09661$ , and  $\lambda_4 = .3864$  in units of  $ms$ .

In Figure 2.3.2, we show the ensemble of sample paths simulated from the GLE mode with the above parameters, and we also show the corresponding numerical evaluation of MSD based on (2.56) formulation. This figure verifies that GLE model phenomenon predicts high frequency (short time) oscillations in experimental path data. And we can see with number of modes increases, the amplitude of oscillation decreases and the starting time of oscillation is always less than the smallest relaxation time.

Unlike (2.57) for the Rouse model, there is no exact formulation of relaxation spectrum for Zimm model, but we have approximate formulation of corresponding spectrum [70, 20]. The approximation of relaxation spectrum for Zimm model is formulated as [70]

$$\lambda_i \approx \lambda_0 \left( \frac{N}{i} \right)^{3\nu} \quad (2.58)$$

Figure 2.1: MSD comparison in different number of modes. The MSD results if we superimpose different number of modes with fixed  $c = 1.74 \cdot 10^5 (ms)^{-2}$ . The 1 mode curve is the MSD of the longest relaxation time  $\lambda_1 = 0.3864ms$ , as reported in section 2.3.2, of the example of Rouse chain. To increase the number of modes, we add one more mode whose relaxation time is smaller than the current smallest. The effect is clear that the oscillation is less in magnitude and the MSD expectation is also less.



where we denote the shortest relaxation time

$$\lambda_0 = \frac{\xi_b b^2}{k_B T}, \quad (2.59)$$

and  $\nu \approx 0.59$  is the scaling exponent.

We now illustrate the methods are not “mode limited”, by running direct simulations for beads of the same size and mass as in Figure 2.3, but with a GLE diffusive transport modulus specified by a 22-mode Zimm kernel. The model posits 1100 monomers along each polymer chain, which we divide into 22 sub-units, which gives 22 modes and an explicit relaxation spectrum. Figure 2.2 shows the MSD statistics, again generated both by ensemble averaging of paths and by the autocorrelation formula (2.56). The simulations predict a MSD power law scaling exponent of 0.62 when fitted between the shortest and longest relaxation spectra, which reasonably approximates the  $\frac{2}{3}$  theoretical value of the Zimm model.

## 2.4 Inversion based on the GLE formulation

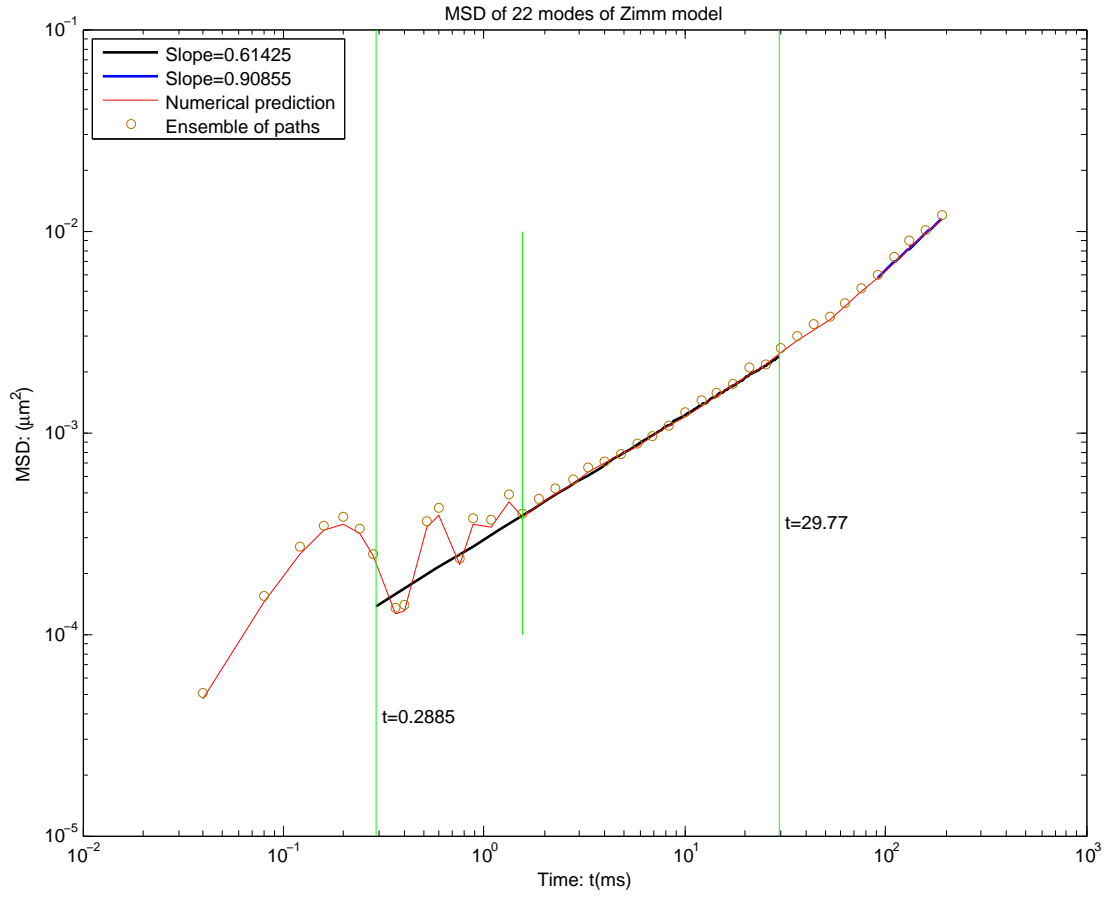
The formulation of the vector AR process for the discrete GLE allows us to apply standard statistical to analyze the time dynamics of bead position and velocity. We will present the inversion method used in [26] for diffusive modulus based on this formulation of the GLE.

### 2.4.1 The MLE method on the velocity of Langevin equation

We now turn to maximum likelihood methods which give a general framework to obtain point estimators and standard errors for the model parameters,  $\alpha$  and  $\sigma$ , given a time series  $v_0, v_1, \dots, v_N$ . The presentation is organized and illustrated for the Langevin model (2.9) by Fricks in our paper [26], to show how the general procedure of MLE for the inversion of diffusive transport property. This subsection of presentation only shows the way of MLE optimization. The real inversion on experimental measurements, which are positions instead of velocity, will be discussed in next subsection.

The likelihood function is computed from the joint probability density for an observed velocity time series. Noting that the time series is Markov, that the conditional

Figure 2.2: MSD of the GLE with a 22-mode Zimm kernel. The smallest relaxation time is  $0.2885ms$ , and then the Zimm relaxation spectrum is calculated by (2.58), which gives the longest  $29.77ms$ ; the two vertical lines mark the time span between them, over which a power law of  $0.6142$  fairly approximates the theoretical Zimm model value of  $\frac{2}{3}$ . (comparison of ensemble average and numerical prediction is also presented)



distribution of  $v_n$  given  $v_{n-1}$  is normal with mean  $e^{-\alpha\Delta}v_{n-1}$  and variance (2.10), and assuming that the initial velocity  $v_0$  is known, the likelihood function is given by

$$\begin{aligned} L(\alpha, \sigma) &= g(v_1, \dots, v_N | v_0, \alpha, \sigma) \\ &= \prod_{n=1}^N h(v_n | v_{n-1}, v_0, \alpha, \sigma) \\ &= (2\pi s(\alpha, \sigma))^{-n/2} \exp \left( - \sum_{n=1}^N \left( \frac{v_n - e^{-\alpha\Delta}v_{n-1}}{2S(\alpha, \sigma)} \right)^2 \right), \end{aligned}$$

where  $g(\cdot | v_0, \alpha, \sigma)$  is the joint density of  $v_1, \dots, v_N$  and  $h(\cdot | \cdot, v_0, \alpha, \sigma)$  is the transition density for the process. Given a sequence of velocity measurements, the likelihood function is numerically maximized to obtain estimates,  $\hat{\alpha}$  and  $\hat{\sigma}$ , for  $\alpha$  and  $\sigma$ . Hereafter in the paper, parameter estimates are denoted by  $\hat{\cdot}$ .

One of the benefits of maximum likelihood estimation is that under fairly general conditions to be given in the Appendix of [26], asymptotic probability distributions for these estimators may be obtained. Note that while  $\alpha$  is not random,  $\hat{\alpha}$  depends on the random time series  $v_0, \dots, v_N$  and is a random variable; given a new time series one obtains a new realization of the random variable. In the present context, we know *a priori* that the estimator  $\hat{\alpha}$  is asymptotically (for long time series, i.e. large number of observations  $N$ ) normal with mean equal to the true parameter  $\alpha$  and variance of  $\hat{\alpha}$  equal to  $(-\partial_\alpha^2 \log L(\alpha, \sigma))^{-1}$ . We obtain an estimate for the variance of  $\hat{\alpha}$  by numerically calculating the derivative of the log likelihood function at the maximized value.

We emphasize that model parameters may be estimated from a single time series of the process; this will be illustrated in the proof-of-principle illustrations below. If that single particle path is sufficiently long, then the Mason-Weitz approach and our approach should be consistent (a final example addresses this point). Ensemble averaging in the time and frequency domains can be performed as well, following the Mason-Weitz protocol, if there are sufficient sample paths or if a single path is sufficiently long. The methods introduced here can be applied even if the data set is not large; this corresponds either to a large  $\Delta$  or a low number of iterations in the discrete process. We will return to this issue below in a discussion of over- and under- resolution of the underlying stochastic process, and in comparisons of quality of fits versus number of observations.

### 2.4.2 Kalman filter for systems including positions

After we have cast the Langevin/GLE model in the form of a vector AR process, which include both velocity and position components, we are in position to calculate the appropriate likelihood function for estimating parameters, given a time series of particle positions  $x_0, x_1, \dots, x_N$ . In this section, the Kalman protocol for the likelihood function is outlined by Fricks in our paper [26] and the content here is just a complete restate.

We outline key steps in the derivation of the likelihood function, The derivation relies on ideas from the Kalman filter, which was developed to estimate the current state of a dynamical system from noisy time series data of partial observations of the process. (This use of the Kalman filter as a method to calculate the likelihood function has become standard and further discussion can be found in [31] and [11].) Recall discrete observations generated from the Langevin equation satisfy (2.17), where the noise has a covariance structure given by (2.15). Experimentally, only the position of the particle is observed, and no other components of the vector  $Y$ . That is, at the  $n$ th time interval the observable is

$$x_n = CY_n, \quad C = \begin{pmatrix} 1 & 0 \end{pmatrix} \quad (2.60)$$

Assuming that the model parameters,  $\Theta$ , are known, a Kalman filter is generally used to recursively estimate the current state,  $Y_n$ , given the observations  $x_1, \dots, x_n$ . Using this and the AR structure of the process, we may also give a predictive density for  $Y_{n+1}$  given  $x_1, \dots, x_n$ . From this we may obtain the density of  $x_{n+1}$  given  $x_1, \dots, x_n$  which we denote by  $h(x_{n+1}|x_m, m < n+1, \Theta, x_0)$ . We may then decompose the joint density for the time series into a product of these conditional densities and obtain

$$g(x_1, x_2, \dots, x_N | \Theta, x_0) = \prod_{n=2}^N h(x_n | x_m, m < n, \Theta, x_0). \quad (2.61)$$

Because the process is Gaussian, the above equation can be rewritten as

$$\begin{aligned} -\log L(\Theta) &= -\log g(x_1, x_2, \dots, x_N | \Theta, x_0) \\ &= \frac{1}{2} \sum_{n=1}^N \left( \log 2\pi + \log Q_{n-1} + \frac{(x_n - \hat{x}_{n|n-1})^2}{Q_{n-1}} \right), \end{aligned} \quad (2.62)$$

where the conditional mean and variance of  $x_n$  given  $x_1, \dots, x_{n-1}$  are

$$\hat{x}_{n|n-1} = Ce^{A\Delta} \hat{Y}_{n-1} \quad (2.63)$$

and

$$Q_{n-1} = CR_{n-1}C^t, \quad (2.64)$$

respectively, and the matrix  $R_n$  is defined in the Appendix of [26]. Therefore, once we have  $x_0, x_1, \dots, x_N$  we may numerically maximize this likelihood function with respect to the parameters to obtain an estimate for  $\Theta$ . An important feature of this Kalman derivation of the likelihood function is that it may be calculated recursively; this dramatically reduces the time necessary to calculate the likelihood function since we do not have to calculate the full covariance matrix of the entire time series.

Of course, this method requires numerical calculation of the matrices  $S$  and  $\exp(A\Delta)$ , but this calculation only has to be done *once* for each trial parameter set in the maximization process. This numerical calculation is, of course, trivial for  $2 \times 2$  systems, but presents a potential limitation for the GLE, which we will soon formulate in this precise vector AR setting, and where the matrix size scales with the number of exponential modes. Below, we overcome this potential limitation due to the special form of the matrices that arise for GLEs with exponential kernels.

As with the univariate case, there are asymptotic results for the distribution of our maximum likelihood estimators  $\hat{\Theta}$ . Under certain reasonable conditions given in the Appendix of [26],  $\hat{\Theta}$  is asymptotically normal with mean  $\Theta$  and covariance given by  $\text{cov}(\hat{\Theta}) = (-\nabla \log L(\Theta))^{-1}$  which may be approximated by numerical evaluation of the quantity  $(-\nabla \log L(\hat{\Theta}))^{-1}$ . Thus, to build a  $1 - \alpha$  confidence interval for  $\theta_m$ , we start with

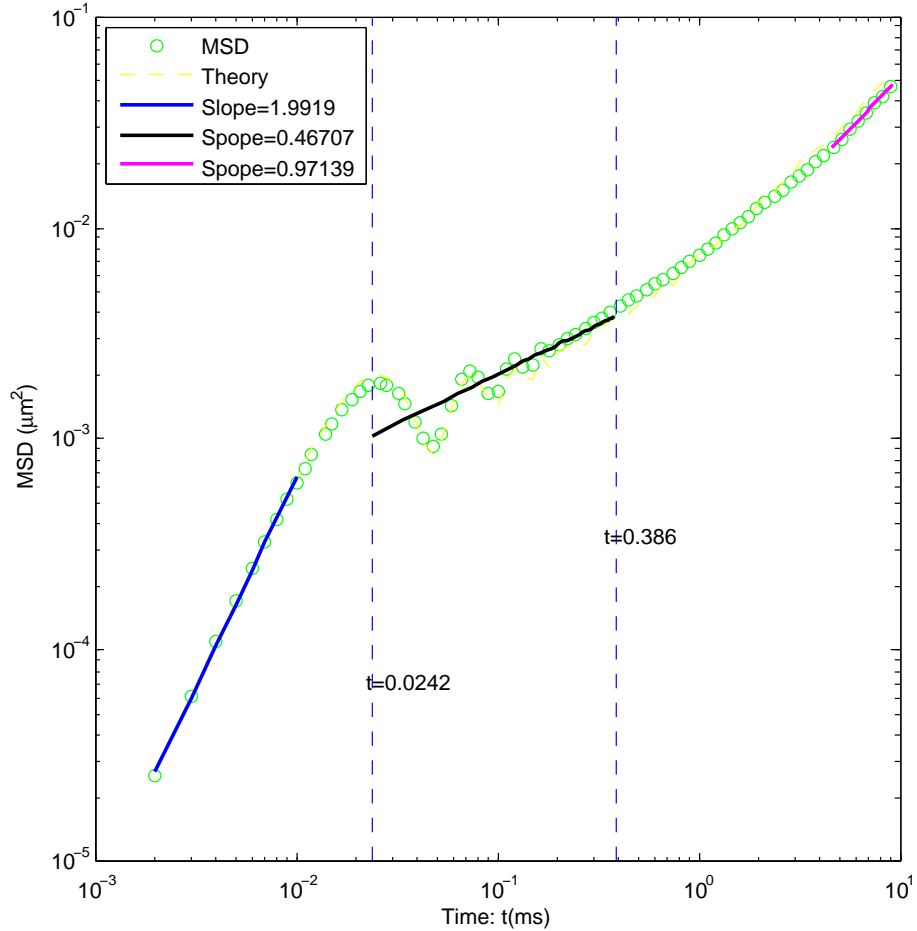
$$P(-z_{\alpha/2} \leq \frac{\hat{\Theta}_m - \theta_m}{\text{cov}(\hat{\Theta})_{m,m}} \leq z_{\alpha/2}) \approx 1 - \alpha, \quad (2.65)$$

where  $z_{\alpha/2}$  is the value that satisfies  $P(Z > z_{\alpha/2}) = \alpha/2$  and  $Z$  is a standard Gaussian random variable. We use the notation  $A_{m,n}$  to denote the element in the  $m$ th row and  $n$ th column of the matrix  $A$ . With some algebra, we have

$$\theta_m \in (\hat{\Theta}_m - z_{\alpha/2} \text{cov}(\hat{\Theta})_{m,m}, \hat{\Theta}_m + z_{\alpha/2} \text{cov}(\hat{\Theta})_{m,m}), \quad (2.66)$$

which is the desired confidence interval for  $\theta_m$ .

Figure 2.3: MSD of GLE sample paths for a 4-mode Rouse diffusive transport modulus. 200 paths are generated for a  $1 \mu\text{m}$  diameter bead at  $293\text{K}$ . The Rouse relaxation times are  $\lambda_1 = .02415$ ,  $\lambda_2 = .04294$ ,  $\lambda_3 = 0.09661$ , and  $\lambda_4 = .3864$  in units of  $ms$ , with a shear modulus  $G_0 = 1.035 \times 10^{-5} mg/ms^2 \mu\text{m}$ . To benchmark analytical scaling laws, a linear fit between the two vertical blue dashed lines (from the shortest to longest relaxation times) confirms the MSD power law of  $.5$  for the Rouse model. The short-term ballistic and long-term diffusive scaling are also confirmed.





## 2.5 Comparison between MLE and M-W framework

The inverse characterization framework proposed in this dissertation focuses on single path information in the time domain, which is a complement to the transform space formulation of Mason and Weitz [58, 57, 56]. We now compare the two approaches on data generated above for the 4-mode Rouse kernel. To make a fair comparison, we simulate an experiment which gathers many bead paths.

As defined in [24], the complex modulus has the form:

$$G^*(\omega) = i\omega \int_0^\infty G(s)e^{-i\omega s}ds = G' + iG'', \quad (2.67)$$

where  $G(t)$  is the shear relaxation modulus of bulk linear viscoelasticity. If we associate the shear modulus with the 4-mode Rouse kernel, the corresponding storage and loss moduli are:

$$G'(\omega) = \sum_{i=1}^4 \frac{G_0\omega^2\lambda_i^2}{1 + \omega^2\lambda_i^2}, \quad G''(\omega) = \sum_{i=1}^4 \frac{G_0\omega\lambda_i}{1 + \omega^2\lambda_i^2}, \quad (2.68)$$

where  $G_0$  and  $\lambda_i$  are defined earlier, equation (2.57).

The experimental data are generated from 4-mode Rouse model as given in 2.32, and Figure 2.3, consisting of 200 paths of  $1\mu m$  size beads shows the MSD of the example.

The results of inversion in previous sections which introduce the maximum likelihood framework, give us relaxation spectrum with different number of modes. In Figure 2.4, we show the complex modulus recovered by those modes (finished by Fricks as in [26]). We note the 4-mode maximum likelihood fit is very accurate for the 4 mode Rouse model that we input as the example.

The MSD information in Figure 2.3 is then transformed and analyzed in the frequency domain with the Mason-Weitz protocol. For the transformation of the MSD data, the approximate algebraic expansion [56] is used to obtain the complex shear modulus. To compare the inversion in the time domain with the maximum likelihood methods, a nonlinear regression method proposed in [64] is used to convert the loss and storage modulus in the frequency domain to a relaxation spectrum of generalized Maxwell type in the time domain.

The complex modulus is calculated from Eq. (2.68) with varying number of modes. The complex modulus obtained with 4 modes fit is very accurate compared to the

original input, and the 3 modes fitting result is very close to the result of 4 modes fit so we did not include it in the figure. The 1 and 2 modes fit results, relaxation time and shear modulus, are statistically optimal (residuals are minimal) but the relaxation modulus recovered are not close to the real values.

Figure 2.5 shows the comparison of the storage and loss moduli recovered by the Maximum Likelihood (ML) method (the best 4-mode fit as determined from the data) and the Mason-Weitz (M-W) transformation method. Compared to M-W method, the ML method more accurately recover  $G'$  and  $G''$ . We note that the inherent oscillations at relatively short times in the MSD turn out to make it difficult for the M-W transformation protocol to capture the high frequency information; we anticipate the error caused by this part of the MSD statistics is the largest source of error in the M-W modulus inversion.

Figure 2.6 shows the relaxation spectrum recovered by the two methods. We notice the transformation tends to overestimate the relaxation time and the modulus. The reason of the overestimate may due to the fact that the transformation intend utilize MSD information that is beyond the longest relaxation time, and the results suggest oscillatory high frequency error inherent in the transformation may accumulate errors.

Figure 2.4: Storage and loss moduli results of different number of exponential modes recovered by the MLE inverse procedure.

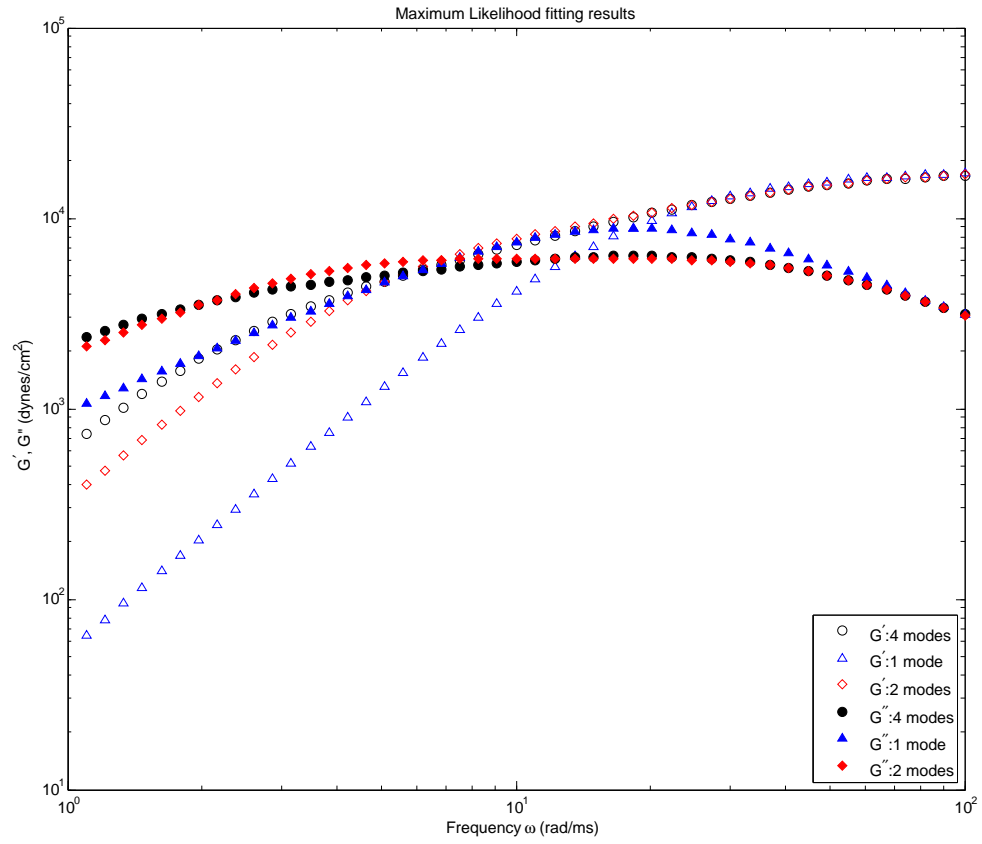


Figure 2.5: The storage and loss moduli recovered from the same numerical GLE data with a 4-mode Rouse kernel, by the Maximum Likelihood (ML) method and the Mason-Weitz method. The ML results correspond to a best 4-mode exponential kernel fit.

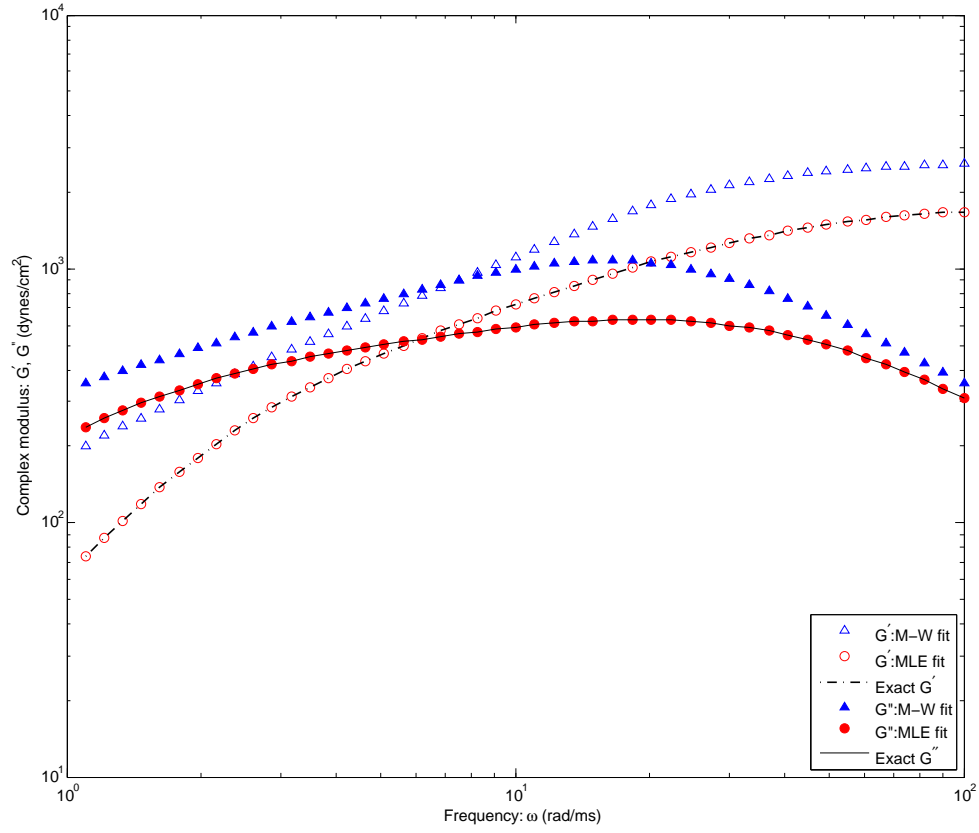
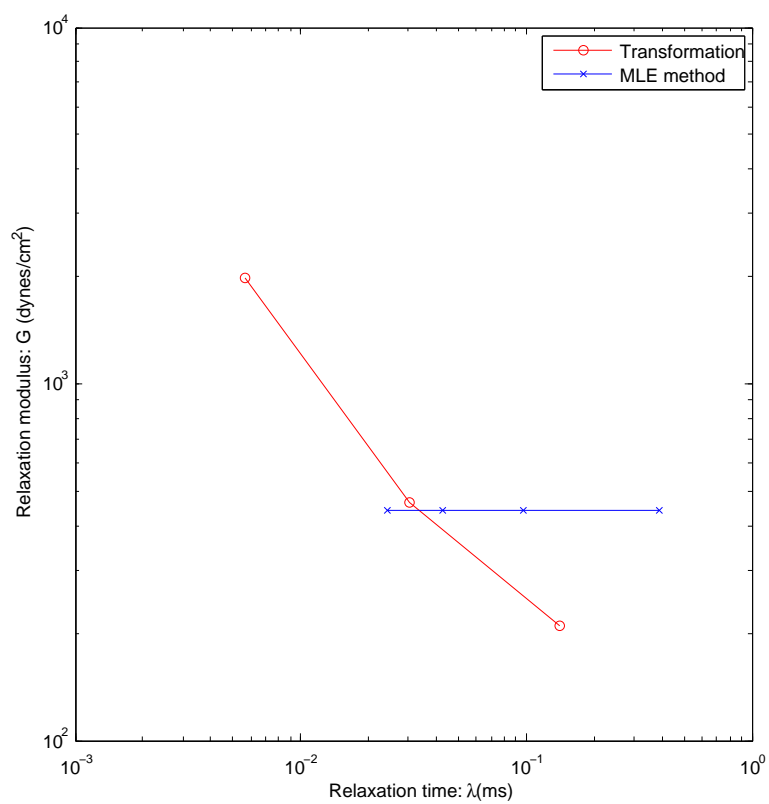


Figure 2.6: Comparison of shear relaxation modulus and relaxation time recovered by M-W method and MLE method. And we note the recovery of MLE is almost exact.



# Chapter 3

## Shearwave modeling and computation

After the discussion of microscopic diffusive transport phenomena, we move on to bulk properties of viscoelastic fluid. As we mentioned in the introduction chapter, the transport of the mucus layer involves bulk rheological properties of mucus and we present suitable experimental tools and analytical analysis.

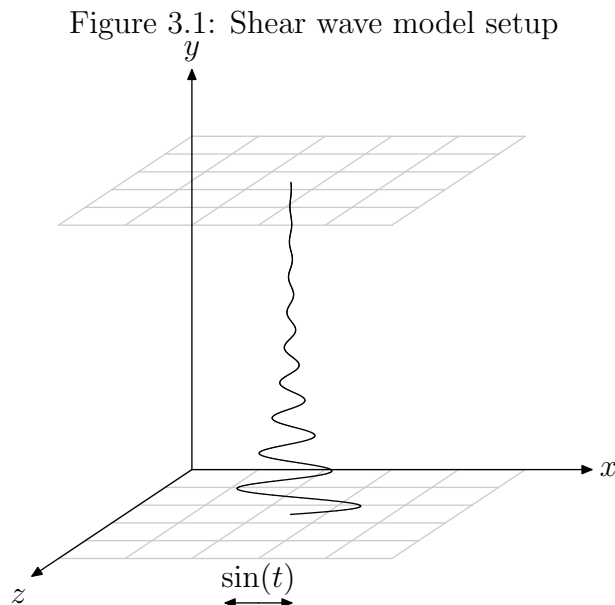
By noticing the driving forces of mucus transport: the coordinated cilia beating and tidal breathing cycles, we first revisit the classical shear wave model of Ferry and collaborators [23, 25, 1]. In Ferry's model, oscillatory motion of plate generates unidirectional shear waves propagating in viscoelastic media, and the damped wave profile was recorded by birefringence techniques. The measurements of Ferry's experiment are on the wave length and the attenuation length of the shear waves. Based on those measurements, the characteristic storage and loss modulus information can be deduced by the Ferry's model equation, in which we assume the oscillation of wave is damped out before they reach the opposite plate. This experimental setup is appealing to us since the pulmonary mucus layer experiences similar oscillatory transport. We expect the inversion based on this shear wave setup gives us proper characteristics of the mucus layer so we can apply them in direct numerical simulations and make predictions more accurate.

We note that the problem we are faced is in small volume biological fluid, and the reflection of deformation/stress propagation from top boundary makes it necessary to consider the finite depth effect in the model and then Ferry's original model setup

has to be extended to the case of finite domain. In the following, we will introduce analytical solution for the finite channel depth model, which is an extension of the linear shear wave model. We also point out here the fact that the normal stress components are completely neglected in the linear shear wave model. Because the normal stress is usually believed occurring in pulmonary liquid transport, we also extend the linear shear wave model by using Giesekus constitutive law, in which the nonlinearity effect of shear thinning can be considered. The results presented in this chapter are inspired by the experiment of D. Hill and R. Superfine, and are collaboration work with Sorin M. Mitran, M. Gregory Forest, Brandon Lindley and David B. Hill[60].

### 3.1 Shear wave models

We consider a layer of incompressible fluid of height  $\tilde{H}$ , moved by an oscillating lower flat plate, and whose upper surface remains flat and parallel to the bottom plate. The superscript  $\sim$  will be used to denote quantities in physical units. The bottom plate



is set to harmonic motion as illustrated in Figure 3.1.

A reference viscosity  $\tilde{\eta}_0$  is set for the fluid of interest of density  $\tilde{\rho}$ , namely the zero strain-rate viscosity of the fluid. The reference length  $\tilde{A} = \tilde{V}_0/\tilde{\omega}$  is the maximum displacement of the driven bottom plate; the reference time  $\tilde{\omega}^{-1}$  is set by the plate frequency; and the reference stress  $\tilde{\eta}_0\tilde{\omega}$  is the viscous plate shear stress. With

those characteristic scales, the non-dimensional velocity of the bottom plate is given by  $v_x(0, t) = \sin(t)$ , where  $v_x(y, t)$  denotes the velocity component of the fluid in the direction of plate motion at height  $y$ . As in Ferry's analysis, it is a property of the model equations that with this scaling, we can focus on the 2-parameter space of values of storage and loss moduli, and make general statements about errors in recovering the moduli that depend only on the pair of values, independent of the imposed frequency. Also a viscoelastic material relaxation time  $\tilde{\lambda}$  is identified. And the following dimensionless parameters arise in our model equations:

- Reynolds number  $Re = \tilde{\rho}\tilde{\omega}\tilde{A}^2/\tilde{\eta}_0$
- Deborah number  $\lambda = \tilde{\lambda}\tilde{\omega}$
- Bulk shear strain  $\gamma = \tilde{A}/\tilde{H}$

When we consider the motion of the fluid bounded by a lower flat plate and an upper parallel flat boundary, which may be either stationary or free to move (with some unknown attenuation and phase lag with respect to the driven lower plate), we can, by symmetry, restrict all flow and stress variables as functions only of  $t$  and the height  $y$  between the two flat surfaces. In particular, the fluid pressure  $p$ , and velocity components are

$$p = p(y, t), v_x = v_x(y, t), v_y = 0, v_z = 0. \quad (3.1)$$

And for this dimension reduction, the continuity condition is satisfied automatically. Also from  $v_x(y, t)$ , we can deduce particle displacement  $X(y, t)$  at height  $y$  between the two plates:

$$X(y, t) = \int_0^t v_x(y, s)ds + X(y, 0), \quad (3.2)$$

for given initial condition  $X(y, 0)$ .

And we know the momentum balance equation (without external force) of differential form gives (in dimensionless form)

$$\frac{\partial \mathbf{v}}{\partial t} + (\mathbf{v} \cdot \nabla) \mathbf{v} = \frac{1}{Re} \nabla \cdot \boldsymbol{\pi}, \quad (3.3)$$

in which  $\boldsymbol{\pi}$  is viewed as the stress tensor of the fluid. And the total stress  $\boldsymbol{\pi}$  is usually



written as

$$\boldsymbol{\pi} = -p\mathbf{I} + \boldsymbol{\tau} \quad (3.4)$$

where  $p$  represents the isotropic part of the total fluid stress, and together with a constitutive law describing the extra stress,  $\boldsymbol{\tau}$ , which likewise is assumed to depend only on  $t$  and  $y$ ,

$$\boldsymbol{\tau} = \boldsymbol{\tau}(y, t), \quad \text{with } \tau_{xz} = \tau_{yz} = 0. \quad (3.5)$$

To close the system for  $(p, v_x, \boldsymbol{\tau})(y, t)$ , we need the constitutive equations for the extra stress  $\boldsymbol{\tau}$ . We will discuss a hierarchy of laws from standard texts [24, 7, 46] in the following sections.

### 3.1.1 Stokes second problem

For viscous fluids, the Navier-Stokes constitutive law is

$$\boldsymbol{\tau} = 2\mathbf{D}, \quad (3.6)$$

where  $\mathbf{D} \equiv \frac{1}{2}(\nabla \mathbf{v} + \nabla \mathbf{v}^T)$  is the rate of strain tensor (the viscosity coefficient does not appear due to the scaling we choose in previous subsection).

From (3.1), it immediately follows that

$$\begin{cases} \tau_{xy} = \eta_0 \frac{\partial v_x}{\partial y}, \\ \tau_{xx} = \tau_{yy} = \tau_{xz} = \tau_{yz} = \tau_{zz} \equiv 0 \end{cases} \quad (3.7)$$

The momentum equation (3.3) reduces to

$$\begin{cases} \frac{\partial v_x}{\partial t} = \frac{1}{Re} \frac{\partial^2 v_x}{\partial y^2} \\ \frac{\partial p}{\partial y} = 0. \end{cases} \quad (3.8)$$

### 3.1.2 Shear wave model in linear viscoelastic fluids

The constitutive law of linear viscoelasticity (the Lodge model) is

$$\boldsymbol{\tau} = 2 \int_{-\infty}^t G(t-t') \mathbf{D}(y, t') dt', \quad (3.9)$$

where  $G(t)$  is the shear relaxation modulus function. In physical units we should have  $\tilde{G} = \tilde{\eta}_0 \tilde{\omega} G$ .

Again, by virtue of (3.1),  $\mathbf{D}$  has only  $xy$  ( $yx$ ) nonzero components, and therefore (3.9) reduces to

$$\begin{cases} \tau_{xy} = \int_{-\infty}^t G(t-t') \frac{\partial v_x}{\partial y}(y, t') dt', \\ \tau_{xx} = \tau_{yy} = \tau_{xz} = \tau_{yz} = \tau_{zz} = 0. \end{cases} \quad (3.10)$$

While the momentum equation (3.3) reduces to

$$\frac{\partial v_x}{\partial t} = \frac{1}{Re} \frac{\partial \tau_{xy}}{\partial y}, \quad (3.11a)$$

$$\frac{\partial p}{\partial y} = 0. \quad (3.11b)$$

From (3.10) and (3.11a), we can derive a equation for  $v_x$  as:

$$\frac{\partial v_x}{\partial t} = \frac{1}{Re} \int_{-\infty}^t G(t-s) \frac{\partial^2 v_x}{\partial y^2}(y, s) ds, \quad (3.12)$$

and then shear stress is obtained from (3.10).

We note here for special shear modulus  $G(t)$ , like a single mode Maxwell model,  $G(t) = (\eta_p/\lambda) e^{-t/\lambda}$  (nondimensional form), the equation (3.12) simplified to a damped wave equation (cf [7, 24]),

$$\frac{\partial^2 v_x}{\partial t^2} - \frac{\eta_p}{\lambda Re} \frac{\partial^2 v_x}{\partial y^2} + \frac{1}{\lambda} \frac{\partial v_x}{\partial t} = 0. \quad (3.13)$$

Furthermore, it is clear that the shear stress  $\tau_{xy}$  also satisfies the identical damped wave

equation (3.13).

### 3.1.3 Upper Convected Maxwell and Giesekus models

The standard nonlinear regimes model is treated in classical texts [7, 46]. Either one consider the K-BKZ class of integral constitutive laws, generalizing (3.10), or one applies differential laws, the choice made here. The general approach involves approximation of the shear modulus  $G(t)$  by a truncated exponential series. This is equivalent to decomposition of the extra stress into a finite sum,

$$\boldsymbol{\tau} = \sum_{i=1}^k \boldsymbol{\tau}_i, \quad (3.14)$$

where each  $\boldsymbol{\tau}_i$  obeys a Maxwell-type evolution equation, with nonlinearity appearing in the upper convected derivative and other nonlinear terms for capturing specific nonlinearity effect. We will include the Giesekus model which is a nonlinear extension from Maxwell model and includes shear thinning effect. For the remainder of this chapter, we restrict to a single Maxwell-type mode; the extension to any finite  $k$  is straightforward and the numerical cost increases proportional to the number of modes.

The Maxwell-type evolution equation for the extra stress is

$$\boldsymbol{\tau} + \lambda \overset{\nabla}{\boldsymbol{\tau}} + a \boldsymbol{\tau} \cdot \boldsymbol{\tau} = 2\eta_p \mathbf{D}, \quad (3.15)$$

where  $\eta_p = \tilde{\eta}_p/\tilde{\eta}_0$  is the polymer viscosity in physical unit  $\tilde{\eta}_p$  scaled with the reference viscosity  $\tilde{\eta}_0$ , and  $\overset{\nabla}{\boldsymbol{\tau}}$  is the upper convected derivative of the extra stress,

$$\overset{\nabla}{\boldsymbol{\tau}} = \frac{\partial \boldsymbol{\tau}}{\partial t} + (\mathbf{v} \cdot \nabla) \boldsymbol{\tau} - (\nabla \mathbf{v})^T \cdot \boldsymbol{\tau} - \boldsymbol{\tau} \cdot (\nabla \mathbf{v}). \quad (3.16)$$

We note here [60], the polymeric stress  $\boldsymbol{\tau}$  is produced by  $\mathbf{D}$  and transported by  $\mathbf{v}$ , and is nonlinearly excited by the Giesekus nonlinear term  $a \boldsymbol{\tau} \boldsymbol{\tau}$ . The “mobility parameter”  $a$  can vary:  $a = 0$  is the upper convected Maxwell (UCM) model;  $a = 0.5$  is the Leonov model; in general,  $0 \leq a \leq 1$ , and the mobility parameter is to be fitted from data with  $\lambda$ .

From (3.1), even though  $\mathbf{D}$  has only  $xy$ ,  $yx$  nonzero terms, there are new nonlinear terms from  $\overset{\nabla}{\boldsymbol{\tau}}$  and  $\boldsymbol{\tau} \cdot \boldsymbol{\tau}$  to balance the normal stresses  $\tau_{xx}, \tau_{yy}$ , so that they cannot be ignored. The single mode constitutive law (3.15) then reduces to

$$\begin{cases} \frac{\partial \tau_{xx}}{\partial t} - 2 \frac{\partial v_x}{\partial y} \tau_{xy} + \tau_{xx} = -\frac{a}{\lambda} (\tau_{xx}^2 + \tau_{xy}^2) \\ \frac{\partial \tau_{xy}}{\partial t} - (\tau_{yy} + \frac{\eta_p}{\lambda}) \frac{\partial v_x}{\partial y} + \tau_{xy} = -\frac{a}{\lambda} \tau_{xy} (\tau_{xx} + \tau_{yy}) \\ \frac{\partial \tau_{yy}}{\partial t} + \tau_{yy} = -\frac{a}{\lambda} (\tau_{xy}^2 + \tau_{yy}^2) \\ \tau_{yz} = \tau_{xz} = 0 \end{cases} \quad (3.17)$$

The momentum equation once again is reduced to (3.11a-3.11b) for velocity and pressure.

$$\frac{\partial v_x}{\partial t} = \frac{1}{Re} \frac{\partial \tau_{xy}}{\partial y}, \quad (3.18a)$$

$$\frac{\partial p}{\partial t} = \frac{\partial \tau_{yy}}{\partial y}. \quad (3.18b)$$

As pointed out in [60], we can see from (3.17), the nonlinearity in this system is from the upper convected derivative,  $\overset{\nabla}{\boldsymbol{\tau}}$ , and the shear thinning term  $a\boldsymbol{\tau}^2$ . As in the Newtonian fluid case, there is no convective nonlinearity in the momentum equation itself. An important indicator of nonlinearity is the shear-induced generation of a non-zero first normal stress difference,  $N_1 = \tau_{xx} - \tau_{yy}$ . The presence of a normal stress gradient along the  $y$ -direction then generates a pressure gradient, absent in the linear model. Indeed, if we neglect all nonlinear terms from (3.17) the two normal stress components  $\tau_{xx}, \tau_{yy}$ , obey identical ordinary differential equations

$$\frac{\partial \tau_{xx}}{\partial t} + \frac{1}{\lambda} \tau_{xx} = 0, \quad \frac{\partial \tau_{yy}}{\partial t} + \frac{1}{\lambda} \tau_{yy} = 0. \quad (3.19)$$

So the linear viscoelasticity model can not capture the normal stress in the shear wave flow. And we also see any initial normal stress relaxes exponentially fast and does not propagate nor couple to the shear stress or wave.

The coupled system (3.17) and (3.11a - 3.11b) can be written in the form,

$$\frac{\partial q}{\partial t} + A(q) \frac{\partial q}{\partial y} = \psi(q), \quad (3.20)$$

with

$$q = \begin{bmatrix} v_x \\ \tau_{xx} \\ \tau_{xy} \\ \tau_{yy} \end{bmatrix}, \quad A(q) = - \begin{bmatrix} 0 & 0 & \frac{1}{\rho} & 0 \\ 2\tau_{xy} & 0 & 0 & 0 \\ \eta_0/\lambda + \tau_{yy} & 0 & 0 & 0 \\ 0 & 0 & 0 & 0 \end{bmatrix}, \quad \psi = \frac{-1}{\lambda} \begin{bmatrix} 0 \\ \tau_{xx} + a \frac{\lambda}{\eta_0} (\tau_{xx}^2 + \tau_{xy}^2) \\ \tau_{xy} (1 + a \frac{\lambda}{\eta_0} (\tau_{xx} + \tau_{yy})) \\ \tau_{yy} + a \frac{\lambda}{\eta_0} (\tau_{xy}^2 + \tau_{yy}^2) \end{bmatrix},$$

together with the pressure equation in (3.11b) and  $\tau_{xz} = \tau_{yz} = 0$ .

## 3.2 Analytical results

It is always good to have the model equations solved analytically, so we can apply parameter inversion and direct prediction on the model. For the model equations we presented above, there are analytical results for the case of viscous and linear viscoelastic model for semi-infinite and finite depth problem, and we will discuss them in this section. The solutions can be obtained via Fourier methods by ignoring the transients. We note the transient problem can be solved by Laplace methods. The known solutions to viscous case and linear viscoelastic in semi-infinite domain cases are reviewed here to complete the presentation and for comparison to the extensions we made on linear viscoelastic model with finite depth domain that appear absent in the literature. The discussion of nonlinear model of UCM and Giesekus will be presented in next section for their own characteristics.

### 3.2.1 Solution to the viscous problem

The long time solution for viscous model is widely available (e.g. [71]) and recalled for completeness as well as comparison with generalizations.

**Semi-infinite domain solution.** Upon positing a solution of the form  $v_x(y, t) = \mathcal{I}m\{\hat{v}_x(y)e^{it}\}$  (note the time is in unit of  $\tilde{\omega}^{-1}$ , so the physical frequency is  $\tilde{\omega}/2\pi$ ), the

solution is given by

$$v_x(y, t) = \mathcal{I}m\{e^{-\delta_0 y} e^{it}\} = e^{-\alpha_0 y} \sin(t - \beta_0 y), \quad (3.21)$$

which obeys the far-field boundary condition  $\lim_{y \rightarrow \infty} v(y, t) = 0$ . We introduce here  $\delta_0 = \alpha_0 + i\beta_0 = (1 + i)\sqrt{Re/2}$ . The Reynolds number,  $Re = \tilde{\rho}\tilde{\omega}\tilde{A}^2/\tilde{\eta}_0$ , determines both the penetration ( $1/\alpha_0$ ) and oscillation length scales ( $2\pi/\beta_0$ ), through  $\alpha_0 = \beta_0 = \sqrt{Re/2}$ . The velocity field produces a particle displacement

$$X(y, t) = X(y, 0) + e^{-\alpha y} [\cos(\beta t) - \cos(t - \beta y)]. \quad (3.22)$$

The viscous stress is given by  $\tau_{xy} = \partial v_x / \partial y$ ,

$$\tau_{xy} = \mathcal{I}m\{-\delta_0 e^{-\delta_0 y} e^{it}\} = \sin(t - \beta_0 y + 5\pi/4) e^{-\alpha_0 y} \sqrt{Re}, \quad (3.23)$$

which shows a constant phase difference between the shear stress and the velocity.

**Finite-depth channel with stationary top plate.** The no-slip boundary condition at the top of the channel needs  $v_x(y = H, t) = 0$ . The solution is simply

$$v_x(y, t) = \mathcal{I}m\left\{e^{it} \frac{\sinh[\delta_0(H - y)]}{\sinh[\delta_0 H]}\right\}. \quad (3.24)$$

### 3.2.2 Solution to linear viscoelastic problems

We summarize solutions to (3.11a-3.11b) for boundary conditions representative of experimental configurations. In all the following cases the bottom plate velocity is assumed to be  $v_x(0, t) = \sin(t)$ .

**Semi-infinite domain solution**[24, 7]. If the fluid height is much larger than the wavelength of the transverse shear waves, the boundary condition

$$v_x(y = \infty, t) = 0, \quad (3.25)$$

is appropriate. Neglecting the transient, a solution of the form  $v_x(y, t) = \mathcal{I}m\{\hat{v}_x(y)e^{it}\}$

is posited and may be obtained by Fourier method. Combining (3.10) and (3.11a), we have

$$\frac{\partial v_x}{\partial t} = \int_{-\infty}^t G(t-s) \frac{\partial^2 v_x(y, s)}{\partial y^2} ds \quad (3.26)$$

Inserting the posited velocity in (3.26), and eliminating the  $e^{it}$  term, we have the ordinary differential equation for  $\hat{v}$

$$\frac{d^2 \hat{v}_x}{dy^2} - \frac{iRe}{\eta^*} \hat{v}_x = 0. \quad (3.27)$$

where the nondimensional complex viscosity  $\eta^*$  follows the definition as in (1.8),  $\eta^* = \int_0^\infty G(s) \exp(-is) ds = \eta' - i\eta''$ .

We note the condition at infinity (3.25) ensure one of the solutions to (3.27) is selected as

$$v_x(y, t) = \mathcal{I}m\{e^{it} e^{-\delta y}\} = e^{-\alpha y} \sin(t - \beta y), \quad (3.28)$$

where the notation  $\delta = \alpha + i\beta = \sqrt{iRe/\eta^*}$  ( $\alpha, \beta \in \mathbb{R}$ ) has been introduced which leads to

$$\alpha = \frac{1}{|\eta^*|} \sqrt{\frac{Re}{2}(|\eta^*| - \eta'')}, \quad \beta = \frac{\eta'}{|\eta^*|} \sqrt{\frac{Re/2}{|\eta^*| - \eta''}}. \quad (3.29)$$

It is clear that  $0 < \alpha \leq \beta$ , with equality only in the viscous limit  $\eta'' = 0$  such that  $\alpha = \beta = \sqrt{Re/2}$ . The greater the elastic component  $\eta''$ , the larger the difference between oscillation wavelength  $2\pi/\beta$  and the attenuation length  $1/\alpha$ .

Recall we have the relation between complex modulus and complex viscosity in dimensional units,  $\tilde{G}^* = i\tilde{\omega}\tilde{\eta}^*$ , while in dimensionless unit,  $G^* = i\eta^*$ , we can recover  $G^*$  from (3.29):

$$G' = \frac{(\beta^2 - \alpha^2)Re}{(\alpha^2 + \beta^2)^2}, \quad G'' = \frac{2\alpha\beta Re}{(\alpha^2 + \beta^2)^2}. \quad (3.30)$$

From this nondimensional formulation, we can recover the formulas in Ferry, Sawyer, and Ashworth [25].

As for the particle displacement  $X(y, t)$ , we have the formulation

$$X(y, t) = X(y, 0) + e^{-\alpha y} [\cos(\beta y) - \cos(t - \beta y)]. \quad (3.31)$$

And the shear stress is obtained from (3.10) and (3.28)

$$\tau_{xy}(y, t) = \mathcal{I}m\{-\delta\eta^*e^{it}e^{-\delta y}\} = \sin(t - \beta y + \varphi + \pi)e^{-\alpha y}\sqrt{|\eta^*|Re}. \quad (3.32)$$

Since the normal stress is not considered here, the normal stress components are assumed zero too in this linear model. And we can see from (3.32) the phase shift of the shear stress with respect to the velocity (3.28) is  $\varphi + \pi$ , where  $\varphi = \arctan(\beta/\alpha)$ ,  $0 \leq \varphi \leq \pi/2$ .

As pointed out in [60], the comparison to viscous solution is informative. The ratio of the viscid to viscoelastic penetration lengths ( $\alpha/\alpha_0$ ) reveals that when  $\eta'' = 0$ , we obtain the expected increase in penetration depth as  $\eta'$  increases: a more viscous fluid leads to more momentum transfer from the oscillating plate! As the fluid elasticity  $\eta''$  increases, the penetration depth ratio decreases. Some of the momentum imparted to the fluid by the oscillating plate is now radiated as an elastic shear wave, hence the penetration depth is smaller. The ratio of viscid to viscoelastic wavelengths ( $\beta/\beta_0$ ) is also instructive. For viscoelastic fluids ( $\eta'' > 0$ ) the wavelength reflects the competition between diffusive and radiative momentum transfer. At a given  $\eta'$  an initial increase in the elasticity decreases the wavelength. In this range the motion is over damped and the decrease in penetration depth dominates the wavelength. At greater values of  $\eta''$  the radiative momentum transfer (through shear waves) becomes dominant and there is an increase in the wavelength. The maximum viscoelastic shear stress is greater than the purely viscous stress by a factor of  $\sqrt{|\eta^*|}$  and exhibits a different phase shift,  $\varphi + \pi$  instead of  $5\pi/4$ .

**Finite channel depth.** When the fluid is bounded above at  $y = H$  by a solid, flat plate moving at velocity  $v_H(t)$  the no-slip boundary condition is

$$v_x(y = H, t) = v_H(t) . \quad (3.33)$$

The Fourier method assumes steady state solution and requires the form of top boundary  $v_H(t) = V_H e^{it}$  with  $V_H$  complex constant giving the amplitude of top plate motion



(e.g.  $V_H(t) = r \exp(i\theta)$ , where  $r$  and  $\theta$  are real constant), and gives us the solution

$$\begin{aligned}
v_x(y, t) = & \frac{e^{-y\alpha}}{(1 + e^{4H\alpha} - 2e^{2H\alpha} \cos(2H\beta))} \left( e^{2(H+y)\alpha} \sin(2H\beta - y\beta - t) \right. \\
& - e^{4H\alpha} V_0 \sin(y\beta - t) - e^{3H\alpha+2y\alpha} r \sin(H\beta - y\beta - \theta - t) \\
& + e^{3H\alpha} r \sin((H+y)\beta - \theta - t\omega) - e^{2H\alpha} \sin(2H\beta - y\beta + t) \\
& + e^{2y\alpha} \sin(y\beta + t) + e^{H\alpha} r \sin(H\beta - y\beta + \theta + t) \\
& \left. - e^{(H+2y)\alpha} r \sin((H+y)\beta + \theta + t) \right), \tag{3.34}
\end{aligned}$$

which can be rewritten in the form proposed by Mitran as:

$$v_x(y, t) = \mathcal{I}m \left\{ V_0 e^{i\omega t} \frac{\sinh[\delta(H-y)]}{\sinh(\delta H)} + v_H(t) \frac{\sinh(\delta y)}{\sinh(\delta H)} \right\}. \tag{3.35}$$

And the stationary top plate solution is included here with  $V_H = 0$ . (This "textbook" solution does not appear to be in the literature; it is given here for explicit comparison with the semi-infinite solution, and since it is the basis for finite-depth inverse characterization.)

We note here the infinite half-plane solution is recovered from (3.35), since

$$\frac{\sinh[\delta(H-y)]}{\sinh(\delta H)} = e^{-\delta y} - 2 \sinh(\delta y) \frac{e^{-2\delta H}}{1 - e^{-2\delta H}}, \tag{3.36}$$

and (note  $\delta = \alpha + i\beta$  and  $\alpha > 0$ )

$$\lim_{H \rightarrow \infty} \frac{\sinh[\delta(H-y)]}{\sinh(\delta H)} = e^{-\delta y}. \tag{3.37}$$

So taking the limit of  $H$  to the infinity, setting  $v_H(t) = 0$  and taking the imaginary part of the result gives (3.28).

The shear stress is given by

$$\tau_{xy}(y, t) = \mathcal{I}m \left\{ -\delta \eta^* \frac{\cosh[\delta(H-y)]}{\sinh(\delta H)} e^{it} \right\}. \tag{3.38}$$

**Finite channel depth, flat fluid boundary above.** The boundary condition in this case is continuity of tangential stress within the viscoelastic fluid  $\tau_{yx}(H, t)$  with that from the adjacent fluid  $\tau_H(t)$ . Since we neglect the transients, the adjacent fluid must exhibit a tangential stress dependence of the form  $\tau_H(t) = T_H e^{it}$  to be consistent with the Fourier method. This leads to

$$\frac{dv_x^0}{dy}(y = H) = \frac{\tau_H(t)}{\eta^*} e^{-i\omega t} \quad (3.39)$$

and the solution

$$v_x(y, t) = \mathcal{Im} \left\{ V_0 e^{i\omega t} \frac{\sinh[\delta(H - y)]}{\sinh(\delta H)} + \frac{\tau_H(t)}{\delta \eta^*} \frac{\sinh(\delta y)}{\sinh(\delta H)} \right\}. \quad (3.40)$$

This solution is relevant if one solves the model equations for the fluid layer above, or designs an experiment with a controlled dynamic shear stress at the interface. (This solution is proposed by Mitran [60] and likewise appears not to have been previously published.) It should be noted however that ensuring that the top fluid layer has the simple harmonic tangential stress  $H(t) = T_H e^{it}$  is difficult to realize experimentally. If the adjacent fluid exerts negligible stress upon the viscoelastic fluid layer  $T_H \approx 0$ , then the formula

$$v_x(y, t) = \mathcal{Im} \left\{ V_0 e^{i\omega t} \frac{\sinh[\delta(H - y)]}{\sinh(\delta H)} \right\}, \quad (3.41)$$

is proper. Otherwise, it is to be expected that  $H(t)$  contains other frequencies besides the fundamental frequency used in the bottom plate forcing, and solution (3.40) should be used.

**Limitations of linear viscoelastic model.** The Lodge type constitutive equation (3.10) is valid for small strain limit

$$\max |D_{xy}| = \max \left| \frac{\partial X}{\partial y} \right| = \max \left| \frac{\partial}{\partial y} \int_0^t v_x(y, s) ds \right| \ll 1. \quad (3.42)$$

For semi-infinite domain solution (3.31), the strain is

$$\max |D_{xy}| = e^{-\alpha y} \{ \alpha [\cos(t - \beta y) - \cos(\beta y)] + \beta [\sin(t - \beta y) + \sin(\beta y)] \}, \quad (3.43)$$

with initial condition  $X(y, 0) = 0$ . The reasonable assumption is that the maximum strain is obtained at lower plate  $y = 0$ ,

$$\max |D_{xy}(y = 0, t)| = -\alpha(1 - \cos t) - \beta \sin t. \quad (3.44)$$

And the maximum is obtained when  $\cos t = \alpha/\sqrt{\alpha^2 + \beta^2}$  and  $\sin t = -\beta/\sqrt{\alpha^2 + \beta^2}$ , and we have

$$\max |D_{xy}| = \sqrt{\alpha^2 + \beta^2} - \alpha. \quad (3.45)$$

Notice  $\sqrt{\alpha^2 + \beta^2} = \sqrt{Re/|\eta^*|}$ , the small strain limit becomes

$$\sqrt{\frac{Re}{|\eta^*|}} \left(1 - \sqrt{\frac{|\eta^* - \eta''|}{2|\eta^*|}}\right) \ll 1. \quad (3.46)$$

The elastic limit of fluid behavior corresponds to  $\eta'' \gg \eta'$ , so the condition becomes

$$Re \ll \eta'',$$

in this limit. We revert the relation into physical units to highlight the significance of these limits. Recall that  $Re = \tilde{\rho}\tilde{\omega}\tilde{A}^2/\tilde{\eta}_0$  and  $\tilde{G}' = \tilde{\omega}\tilde{\eta}''$ . The condition in the elastic limit is then

$$\tilde{\rho}(\tilde{\omega}\tilde{A})^2 \ll \tilde{G}', \quad (3.47)$$

or, physically, that the dynamic pressure induced by the oscillating plate must be much less than the elasticity modulus of the fluid. In the viscous limit  $\eta' = 1, \eta'' = 0$ , the small-strain condition becomes  $Re \ll 1$ . In the physical terms this states that

$$\tilde{A} \ll \tilde{d} = \sqrt{\tilde{\omega}/2\tilde{\eta}/\tilde{\rho}},$$

or that the amplitude of the oscillating bottom plate,  $\tilde{A}$  must be much less than the viscous penetration depth  $\tilde{d}$ . If viscous and elastic effects are roughly equal, then the

small strain condition becomes

$$Re \ll \min(\eta', \eta'').$$

The coefficients  $(\eta', \eta'')$  obtained from fitting experimental data to the formulas above should be checked against these limits to ascertain whether non-linear effects are insignificant. In the finite depth linear and nonlinear models, one can calculate the local strain from the numerical solutions, which generically will be maximal in the first half-wavelength of the shear deformation at the lower plate.

### 3.3 Solutions to nonlinear model at special limits

The model equations with nonlinear viscoelastic constitutive law discussed above are hyperbolic in nature. We will analyze the hyperbolicity of the system here to prepare the presentation of numerical scheme proper for hyperbolic system, and we specially mention the way of imposing consistent boundary conditions for those system. Also, we have to point out the analysis on the nonlinear model are difficult and the analytical solutions are usually very hard to get. We will only consider one exactly solvable case here.

#### 3.3.1 Hyperbolic structure

We now turn to a consideration of nonlinear effects by solving (3.20). The matrix  $A$  from (3.20) has eigenvalues  $\mu_1 = \mu_2 = 0$ ,  $\mu_3 = -c$ ,  $\mu_4 = c$  with

$$c = \sqrt{\frac{\eta_p + \lambda\tau_{yy}}{\lambda Re}}$$

denoting the velocity of propagation of shear waves transverse to the flow direction. It's clear that for elastic fluid whose normal stress component  $\tau_{yy} > \eta_p/\lambda$ , the system (3.20) is hyperbolic; if the stress condition is violated, say  $\tau_{yy} < \eta_p/\lambda$ , the system will

be elliptic with complex  $c$ . The associated right eigenvectors of  $A$  are

$$R = \begin{bmatrix} r_1 & r_2 & r_3 & r_4 \end{bmatrix} = \begin{bmatrix} 0 & 0 & c & -c \\ 0 & 1 & 2\tau_{xy} & 2\tau_{xy} \\ 0 & 0 & c^2 Re & c^2 Re \\ 1 & 0 & 0 & 0 \end{bmatrix}. \quad (3.48)$$

The eigenvectors form a basis for  $c > 0$ , hence the system (3.20) is hyperbolic. The structure of this system is particularly simple with multiplicity two non-propagating characteristic speed. This allows considerable analytical progress. Consider a local linearization in which use average values (denoted by an overbar) for the eigenvectors

$$\bar{R} = \begin{bmatrix} 0 & 0 & \bar{c} & -\bar{c} \\ 0 & 1 & 2\bar{\tau}_{xy} & 2\bar{\tau}_{xy} \\ 0 & 0 & \bar{c}^2 Re & \bar{c}^2 Re \\ 1 & 0 & 0 & 0 \end{bmatrix}$$

The characteristic variables of the problem are

$$w = \begin{bmatrix} w_1 \\ w_2 \\ w_3 \\ w_4 \end{bmatrix} = \bar{R}^{-1}q = \begin{bmatrix} 0 & 0 & 0 & 1 \\ 0 & 1 & -\frac{2\bar{\tau}_{xy}}{\bar{c}^2 Re} & 0 \\ \frac{1}{2\bar{c}} & 0 & \frac{1}{2\bar{c}^2 Re} & 0 \\ -\frac{1}{2\bar{c}} & 0 & \frac{1}{2\bar{c}^2 Re} & 0 \end{bmatrix} \begin{bmatrix} v_x \\ \tau_{xx} \\ \tau_{xy} \\ \tau_{yy} \end{bmatrix} = \begin{bmatrix} \tau_{yy} \\ \tau_{xx} - \frac{2\bar{\tau}_{xy}}{\bar{c}^2 Re} \tau_{xy} \\ \frac{1}{2\bar{c}} v_x + \frac{1}{2\bar{c}^2 Re} \tau_{xy} \\ -\frac{1}{2\bar{c}} v_x + \frac{1}{2\bar{c}^2 Re} \tau_{xy} \end{bmatrix},$$

and (3.20) can be rewritten in terms of these variables as

$$\frac{\partial w}{\partial t} + \Lambda \frac{\partial w}{\partial y} = \phi \quad (3.49)$$

with  $\Lambda = \text{diag} \{ \mu_1, \mu_2, \mu_3, \mu_4 \}$  and  $\phi = R^{-1}\psi$ ,

$$\phi = -\frac{1}{\lambda} \begin{bmatrix} \tau_{yy} + a(\tau_{xy}^2 + \tau_{yy}^2) \\ \tau_{xx} + a(\tau_{xy}^2 + \tau_{xx}^2) - 4\bar{\tau}_{xy}\sigma \\ \sigma \\ \sigma \end{bmatrix}, \quad \sigma = \frac{1}{2\bar{c}^2 Re} \tau_{xy} (1 + a(\tau_{xx} + \tau_{yy})) .$$

The forcing term  $\phi$  can be rewritten as a function of the characteristic variables  $\phi = \phi(w)$  by using

$$q = \begin{bmatrix} v_x \\ \tau_{xx} \\ \tau_{xy} \\ \tau_{yy} \end{bmatrix} = \bar{R}w = \begin{bmatrix} 0 & 0 & \bar{c} & -\bar{c} \\ 0 & 1 & 2\bar{\tau}_{xy} & 2\bar{\tau}_{xy} \\ 0 & 0 & \bar{c}^2 Re & \bar{c}^2 Re \\ 1 & 0 & 0 & 0 \end{bmatrix} \begin{bmatrix} w_1 \\ w_2 \\ w_3 \\ w_4 \end{bmatrix} = \begin{bmatrix} \bar{c}(w_3 - w_4) \\ w_2 + 2\bar{\tau}_{xy}(w_3 + w_4) \\ \bar{c}^2(w_3 + w_4)Re \\ w_1 \end{bmatrix} . \quad (3.50)$$

### 3.3.2 Characteristic boundary conditions

The hyperbolic structure of the problem indicates that the compatible boundary conditions must be used in numerical simulations. The non-propagating quantities  $w_1 = \tau_{yy}$  and  $w_2 = \tau_{xx} - \frac{2\bar{\tau}_{xy}}{\bar{c}^2 Re} \tau_{xy}$  can be freely specified on both bottom and top boundaries. Subsequent values must be determined by solving the following ODE at each boundary

$$\begin{aligned} \frac{\partial \omega_1}{\partial t} &= -\frac{1}{\lambda} [\tau_{yy} + a(\tau_{xy}^2 + \tau_{yy}^2)], \\ \frac{\partial \omega_2}{\partial t} &= -\frac{1}{\lambda} [\tau_{xx} + a(\tau_{xy}^2 + \tau_{xx}^2) - 4\bar{\tau}_{xy}\sigma]. \end{aligned} \quad (3.51)$$

At the bottom plate ( $y = 0$ ) only the in-going characteristic variable  $w_4 = -\frac{1}{2\bar{c}}v_x + \frac{1}{2\bar{c}^2 Re}\tau_{xy}$  quantity can be specified since it is propagating into the fluid from the the fluid domain. The other characteristic variable  $w_3 = \frac{1}{2\bar{c}}v_x + \frac{1}{2\bar{c}^2 Re}\tau_{xy}$  propagates from within the fluid domain towards the boundary and *must* be determined as part of the solution procedure. Conversely, at the top boundary ( $y = H$ )  $w_3$  can be given as a boundary condition and  $w_4$  *must* be evaluated from the solution procedure. Typically, we wish to give boundary conditions in terms of the physical variables. The essence of the above

discussion is that we cannot impose both velocity  $v_x$  and shear stress  $\tau_{xy}$  at boundaries. To do so would determine both  $w_3$  and  $w_4$  in violation of characteristic information propagation directions. We list common cases of compatible boundary conditions.

1. Velocity and normal stresses. At the bottom plate we specify  $v_x$  and propagation from within the channel as specified by the characteristic equation

$$\frac{\partial \omega_3}{\partial t} - c \frac{\partial \omega_3}{\partial y} = -\frac{\sigma}{\lambda}, \quad (3.52)$$

to give  $w_3$ . This allows  $\tau_{xy} = 2\bar{c}^2 Re(w_3 - \frac{1}{2\bar{c}}v_x)$  to be computed. We solve (3.51) to obtain  $w_1, w_2$ . By using (3.50), we then can specify  $\tau_{yy}$  and  $\tau_{xx}$  thereby obtaining all the variables of the  $q$  vector. At the top plate we proceed analogously, by specifying  $v_x$  but obtaining  $\tau_{xy}$  from the  $w_4$  component as  $\tau_{xy} = 2\bar{c}^2 Re(w_4 + \frac{1}{2\bar{c}}v_x)$ . The  $\omega_4$  component is determined from propagation within the fluid by solving

$$\frac{\partial \omega_4}{\partial t} + c \frac{\partial \omega_4}{\partial y} = -\frac{\sigma}{\lambda}. \quad (3.53)$$

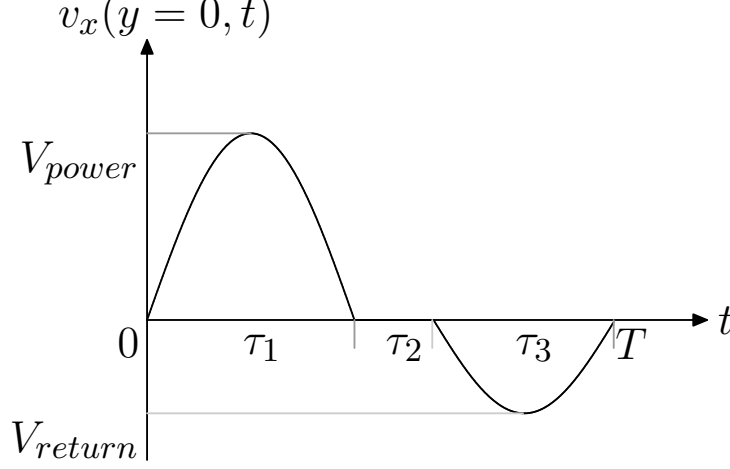
2. Tangential and normal stresses. At both boundaries we specify  $\tau_{xy}$ . Solving (3.51) gives  $\omega_1, \omega_2$  and hence  $\tau_{yy}, \tau_{xx}$ . At the bottom boundary, velocity  $v_x$  is obtained from the propagating  $\omega_3$  component by solving (3.52) and at the top from the  $\omega_4$  component obtained by solving (3.53).
3. Non-reflective top boundary condition. To simulate an infinite domain we can set the in-coming characteristic at  $y = H$  to zero,  $w_3 = 0$ . Numerically, care must be taken so there are no spurious reflections of the  $\omega_4$  component at the  $y = H$  boundary.

Also, it is worth to point out we can mimic cilia beating pattern by impose asymmetric lower boundary condition. As showed in Figure 3.3.2, we model this motion by the plate velocity in one period  $T$

$$V(t) = \begin{cases} V_{power} \sin(\pi t / \tau_1), & 0 \leq t \leq \tau_1 \\ 0, & \tau_1 \leq t \leq \tau_1 + \tau_2 \\ -V_{return} \sin(\pi(t - (\tau_1 + \tau_2)) / \tau_3), & \tau_1 + \tau_2 \leq t \leq \tau_1 + \tau_2 + \tau_3, \end{cases} \quad (3.54)$$

where  $\tau_1 + \tau_2 + \tau_3 = T = 2\pi$  (in dimensionless form, and the dimensional period

Figure 3.2: Schematic sketch of asymmetric lower boundary condition for velocity, with effect of net shift to the right showed



$\tilde{T} = 2\pi/\tilde{\omega}$ ). We can see, from (3.54),  $(V_{power}, \tau_1)$  and  $(V_{return}, \tau_3)$  give us the parameter sets to adjust the net drift to right which mimics the slip boundary condition at bottom ‘plate’. And since

$$\Delta x|_{power} = \int_0^{\tau_1} V_{power} \sin(\pi t/\tau_1) dt = \frac{2\tau_1}{\pi} V_{power}, \quad (3.55)$$

and

$$\Delta x|_{return} = -\frac{2\tau_3}{\pi} V_{return}, \quad (3.56)$$

the no-slip boundary condition implies  $\tau_1 V_{power} = \tau_3 V_{return}$ . Otherwise the average net drift velocity could be determined by

$$V_{drift} = \frac{2}{\pi} \frac{\tau_1 V_{power} - \tau_3 V_{return}}{\tau_1 + \tau_2 + \tau_3}. \quad (3.57)$$

There are several ways to parameterize the net drift with those numbers: one is to keep the velocity amplitude same and then adjust time spend on forward, relax and backward, eg.  $\tau_1 = T/2, \tau_3 = T/2 - \tau_2$  with  $0 \leq \tau_2 \leq T/2$ ; another one is to set  $\tau_1 = \tau_3$  and then  $\tau_2 = 0$ , then  $V_{power} = \alpha V_{return}$  with  $0 < \alpha \leq 1$ .

The analysis of boundary conditions not only sheds light on the model study for finite depth shear wave, but also useful to our numerical analysis for full  $2d$  simulation,



in which the hyperbolic part of the problem again need similar treatment to maintain the numerical procedure stable and convergent. We will talk about this in next chapter.

### 3.3.3 Upper Convected Maxwell solution

For general nonlinear viscoelastic model, the analytical solution is hard to obtain, but here we present an analytical solution for UCM model.

We recall the UCM model system is,  $a = 0$  in (3.20),

$$\left\{ \begin{array}{l} \frac{\partial v_x}{\partial t} - \frac{1}{Re} \frac{\partial \tau_{xy}}{\partial y} = 0 \\ \frac{\partial \tau_{xx}}{\partial t} - 2\tau_{xy} \frac{\partial v_x}{\partial y} = -\frac{1}{\lambda} \\ \frac{\partial \tau_{xy}}{\partial t} - \left(\frac{\eta_p}{\lambda} + \tau_{yy}\right) \frac{\partial v_x}{\partial y} = -\frac{1}{\lambda} \tau_{xy} \\ \frac{\partial \tau_{yy}}{\partial t} = -\frac{1}{\lambda} \tau_{yy} \end{array} \right. \quad (3.58)$$

with an immediate solution for  $\tau_{yy}(y, t) = \tau_{yy}(y, 0) \exp(-t/\lambda)$ . The analytical solution given by Mitran via Riemann method [60] is shown below. (In the analysis, the assumption  $\tau_{yy}(y, 0) = 0$  is taken)

$$v_x(y, t) = \frac{1}{2} e^{-\frac{t}{2\lambda}} u(y, t), \quad (3.59)$$

with

$$u(y, t) = \frac{1}{2} [U(y - ct) + U(y + ct)] + \int_{y-ct}^{y+ct} [K(s, y, t)U(s) + L(s, y, t)V(s)] ds, \quad (3.60)$$

and

$$K(s, y, t) = \frac{t}{8\lambda^2 c} \frac{J_1(r(s, y, t))}{r(s, y, t)}, \quad L(s, y, t) = \frac{1}{2c} J_0(r(s, y, t)). \quad (3.61)$$

And function  $U(y)$  in (3.59) is solved from

$$U(y) = \mu \int_y^0 M(s, y) U(s) ds + F(y), \quad (3.62a)$$

$$M(s, y) = -\frac{y}{\sqrt{y^2 - s^2}} J_1\left(\frac{1}{2\lambda c} \sqrt{y^2 - s^2}\right) \quad (3.62b)$$

$$F(y) = -4e^{-y/(2\lambda c)} \sin \frac{y}{c}, \mu = \frac{1}{2\lambda c}. \quad (3.62c)$$

And the shear stress  $\tau_{xy}$  is given by

$$\tau_{xy}(y, t) = \frac{Re}{2} e^{-t/2\lambda} \int_{y+ct}^y \left[ \frac{\partial u}{\partial t}(s, t) \frac{1}{2\lambda} u(s, t) \right] ds. \quad (3.63)$$

After knowing  $v_x$  and  $\tau_{xy}$ , we can construct the solution for the normal stress component  $\tau_{xx}$  from (3.58).

The upshot of this solution formula is that we can capture the nonlinearity of normal stress generation in shear flow, and this effect is completely ignored in the linear model.

## 3.4 High resolution numerical computation

### 3.4.1 Numerical scheme

For the more general nonlinear constitutive laws of Giesekus type with shear thinning ( $a \neq 0$ ), closed-form solutions do not exist, so numerical methods are employed. A primary purpose of this study is to provide a basis for inverse characterization of nonlinear viscoelastic properties. Hence it is desirable to minimize any artificial dissipation and dispersion that might arise in a numerical computation, which is the baseline for matching with experimental data through parameter fitting. For this purpose, we apply a high-resolution algorithm [15] for hyperbolic PDEs as implemented in the Clawpack [17] or Bearclaw packages [16]. We present the salient points of the numerical method here for completeness. It is a finite volume, Godunov-type method in which the jumps between adjacent finite volume cell averages are propagated in accordance with local wave speeds. Consider an uniform discretization of the interval  $[0, H]$  with step size  $h$ . The cell center coordinates are  $y_j = (j - 1/2)h$  for  $j = 1, 2, \dots, m$  with  $h = H/m$ , and the cell edge coordinates are  $y_{j-1/2} = (j - 1)h$  for  $j = 1, 2, \dots, m + 1$ . The cell finite

volume average is

$$Q_j^n = \frac{1}{h} \int_{y-1/2}^{y+1/2} q(y, t^n) dy. \quad (3.64)$$

The numerical method presented here is based on [48].

We first rewrite the system (3.20) with operators

$$\mathbf{q}_t = (\mathcal{A} + \mathcal{B})(\mathbf{q}), \quad \mathcal{A} = -\mathbf{A}(\mathbf{q}) \frac{\partial}{\partial x}, \mathcal{B} = -\psi(\mathbf{q}), \quad (3.65)$$

where  $\mathcal{A}$  is the convective operator and  $\mathcal{B}$  is the source term operator. Computation of (3.65) is split into two steps with Strang splitting:

$$\mathbf{q}(t + \Delta t) = e^{(\mathcal{A} + \mathcal{B})\Delta t} \mathbf{q}(t) \approx e^{\mathcal{B}\Delta t/2} e^{\mathcal{A}\Delta t} e^{\mathcal{B}\Delta t/2} \mathbf{q}(t). \quad (3.66)$$

The source term of the splitting is  $\mathbf{q}_t = \mathcal{B}(\mathbf{q})$ , a system of ordinary differential equations which is advanced by using a second order Runge-Kutta scheme. For the convective part of equation, jumps between adjacent cells as propagating waves are first presented. The jump at the  $j - 1/2$  cell interface  $\Delta \mathbf{Q}_{j-1/2}^n$ , is decomposed on the eigen basis  $\bar{R} = R((Q_j^n + Q_{j-1}^n)/2)$

$$\Delta \mathbf{Q}_{j-1/2}^n = \mathbf{Q}_j^n - \mathbf{Q}_{j-1}^n = \sum_{l=3}^4 \alpha_{j-1/2}^l \mathbf{r}_{j-1/2}^l, \mathcal{W}_{j-1/2}^l = \alpha_{j-1/2}^l \mathbf{r}_{j-1/2}^l, l=3, 4. \quad (3.67)$$

Note only the  $r_3, r_4$  eigen mode from (3.48) are propagating in the system, hence number of waves  $n_w = 2$ ,  $\mathcal{W}_{j-1/2}^{3,4}$  are required. The  $\alpha$  coefficients are

$$\alpha_{j-1/2}^3 = \frac{\Delta Q_{3,j-1/2}}{2\bar{c}_{j-1/2}^2 Re} - \frac{\Delta Q_{1,j-1/2}}{2\bar{c}_{j-1/2}^2}, \alpha_{j-1/2}^4 = \frac{\Delta Q_{3,j-1/2}}{2\bar{c}_{j-1/2}^2 Re} + \frac{\Delta Q_{1,j-1/2}}{2\bar{c}_{j-1/2}^2}, \quad (3.68)$$

with  $Q_1, Q_3$  the 1, 3 components of  $\mathbf{Q}$ . Cell average values are updated by

$$Q_j^{n+1} = Q_j^n - \frac{\Delta t}{h} (\mathcal{W}_{j-1/2}^4 + \mathcal{W}_{j+1/2}^3), \quad (3.69)$$

along with second order corrections (details can be found in [47]). The program based on

this numerical scheme is setup within Bearclaw. In the spirit of Literate Programming [37], all software details are available both in Bearclaw package and on a website [32].

### 3.4.2 Experimental design guidelines

The high resolution numerical method presented above enables us to test various boundary conditions. We can apply the numerical algorithm to show the effect of experimentally relevant boundary conditions. In the results we showed, parameters are chosen  $H = 10$ ,  $\eta_p = 1$ ,  $\lambda = 4$ ,  $Re = 1$ ,  $a = 0$  and  $\tau_{yy} = 0$ . Results are presented in Figure 3.3 by showing superimposed snapshots of  $v_x(y, t_n)$ ,  $\tau_{xx}(y, t_n)$ ,  $\tau_{xy}(y, t_n)$  at times  $t_n = n\Delta t$ ,  $n = 0, 1, \dots, 30$ , with time increment  $\Delta t = 1.9$ . Also shown are subsequent time positions of tracer beads initially placed at  $X(y, 0) = 0$ . Since  $\tau_{yy} = 0$  in these simulations the normal stress difference is directly given by  $\tau_{xx}$ ,  $N_1 = \tau_{xx} - \tau_{yy} = \tau_{xx}$ .

**Open-cell experiment.** In an open-cell experimental setup the viscoelastic fluid is typically in contact with the surrounding air which is assumed to exert a negligible tangential stress upon the viscoelastic layer. The top boundary at  $y = 0$  is assumed to be flat. Hence the boundary condition  $\tau_{xy}(H, t) = 0$  is set. Results for this case are shown in Figure 3.3. Note that the nonlinear interaction terms in the UCM model lead to large values of  $\tau_{xx}$ , larger than those for  $\tau_{xy}$  near the plate.

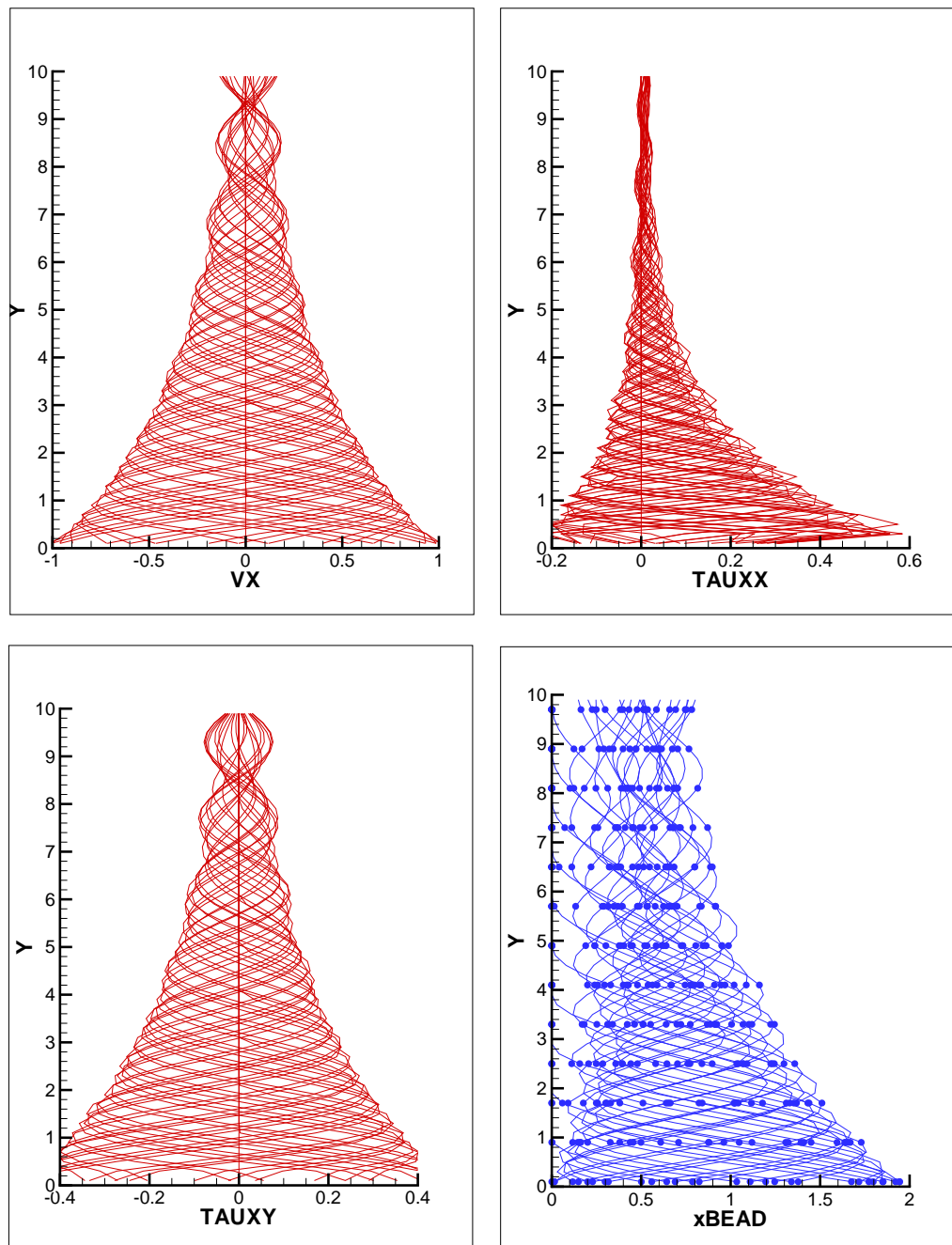
**Stationary top plate.** A closed-cell experimental setup is advantageous in ensuring isolation of the sample and surrounding medium. Typical results are shown in Fig. 10 when the top plate is kept at zero velocity  $v_x(H, t) = 0$ . An interesting observation is that the velocity and stress profiles are very similar to those obtained in the open-cell experiment. The main difference is the much smaller range of motion exhibited by tracer beads when the top plate is stationary by comparison to the open-cell experimental setup. If signal-to-noise ratio of tracer bead positions becomes a concern at low strain thresholds, then the open-cell setup is preferable.

#### Asymmetric lower boundary condition

To demonstrate the ability to mimic cilia beating pattern, we show the computation results with lower boundary velocity assigned as in (3.54). The simulation parameters of the above example are also used here, and we set  $V_{power} = 3$ ,  $V_{return} = 1$ ,  $\tau_1 = 3.14$ ,  $\tau_2 = \tau_3 = 1.57$ .

In Figure 3.4, solid wall velocity boundary condition is applied at top plate, and consistent normal stress boundary condition as discussed in section 3.3.2 are also ap-

Figure 3.3: Numerical results with symmetric lower boundary condition  $v(y = 0, t) = \sin(t)$ , with open-cell boundary condition at top plate ( $\tau_{xy} = 0$  assigned at the top).



plied. The results on bead deformation indicate there is no bead movement at top plate, and the normal stress at bottom plate are much higher than tangential stress.

In Figure 3.5, open-cell boundary condition is applied at top plate, and velocity is calculated consistently according to section 3.3.2. We clearly see net transport of tracer beads and again, the normal stress at bottom plate are much higher than tangential stress. This model setup and boundary condition enable us to study the mucus layer transport by cilia driving, and can predict the rate of net transport for mucus.

Figure 3.4: Numerical results of the asymmetric lower boundary condition, with  $V_{power} = 3$ ,  $V_{return} = 1$ ,  $\tau_1 = 3.14$ ,  $\tau_2 = \tau_3 = 1.57$ , and the stationary plate boundary condition at top plate ( $v(y = H, t) = 0$ ).

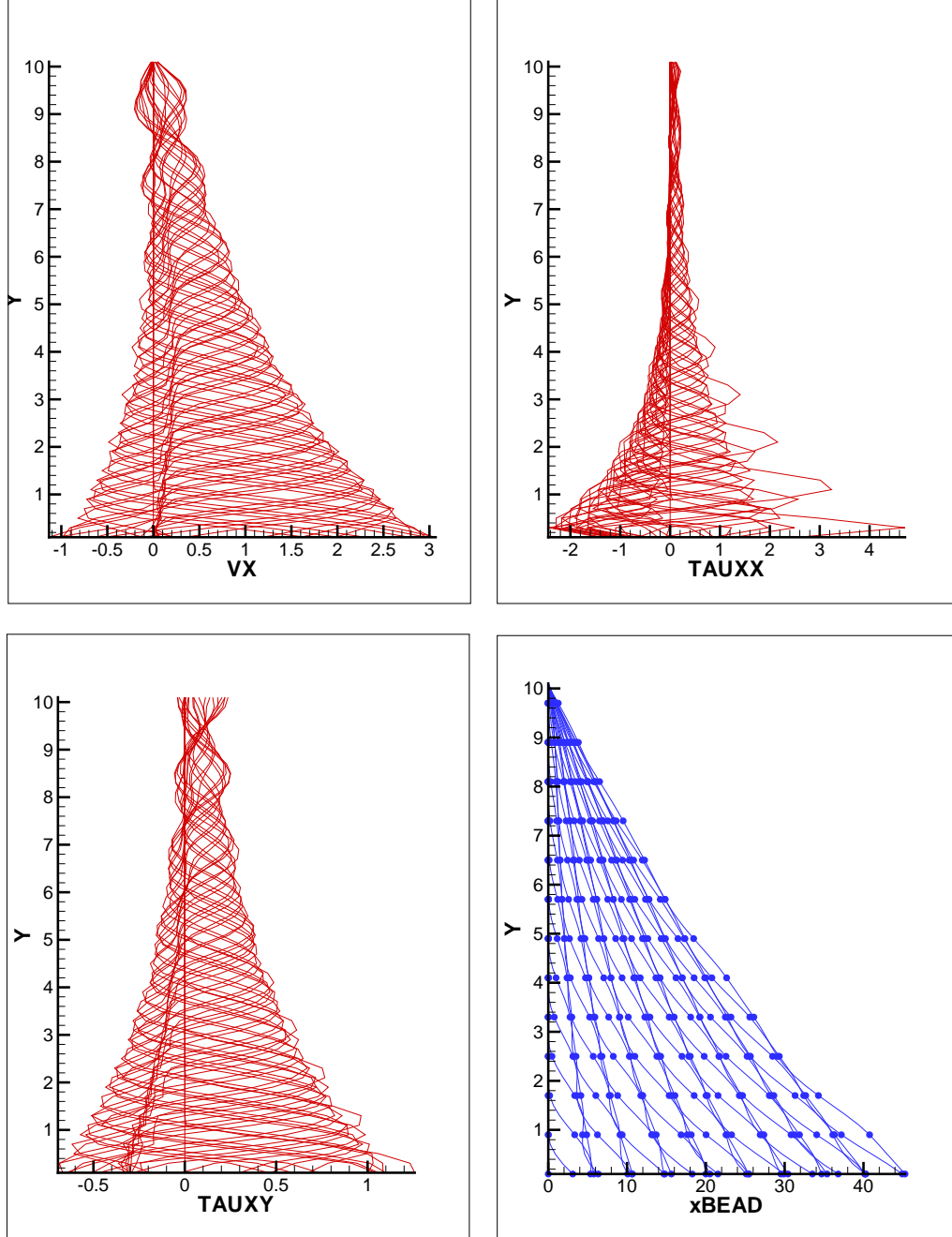
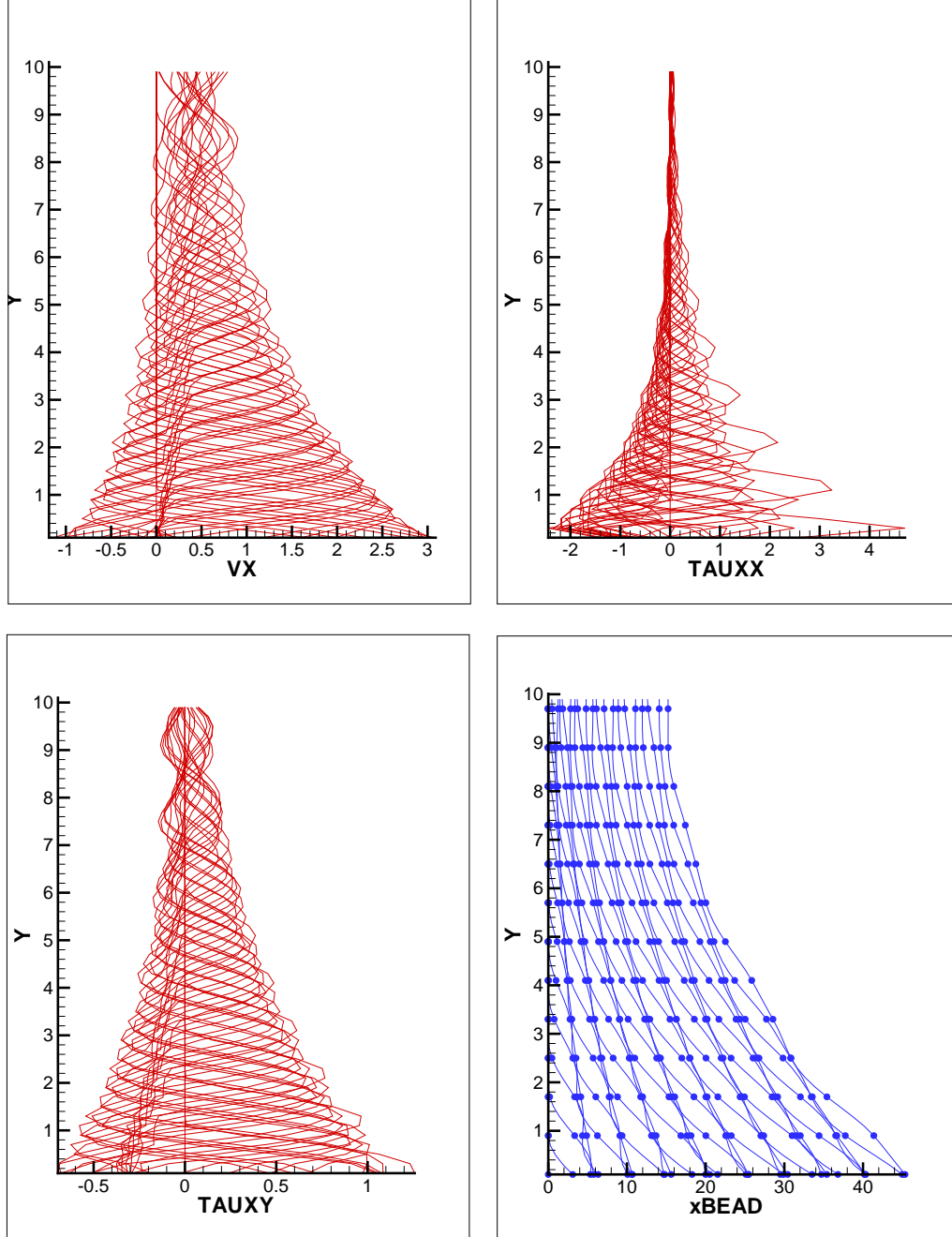


Figure 3.5: Numerical results with the asymmetric lower boundary condition, with  $V_{power} = 3$ ,  $V_{return} = 1$ ,  $\tau_1 = 3.14$ ,  $\tau_2 = \tau_3 = 1.57$ , and the open-cell boundary condition at top plate (the tangential stress  $\tau_{xy} = 0$  is at the top boundary)





# Chapter 4

## Numerical simulation at continuum level

As mentioned in the introduction chapter, transport of mucus layer itself is an important issue for lung functionality and one of our primary interests. Transport of the mucus layer is a cooperative outcome of the pulmonary system, and cilia beating and tidal breathing cycles are the main driving forces of the transport. Due to the fact of lacking understanding to details of the coupling between cilia/PCL and the mucus layer, we will simplify the model system to consider only the mucus layer itself with prescribed boundary conditions, which hopefully represents the stress/velocity communication from adjacent layers.

In this chapter, we model the viscoelasticity of mucus by Oldroyd-B differential constitutive law, and couple the corresponding extra stress evolution to momentum balance equation; with the assumption of incompressibility for mucus, we have the continuity equation to close the system of velocity, pressure, and stress components from viscous and elastic effect. To predict mucus flow, we study numerical schemes for the system, and discuss their stability of those numerical methods. In the literature, previous works on numerical methods for viscoelastic flows show loss of stability due to highly elastic effect of viscoelastic system and the necessity of particular care to treat the elastic stress components of the system was pointed out in summaries of previous numerical work [67, 35]. We will go through the physical and mathematical properties of the equation system and then present our choice of model for extra stress evolution; and we also try to identify the difficulty in simulation while restating numerical

methods proposed previously in the literature. By analyzing the detailed procedure of discretization to the system and considering the special constraint on the discrete variables, we present a new numerical scheme to simulate unsteady Oldroyd-B fluid flow. We show the underlying physical and mathematical interpretation of the method and also point out its advantage over previous classical numerical approaches. Also, to overcome the nonphysical assumption of the microscopic foundation of Oldroyd-B model, the Hookean dumbbell, we also study the FENE-P dumbbell and its constitutive equation. Based on approximation expansion of the stress of FENE-P, we can analyze the nonlinear correction to the numerical method we proposed for Oldroyd-B model. The results presented in this chapter are collaboration work with Sorin Mitran [61].

## 4.1 Viscoelastic fluid flow models

The momentum equation of viscoelastic flow for velocity  $\mathbf{v}$  is formulated as (in dimensional units)

$$\rho\left(\frac{\partial \mathbf{v}}{\partial t} + (\mathbf{v} \cdot \nabla)\mathbf{v}\right) = \nabla \cdot \boldsymbol{\pi} + \mathbf{f} \quad (4.1)$$

where  $\rho$  is the fluid density, the total stress tensor is denoted by  $\boldsymbol{\pi}$  and  $\mathbf{f}$  is the external force applied to fluid flow. Furthermore, the total stress is usually decomposed into isotropic part of pressure  $p$ , and the extra stress tensor  $\boldsymbol{\tau}$ :

$$\boldsymbol{\pi} = -p\mathbf{I} + \boldsymbol{\tau}. \quad (4.2)$$

When incompressibility assumption is taken, we have the continuity constraint equation for the velocity

$$\nabla \cdot \mathbf{v} = 0. \quad (4.3)$$

To close the system of equations (4.1)–(4.3) for viscoelastic fluid flow, we have to include a governing equation for extra stress  $\boldsymbol{\tau}$ . The constitutive equations describing the evolution of extra stress  $\boldsymbol{\tau}$  are proposed both in integral and differential equation form in literature, (cf. [7, 46, 45]), and they are used to capture relation between strain/rate-of-strain *vs.* stress response for viscoelastic material. We will apply constitutive laws in differential form in this chapter, and those in integral form are not our topics here.

### 4.1.1 Note on viscous case

We notice the situation in which only viscous stress is considered in (4.2),

$$\boldsymbol{\tau}_s = \eta_s(\nabla \mathbf{v} + \nabla \mathbf{v}^T), \quad (4.4)$$

where  $\eta_s$  is fluid viscosity. From (4.2) and (4.4), we will have standard Navier-Stokes (NS) equation in (4.1).

$$\rho\left(\frac{\partial \mathbf{v}}{\partial t} + (\mathbf{v} \cdot \nabla) \mathbf{v}\right) = -\nabla p + \eta_s \nabla^2 \mathbf{v} + \mathbf{f}. \quad (4.5)$$

With continuity equation (4.3) and (4.5), we have the incompressible Navier-Stokes equation, which is the standard model for viscous fluid flow. The above momentum equation (4.5) can be written in dimensionless form (without external force  $\mathbf{f}$ ):

$$\frac{\partial \mathbf{v}}{\partial t} + (\mathbf{v} \cdot \nabla) \mathbf{v} = -\nabla p + \frac{1}{Re} \nabla^2 \mathbf{v}, \quad (4.6)$$

where  $Re = \rho UL/\eta_s$  with characteristic fluid velocity of the flow  $U$  and the characteristic length of the flow problem  $L$ .

As pointed out in literature [14, 81], the incompressible Navier-Stokes equation admits mixed type properties with hyperbolic, elliptic and parabolic part existing in the same system. The elliptic part of the equation needs the full coupling of discretization of variables in numerical scheme to solve the equation, which means very expensive computational work required. The idea of splitting procedure based on Helmholtz-Hodge decomposition [14] allows decoupling of the computation of velocity and pressure field, and then leads to much more efficient numerical scheme of projection method by Chorin and Temam [15, 81], whose procedure is as followed: (given previous time step values of  $\mathbf{v}^n$  and  $p$ )

- (i) Advance velocity without pressure (we take the first order in time projection as example) to get intermediate velocity  $\mathbf{v}^*$ :

$$Re\left(\frac{\mathbf{v}^* - \mathbf{v}^n}{\Delta t}\right) = \nabla^2 \mathbf{v}^n - Re(\mathbf{v}^n \cdot \nabla) \mathbf{v}^n; \quad (4.7)$$

(ii) Update pressure to ensure the incompressibility constraint

$$Re\left(\frac{\mathbf{v}^{n+1} - \mathbf{v}^*}{\Delta t}\right) = -\nabla p^{n+1}. \quad (4.8)$$

One of the variants of projection method is named gauge method and discussed in detail in [21, 22]. In which the auxiliary variable

$$\mathbf{a} = \mathbf{u} - \nabla\phi \quad (4.9)$$

is introduced, and (4.6) is formulated as

$$\mathbf{a}_t + (\mathbf{u} \cdot \nabla)\mathbf{u} + \nabla\left(\partial_t\phi - \frac{1}{Re}\Delta\phi + p\right) = \frac{1}{Re}\nabla^2\mathbf{a}. \quad (4.10)$$

So the *gauge variable*  $\phi$  can be defined as

$$\partial_t\phi - \frac{1}{Re}\Delta\phi + p = 0. \quad (4.11)$$

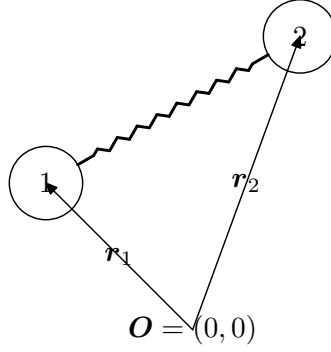
The formulation enables easy assignment of boundary condition and eliminate the numerical boundary layer for pressure update, and we will extend this idea later to solve the viscoelastic flow later.

### 4.1.2 Constitutive law for extra stress

The striking feature of viscoelastic/polymeric materials, compared to viscous fluids, is the manifestation of elastic effect. Since the polymer composition of those materials is responsible for the elastic characteristics, proper model of polymer chains is the key for understanding the relevant physical properties. The simplest molecular scale models for flexible polymers are those elastic dumbbells, which are commonly used in the analysis for rheology of polymeric system. Figure 4.1 shows a typical dumbbell, in which 2 beads with mass  $m$  are connected by a spring and the vector  $\mathbf{Q} = \mathbf{r}_2 - \mathbf{r}_1$  is used to represent the orientation and length of a dumbbell.

If the spring, in a dumbbell is assumed Hookean (Spring force is proportional to de-

Figure 4.1: Dumbbell model



formation,  $\mathbf{F} = H\mathbf{Q}$  with spring constant  $H$ , and spring itself is infinitely extensible.), we call the dumbbell Hookean dumbbell. One can derive macroscopic stress constitutive equation based on careful calculation of ensemble average of Hookean dumbbell dynamics [8, 46], and the bulk stress contribution from elastic dumbbell  $\boldsymbol{\tau}_p$  is written as the constitutive equation

$$\lambda_1 \overset{\nabla}{\boldsymbol{\tau}}_p + \boldsymbol{\tau}_p = 2\eta_p \mathbf{D}, \quad (4.12)$$

where  $\lambda_1$  is relaxation time,  $\eta_p$  is polymer viscosity, the convected time derivative  $\overset{\nabla}{\boldsymbol{\tau}}$  is defined as

$$\overset{\nabla}{\boldsymbol{\tau}} = \frac{\partial \boldsymbol{\tau}}{\partial t} + (\mathbf{v} \cdot \nabla) \boldsymbol{\tau} - (\boldsymbol{\tau} \nabla \mathbf{v} + \nabla \mathbf{v}^T \boldsymbol{\tau}), \quad (4.13)$$

and the rate of strain tensor  $\mathbf{D}$  is

$$\mathbf{D} = \frac{1}{2}(\nabla \mathbf{v} + \nabla \mathbf{v}^T). \quad (4.14)$$

We note  $\boldsymbol{\tau}_p$  defined in (4.12) only account for the polymeric part of contribution to extra stress, and for this Hookean dumbbell model, the viscous component,  $\boldsymbol{\tau}_s$  of equation (4.4), of the extra stress

$$\boldsymbol{\tau} = \boldsymbol{\tau}_s + \boldsymbol{\tau}_p \quad (4.15)$$

should also be included in the momentum equation (without external force)

$$\rho \left( \frac{\partial \mathbf{v}}{\partial t} + (\mathbf{v} \cdot \nabla) \mathbf{v} \right) = -\nabla p + \eta_s \nabla^2 \mathbf{v} + \nabla \cdot \boldsymbol{\tau}_p. \quad (4.16)$$

We also note here (4.15) is named as Oldroyd-B constitutive equation, and by using

$$\overset{\nabla}{\mathbf{I}} = 2\mathbf{D}, \quad (4.17)$$

we can reformulate this constitutive law (4.15) into one equation for  $\boldsymbol{\tau}$

$$\boldsymbol{\tau} + \lambda_1 \overset{\nabla}{\boldsymbol{\tau}} = 2\eta_0(\mathbf{D} + \lambda_2 \overset{\nabla}{\mathbf{D}}), \quad (4.18)$$

where  $\lambda_2$  is named retardation time and  $\eta_0$  is zero shear viscosity.

Obviously we can derive the relationship between the parameter sets,  $(\eta_0, \lambda_2)$  and  $(\eta_s, \eta_p)$ :

$$\eta_s = \frac{\lambda_2}{\lambda_1} \eta_0, \quad \eta_p = (1 - \frac{\lambda_2}{\lambda_1}) \eta_0. \quad (4.19)$$

By assigning special values of time constant, we will have

- i)  $\lambda_2 = 0$ , Upper Convected Maxwell model;
- ii)  $\lambda_2 = \lambda_1$ , viscous case (Naiver-Stokes stress-rate of strain relation).

And we can define  $\beta = \lambda_2/\lambda_1$  to count the weight of viscous and elastic stress contribution. It is also seen that since we would rather not to have negative viscosity, the retardation parameter would be always smaller than relaxation time  $\lambda_2 < \lambda_1$ .

We note here that all the physical parameters in the constitutive equation (4.18) have their physical interpretations[8, 45]:

$$\eta_p = \frac{nk_B T \xi}{4H}, \quad (4.20)$$

where  $n$  is number density of dumbbells,  $\xi = 6\pi\eta_s a$  is friction coefficient for beads of radius  $a$  in dumbbell, and  $H$  is spring constant. Relaxation time is

$$\lambda_1 = \frac{\xi}{4H}, \quad (4.21)$$

and retardation time is

$$\lambda_2 = \frac{\eta_s \xi}{4(\eta_s + \eta_p)H}. \quad (4.22)$$

Now equations (4.3), (4.12), and (4.16) close the equation system for our viscoelastic problems. And the nondimensional parameter groups from those equations are as followed:

- i) Weissenberg number:  $We = \frac{\lambda_1 U}{L}$ , where  $U$  is characteristic speed of flow, and  $L$  is characteristic length of the problem;
- ii) Deborah number:  $De = \frac{\lambda_1}{T_0}$ , where  $T_0$  is characteristic time of flow.

As specified in [7],  $We$  and  $De$  characterize the elastic effect over viscous effect, and the high Weissenberg/Deborah numbers always indicate highly elastic scenario. [4]

The dimensionless version of the system is

$$Re \left\{ \frac{\partial \mathbf{v}}{\partial t} + \mathbf{v} \cdot \nabla \mathbf{v} \right\} = -\nabla p + \beta \nabla^2 \mathbf{v} + \nabla \cdot \boldsymbol{\tau}_p, \quad (4.23a)$$

$$We \left\{ \frac{\partial \boldsymbol{\tau}_p}{\partial t} + (\mathbf{v} \cdot \nabla \boldsymbol{\tau}_p - \nabla \mathbf{v}^T \boldsymbol{\tau}_p - \boldsymbol{\tau}_p \nabla \mathbf{v}) \right\} = (1 - \beta) \mathbf{D} - \boldsymbol{\tau}_p. \quad (4.23b)$$

$$\nabla \cdot \mathbf{v} = 0. \quad (4.23c)$$

Analysis done on (4.23a)-(4.23b) [67, 35] shows that it is mixed type of equations in the system: the convective directive of momentum and constitutive equations give hyperbolicity, and elliptic part is from incompressible constraint, and the diffusion in momentum equation surely indicates parabolic signature. To ensure stability and accuracy, proper treatments on all characteristics are required while devising numerical scheme. And the first thought to everybody is to extend the current numerical schemes successful for viscous case to viscoelastic problems.

### 4.1.3 Current numerical scheme and the difficulty

Previous results on numerical simulation reveal a high Weissenberg number difficulty [35, 67]: iterative methods will lose convergence and accuracy at high Weissenberg number, and the reason is attributed *either to limitations of models or to numerical approximation errors* [67]. Numerical studies have concentrated on deriving stable and accurate methods proper for capturing elastic effect of model system. In literature (survey and summary can be found in [67, 34]) , elastic viscous stress splitting (EVSS)

and its variants (EVSS-G, DEVSS, and DEVSS-G) are proposed by researchers mainly based on finite element (FE) discretization to handle the extra stress properly. Numerical methods (cf. [86, 82], and summary in [67]) based on finite difference (FD) and finite volume (FV) framework are also proposed to solve viscoelastic system.

Since the obvious success on solving Navier-Stokes equation, projection method has been carried over without modification for viscoelastic fluid flow computation. To demonstrate the steps of solving evolution equation, we show the treatment for velocity and extra stress coupling with Van Kan's scheme [36] of using projection technique (cf. [15, 81, 5]): given previous value for  $\mathbf{v}^n$ ,  $\boldsymbol{\tau}_p^n$ , and  $p^n$ , the constitutive equation is used first to update polymeric stress components

$$We \left\{ \frac{\boldsymbol{\tau}_p^{n+1} - \boldsymbol{\tau}_p^n}{\Delta t} + (\mathbf{v} \cdot \nabla \boldsymbol{\tau}_p - \nabla \mathbf{v}^T \boldsymbol{\tau}_p - \boldsymbol{\tau}_p \nabla \mathbf{v})^n \right\} = (1 - \beta) \mathbf{D}^n - \boldsymbol{\tau}_p^n \quad (4.24)$$

$We$  is the Weissenberg number. And then an auxiliary velocity variable  $\mathbf{v}^*$  is calculated from momentum equation by neglecting pressure

$$Re \left\{ \frac{\mathbf{v}^* - \mathbf{v}^n}{\Delta t} + \mathbf{v}^n \cdot \nabla \mathbf{v}^n \right\} = \beta \nabla^2 \mathbf{v}^* + \nabla \cdot \boldsymbol{\tau}_p^n. \quad (4.25)$$

To ensure the incompressibility constraint, the auxiliary velocity field is projected to the divergence free function space

$$\begin{aligned} \frac{\mathbf{v}^{n+1} - \mathbf{v}^*}{\Delta t} &= -\nabla p^{n+1} \\ \nabla \cdot \mathbf{v}^{n+1} &= 0, \end{aligned} \quad (4.26)$$

and pressure field  $p$  is updated to new time level during the above update of velocity.

Based on the way of handling the constitutive (4.24) and momentum (4.25) equations, different methods we mentioned at the beginning of this subsection can be formulated. To reveal the source of error in numerical procedure, we will discuss details of the system and then we will propose our new treatment in the following.



## 4.2 Extension of the projection method for viscoelastic fluid flows

The governing equations for the viscoelastic model, can be rearranged into a system, we will write the system in quasilinear form to show the characteristics of hyperbolic and elliptic/parabolic part. We also identify the limit of stress components for type change in the system. We first present the system in hyperbolic form and then try to maintain the incompressibility with modified gauge method presented.

### 4.2.1 System of model equations

We define field variable  $\mathbf{q}$  for velocity and stress components as

$$\mathbf{q} = (v_x, v_y, \tau_{xx}, \tau_{xy}, \tau_{yy})^T. \quad (4.27)$$

And the system of (4.3), (4.12), and (4.16) can be reformulated into hyperbolic form, by putting the continuity equation (4.3) aside for a moment,

$$\frac{\partial \mathbf{q}}{\partial t} + \mathbf{A} \frac{\partial \mathbf{q}}{\partial x} + \mathbf{B} \frac{\partial \mathbf{q}}{\partial y} = \mathbf{C} \left( \frac{\partial^2 \mathbf{q}}{\partial x^2} + \frac{\partial^2 \mathbf{q}}{\partial y^2} \right) + \boldsymbol{\psi}(\mathbf{q}) + \boldsymbol{\phi}, \quad (4.28)$$

with

$$\mathbf{A} = \begin{pmatrix} v_x & 0 & -1/\rho & 0 & 0 \\ 0 & v_x & 0 & -1/\rho & 0 \\ -2(\tau_{xx} + \eta_p/\lambda) & 0 & v_x & 0 & 0 \\ 0 & -(\tau_{xx} + \eta_p/\lambda) & 0 & v_x & 0 \\ 0 & -2\tau_{xy} & 0 & 0 & u \end{pmatrix}, \quad (4.29a)$$

$$\mathbf{B} = \begin{pmatrix} v_y & 0 & 0 & -1/\rho & 0 \\ 0 & v_y & 0 & 0 & -1/\rho \\ -2\tau_{xy} & 0 & v_y & 0 & 0 \\ -(\tau_{yy} + \eta_p/\lambda) & 0 & 0 & v_y & 0 \\ 0 & -2(\tau_{yy} + \eta_p/\lambda) & 0 & 0 & v_y \end{pmatrix}, \quad (4.29b)$$

and terms of right hand side

$$\mathbf{C} = \begin{pmatrix} \frac{\eta_s}{\rho} & 0 & 0 & 0 & 0 \\ 0 & \frac{\eta_s}{\rho} & 0 & 0 & 0 \\ 0 & 0 & 0 & 0 & 0 \\ 0 & 0 & 0 & 0 & 0 \\ 0 & 0 & 0 & 0 & 0 \end{pmatrix}, \quad (4.29c)$$

$$\boldsymbol{\phi} = \left(-\frac{1}{\rho} \frac{\partial p}{\partial x}, -\frac{1}{\rho} \frac{\partial p}{\partial y}, 0, 0, 0\right)^T. \quad (4.29d)$$

and

$$\boldsymbol{\psi}(\mathbf{q}) = \begin{pmatrix} \frac{\eta_s}{\rho} \nabla^2 u - \frac{1}{\rho} \frac{\partial p}{\partial x} \\ \frac{\eta_s}{\rho} \nabla^2 v - \frac{1}{\rho} \frac{\partial p}{\partial y} \\ -\frac{1}{\lambda} \tau_{xx} \\ -\frac{1}{\lambda} \tau_{xy} \\ -\frac{1}{\lambda} \tau_{yy} \end{pmatrix} \quad (4.29e)$$

The eigensystem of coefficient matrix  $\mathbf{A}$  and  $\mathbf{B}$  are explicitly determined, and we give them as followed. Eigenvalues of matrix  $\mathbf{A}$  are  $\gamma_{\mp}^{\mathbf{A}} = v_x \mp \sqrt{(\eta_p/\lambda + \tau_{xx})/\rho}$ , and we have the corresponding eigenvectors  $\boldsymbol{\xi}_{\mp}^{\mathbf{A}}$

$$\boldsymbol{\xi}_{\mp}^{\mathbf{A}} = (0, \pm \sqrt{\rho(\frac{\eta_p}{\lambda} + \tau_{xx})}, 0, \rho(\frac{\eta_p}{\lambda} + \tau_{xx}), 2\rho\tau_{xy})^T. \quad (4.30)$$

For eigenvalue  $\gamma^{\mathbf{A}} = v_x$ , the corresponding eigenvector is

$$\boldsymbol{\xi}^{\mathbf{A}} = (0, 0, 0, 0, 1)^T. \quad (4.31)$$

And eigenvalues  $\xi_{\mp}^{\mathbf{A}} = v_x \mp \sqrt{2\rho(\eta_p/\lambda + \tau_{xx})}$  have eigenvectors

$$\boldsymbol{\chi}_{\mp}^{\mathbf{A}} = (\pm 1, 0, \sqrt{2\rho(\eta_p/\lambda + \tau_{xx})}, 0, 0)^T. \quad (4.32)$$

The eigenvalues of matrix  $\mathbf{B}$   $\gamma_{\mp}^B = v_y \mp \sqrt{(\eta_p/\lambda + \tau_{yy})/\rho}$  have corresponding eigenvectors

$$\boldsymbol{\xi}_{\mp}^B = (\pm \sqrt{\rho(\frac{\eta_p}{\lambda} + \tau_{xx})}, 0, 2\rho\tau_{xy}, \rho(\frac{\eta_p}{\lambda} + \tau_{xx}), 0)^T. \quad (4.33)$$

$\gamma^B = v_y$  has eigenvector

$$\boldsymbol{\xi}^A = (0, 0, 1, 0, 0)^T. \quad (4.34)$$

And eigenvalues  $\xi_{\mp}^B = v_y \mp \sqrt{2\rho(\eta_p/\lambda + \tau_{yy})}$  have eigenvectors

$$\boldsymbol{\chi}_{\mp}^B = (0, \pm 1, 0, 0, \sqrt{2\rho(\eta_p/\lambda + \tau_{yy})})^T. \quad (4.35)$$

From the eigenvalues and eigenvectors, we see the system (4.28) is hyperbolic as long as the condition

$$\frac{\eta_p}{\lambda} > \tau_{xx}, \text{ and } \frac{\eta_p}{\lambda} > \tau_{yy}. \quad (4.36)$$

As proved in [35], the hyperbolicity condition is always satisfied for Oldroyd-B model with  $\eta_s > 0$ , and we then have to maintain this property in our numerical procedure.

As mentioned in [82], to keep the incompressibility constraint valid, the longitudinal wave should not be propagating in the system. This fact is critical for devising stable and accurate numerical scheme. As suggested by [82], the natural choice is to modify the projection method for the Navier-Stokes equation to incorporate the elastic stress of the system and render the algorithm suitable for viscoelastic fluid flow. We will introduce our attempt of modification in the following.

### 4.2.2 Gauge formulation

Our investigation of modification on the projection method to solve viscoelastic system starts with the gauge formulation [21, 22]. We try to manipulate the original gauge variable of the method to obtain a suitable numerical scheme for our purpose. As suggested by the formulation of (4.16), the divergence of extra stress affects the momentum equation as an elastic source. Then our original emphasis on modification of the gauge formulation is to include the history of stress divergence into the auxiliary variable, so we can combine the computation of velocity and the divergence of stress

to introduce the dimensional auxiliary variable  $\mathbf{a}$ ,

$$\mathbf{a} = \mathbf{v} + \nabla\phi - \frac{1}{\rho} \int_0^t \nabla \cdot \boldsymbol{\tau}_p ds. \quad (4.37)$$

Then the equation of (4.16) can be rewritten as

$$\frac{\partial \mathbf{a}}{\partial t} + (\mathbf{v} \cdot \nabla) \mathbf{v} = \frac{\eta_s}{\rho} \nabla^2 \mathbf{a} + \frac{\eta_s}{\rho} \nabla^2 \frac{1}{\rho} \int_0^t \nabla \cdot \boldsymbol{\tau}_p ds \quad (4.38a)$$

$$\nabla \cdot \mathbf{a} = \nabla^2 \phi - \frac{1}{\rho} \nabla \cdot \int_0^t \nabla \cdot \boldsymbol{\tau}_p ds \quad (4.38b)$$

$$\frac{\partial \phi}{\partial t} - \frac{\eta_s}{\rho} \nabla^2 \phi = \frac{1}{\rho} p \quad (4.38c)$$

where  $\phi$  is called *gauge variable*. System of equations (4.38a)–(4.38c) and (4.12) now is in gauge formulation.

The whole idea of modifying the projection procedure is to count for the effect of elastic stress to velocity field. Now we use the above gauge representation of the system to obtain the projection steps. For simplicity, we first choose a local impact of the extra stress on the auxiliary of velocity, so as defined in previous section, we give the variable (from here, we use  $\tau$  to denote  $\tau_p$  for simplicity)

$$\mathbf{a} = \mathbf{v} + \nabla\phi - \frac{1}{\rho} \int_{t_n}^t \nabla \cdot \boldsymbol{\tau}(s) ds \triangleq \mathbf{v} + \mathbf{r} \quad (4.39)$$

and the gauge variable

$$\frac{\partial}{\partial t} \phi = \frac{1}{\rho} (p + \eta_s \nabla^2 \phi). \quad (4.40)$$

So originally defined field variables (cell centered) include auxiliary variable  $\mathbf{a} = (a_x, a_y)$ , stress tensor  $\boldsymbol{\tau} = (\tau_{xx}, \tau_{xy}, \tau_{yy})$ , velocity  $\mathbf{v} = (u, v)$ , gauge variable  $\phi$ , and pressure  $p$ . New time level value of velocity and pressure are updated from auxiliary and gauge variables.

Given all the values at previous step, which means all cell centered and edge centered variables are up to date and for the initial setup the auxiliary velocity at edge have to satisfy the divergence free condition, we intend to calculate the update for next step as

followed

1. We need to construct the hyperbolic formula to take care of auxiliary velocity  $\mathbf{a}$  and the extra stress  $\boldsymbol{\tau}$  at the same time.

$$\begin{aligned}\mathbf{a}_t + (\mathbf{v} \cdot \nabla) \mathbf{v} &= 0 \\ \boldsymbol{\tau}_t + (\mathbf{v} \cdot \nabla) \boldsymbol{\tau} &= \boldsymbol{\tau}(\nabla \mathbf{v}) + (\nabla \mathbf{v})^T \boldsymbol{\tau} - \frac{1}{\lambda} \boldsymbol{\tau} + \frac{2\eta_p}{\lambda} \mathbf{D}\end{aligned}\tag{4.41}$$

while we notice our velocity gradient defined as

$$\nabla \mathbf{v} = \begin{pmatrix} \frac{\partial u}{\partial x} & \frac{\partial v}{\partial x} \\ \frac{\partial u}{\partial y} & \frac{\partial v}{\partial y} \end{pmatrix}\tag{4.42}$$

With the help of  $\mathbf{v} = \mathbf{a} - \mathbf{r}$ , we would have

$$\begin{aligned}\mathbf{a}_t + (\mathbf{v} \cdot \nabla) \mathbf{a} &= ((\mathbf{a} - \mathbf{r}) \cdot \nabla) \mathbf{r} \\ \boldsymbol{\tau}_t + (\mathbf{v} \cdot \nabla) \boldsymbol{\tau} &= \boldsymbol{\tau}(\nabla \mathbf{v}) + (\nabla \mathbf{v})^T \boldsymbol{\tau} - \frac{1}{\lambda} \boldsymbol{\tau} + \frac{2\eta_p}{\lambda} \mathbf{D}\end{aligned}\tag{4.43}$$

We notice the source term in the above hyperbolic equation involves the field variable itself, but they could be specified after the wave propagation is applied by the source term splitting result. Furthermore the advection velocity is edge centered to capture the correct physics flux. And the velocity  $\mathbf{v}$  should be cell centered, since it acts as the source term for the equation.

2. The extra stress is updated here to include the diffusion effect and it should be before the momentum equation time splitting, but for the first round of test we ignore this part and take the auxiliary extra stress obtained in the first step as the one we would have for the next time level.
3. Crank-Nicolson step is utilized to get the approximate velocity via momentum equation (cell centered) and in this step, we have to take care of the modification of auxiliary velocity variable and the extra stress (cell center). If  $\mathbf{f}(t) \triangleq \int_{t_n}^t \nabla \cdot \boldsymbol{\tau} ds / \rho$ , we have

$$\frac{\mathbf{a}^{n+1} - \mathbf{a}^*}{\Delta t} = \frac{1}{2} \frac{\eta_s}{\rho} (\nabla^2 (\mathbf{a}^{n+1} + \mathbf{a}^*) + \nabla^2 (f^{n+1} + f^*))\tag{4.44}$$

4. Gauge projection is applied and then the gauge update for gauge variable and pressure is calculated. So velocity is updated and the extra stress is updated to the new level.

$$\nabla^2 \phi = \nabla \cdot \mathbf{a} + \frac{1}{\rho} \nabla \cdot \int_{t_n}^t \nabla \cdot \boldsymbol{\tau}(s) ds \quad (4.45)$$

5. Then the edge centered velocity is interpolated from the intermediate velocity calculated from the above steps to make sure the edge velocity divergence free.

Boundary conditions are not clear. If we set all the derivative of stress component  $\boldsymbol{\tau}$  zero on the boundary, then we would have the similar boundary condition for  $\mathbf{a}$  as in the Navier-Stokes case:

$$\mathbf{a} \cdot \mathbf{n}_n = \mathbf{v}_B \cdot \mathbf{n}_n, \quad \mathbf{a} \cdot \mathbf{n}_\tau = \frac{\partial \phi}{\partial \mathbf{n}_\tau} + \mathbf{v}_B \cdot \mathbf{n}_\tau, \quad (4.46)$$

Before every computation step, boundary condition for  $\mathbf{a}$  and  $\boldsymbol{\tau}$  have to be imposed. The boundary conditions of  $\mathbf{v}$  are naturally chosen and they will have impact on the boundary condition of  $\mathbf{a}$  by equation (4.37).

We also notice the right hand side of equation (4.45) includes divergence of  $\mathbf{a}$ , which tells us the need of boundary condition update of it. Also we know

$$\nabla \cdot (\nabla \cdot \boldsymbol{\tau}) = \frac{\partial^2 \tau_{xx}}{\partial x^2} + 2 \frac{\partial^2 \tau_{xy}}{\partial x \partial y} + \frac{\partial^2 \tau_{yy}}{\partial y^2}, \quad (4.47)$$

so the ghost value of stress components are also needed in computation.

The algorithm shows obvious elastic flow pattern in driven cavity compared to viscous result and results are showed in Figure 4.2 and 4.3. And for small Deborah number calculation, the computation converge to steady state, but it can not achieve convergent results for highly elastic fluid flow.

Figure 4.2: Simulation of cavity for Oldroyd-B model. Note the solid wall boundary conditions are assigned to all walls, and the top wall is moving to the right with velocity 1. Red solid lines are streamline with  $Re = 100$ ,  $We = 0.1$ , and time step  $\Delta t = 0.01$ . Green dash line is the stream line of viscous flow with same Reynolds number. Top plot show the comparison after 10 step computations of Oldroyd-B flow; and bottom plot show the comparison after 20 steps.

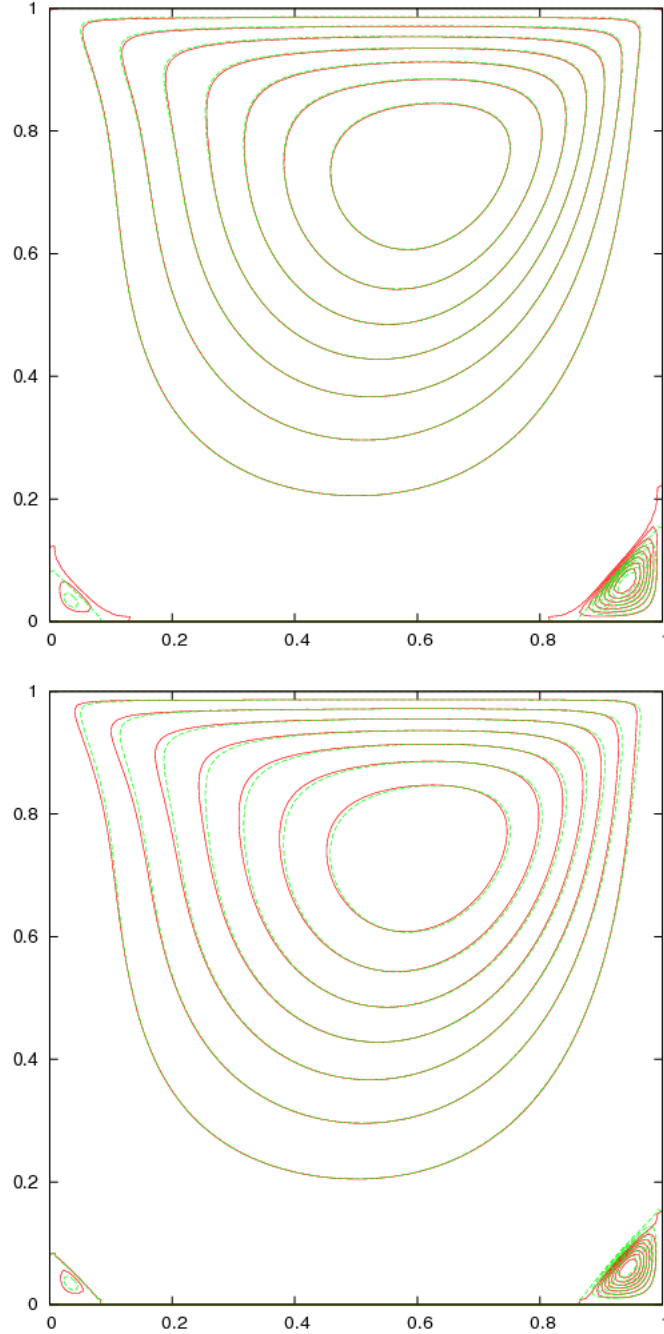
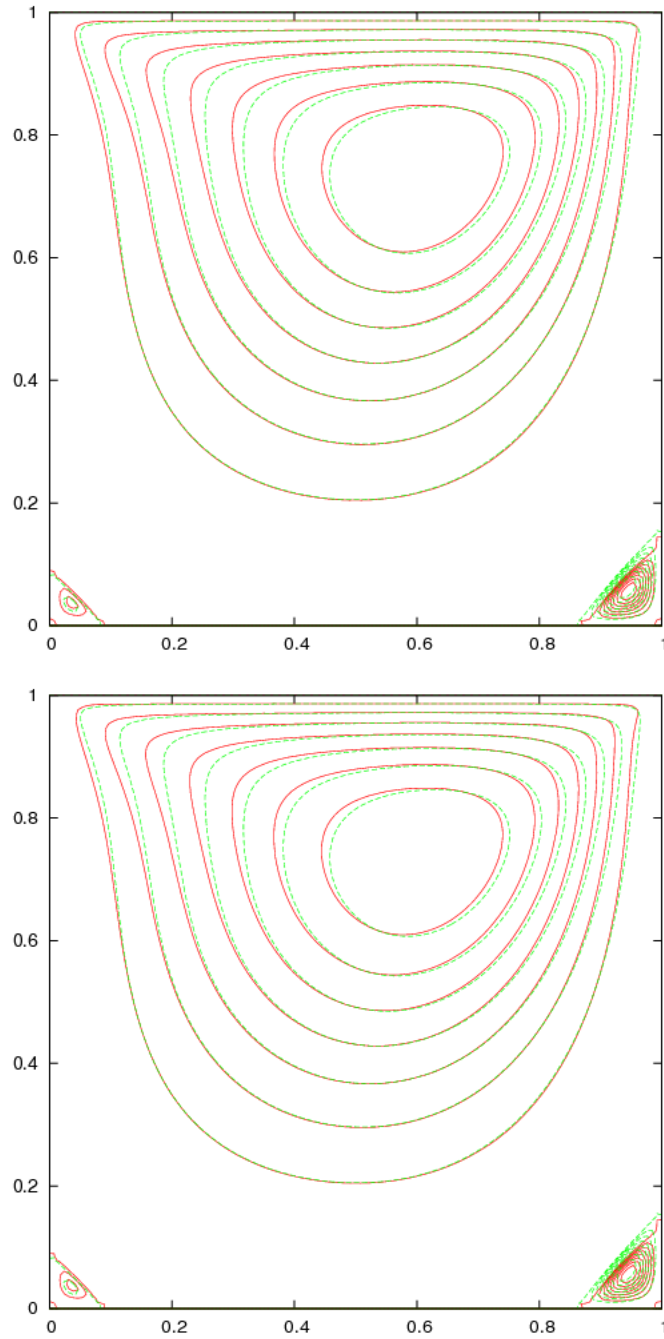


Figure 4.3: Simulation of cavity problem with Oldroyd-B constitutive law. Note the solid wall boundary conditions are assigned to all walls, and the top wall is moving to the right with velocity 1. Red solid lines are streamline with  $Re = 100$ ,  $We = 0.1$ , and time step  $\Delta t = 0.01$ . Green dash line is the stream line of viscous flow with same Reynolds number. Top plot show the comparison after 50 step computations of Oldroyd-B flow; and bottom plot show the comparison after 60 steps.





### 4.3 Analysis on extra stress and the new numerical scheme

To verify the validity of a numerical scheme, we need to check whether main physical feature is captured properly in the computation and results. From the analysis of 1d shear wave model of last chapter, we know there should be elastic shear waves propagating in the system so correct numerical schemes should capture this phenomena.

The analysis on the shear wave inspires us in considering the linearized version (neglect all source terms and convective terms) of (4.28). After the linearization, we end up with

$$\begin{cases} \nabla \cdot \mathbf{v} = 0 \\ \rho \frac{\partial \mathbf{v}}{\partial t} = -\nabla p + \nabla \cdot \boldsymbol{\tau} , \\ \frac{\partial \boldsymbol{\tau}}{\partial t} = \frac{\eta_p}{\lambda} \mathbf{D} \end{cases} \quad (4.48)$$

which leads to a wave equation of  $\mathbf{v}$  in 2 dimensional computational domain.

As to the gauge formulation of above section, we see the shear generating part, which is divergence of stress tensor, is included in the auxiliary variable and does not affect the momentum transport directly, so it fails to do so since the elastic waves are not retained in the computation.

From the above argument, we can see when we look into the feature of propagation of elastic wave in Oldroyd-B material, one fundamental question for a numerical scheme is whether it can capture the wave propagation correctly. By analyzing (4.48), we have

$$\begin{aligned} \rho \frac{\partial^2 \mathbf{v}}{\partial t^2} &= -\nabla \left( \frac{\partial p}{\partial t} \right) + \frac{\eta_p}{\lambda} (\nabla^2 \mathbf{v} + \nabla (\nabla \cdot \mathbf{v})) \\ &= -\nabla \dot{p} + c_t^2 \nabla^2 \mathbf{v} + (c_l^2 - c_t^2) \nabla (\nabla \cdot \mathbf{v}), \end{aligned} \quad (4.49)$$

where  $c_t$  is transverse wave speed and  $c_l$  is longitudinal wave speed. It is clear now, from basic elasticity theory [44], we know there are indeed two elastic waves found: transverse waves will not change volume of material and longitudinal wave makes volume change with wave propagations. So we try to identify the components, which generate shear waves, in stress, and we also want to keep track of the stress elements that violate the incompressibility condition so we can avoid the violation during computa-

tion. The force-carrying part that remains is the one of interest. The key aspect of the method of Double-Projection proposed [61] is to now extract from this force-carrying part the elastic displacement. Then the elastic displacement is corrected to eliminate longitudinal modes. So the questions raised here:

1. can the stress be divided into two parts nicely (or could we find the function space); and
2. is the projection step enough to enforce the incompressibility constraint and to ensure the extra stress evolution.

And we will answer those questions in the following.

### 4.3.1 Stress tensor decomposition

Based on the observations to the system, we are trying to identify the source of error in numerical algorithm. Due to the analysis on property of elasticity as above, the first thing we notice is that clearly any time discretization of numerical procedure which introduces spurious modes will cause numerical instability, hence should be taken care of. From this point of view, Mitran proposes the idea of devising numerical procedure to eliminate those modes and point out [61] the main concern is on the procedure of elastic stress update in the numerical computation. The divergence-free part does not affect the momentum equation and hence can be neglected.

The idea of elastic waves isolation depends on how well we can decompose extra stress tensor and grab the force generating part of it. And we learned from previous literature that it is possible to split a symmetric tensor into two parts. We note here that there may be multiple choices for the decomposition of extra stress tensor, and our first intuition is to isolate the divergence free part and the remainder. From the references we found [83, 65], we have the following theorem :

**Theorem 1 (Symmetric Tensor Decomposition)** *Suppose the domain  $\Omega \in \mathcal{R}^3$  and the boundary of  $\Omega$  is defined by  $\partial\Omega$ . The outward unit normal vector on  $\partial\Omega$  is denoted by  $\mathbf{n}$ . We take  $\partial_T\Omega$  and  $\partial_u\Omega$  as supplementary subsets of  $\partial\Omega$ . Given symmet-*

ric tensor  $\mathbf{S}$  in  $C^1(\Omega)$ ,  $\mathbf{S}$  could be uniquely decomposed into

$$\mathbf{S} = \mathbf{T} + \mathbf{E} \quad (4.50)$$

where  $\mathbf{T}$  and  $\mathbf{E}$  are symmetric tensor field on  $\Omega$  and they satisfy, respectively,

$$\nabla \cdot \mathbf{T} = 0, \quad \mathbf{T} \cdot \mathbf{n}|_{\partial_T \Omega} = 0 \quad (4.51a)$$

$$\mathbf{E} = \frac{1}{2}(\nabla \mathbf{u} + \nabla \mathbf{u}^T), \quad \mathbf{u}|_{\partial_u \Omega} = 0 \quad (4.51b)$$

where the introduced filed variable  $\mathbf{u} = (u_x, u_y)$  representing deformation could be determined by

$$\nabla^2 \mathbf{u} + \nabla(\nabla \cdot \mathbf{u}) = 2\nabla \cdot \mathbf{S} \quad (4.52a)$$

with boundary conditions

$$\frac{1}{2}(\nabla \mathbf{u} + \nabla \mathbf{u}^T) \cdot \mathbf{n}|_{\partial_T \Omega} = -\mathbf{S} \cdot \mathbf{n}, \quad \mathbf{u}|_{\partial_u \Omega} = 0 \quad (4.52b)$$

Taking the theorem, we can find the deformation equation that determines the longitudinal wave part of extra stress tensor is actually the equilibrium state equation of body force with Poisson ratio taken as zero. So now the fact we are facing is if we want to decouple the extra stress  $\boldsymbol{\tau}$ , we will have to use the divergence of extra stress tensor as the effective body force to calculate the equilibrium deformation and then we will have the two parts of the tensor. Based on our observations here, Mitran leads us to a numerical scheme that suppress introduction of spurious modes in discretization and is introduced in the following [61].

### 4.3.2 Numerical scheme based on the stress decomposition

So we propose double projection method to eliminate spurious wave propagating in the hyperbolic system and keep incompressibility condition satisfied. Given all variables at previous time level,  $\mathbf{v}^n$ ,  $p^n$ , and  $\boldsymbol{\tau}^n$ , the first step is to get auxiliary polymeric stress  $\boldsymbol{\tau}^*$

$$We\left(\frac{\boldsymbol{\tau}^* - \boldsymbol{\tau}^n}{\Delta t}\right) = (1 - \beta)2\mathbf{D}^n - \boldsymbol{\tau}^n - We((\mathbf{v} \cdot \nabla)\boldsymbol{\tau} - \boldsymbol{\tau}\nabla\mathbf{v} - (\nabla\mathbf{v})^T\boldsymbol{\tau})^n. \quad (4.53)$$

And by applying theorem of last subsection, we decompose the auxiliary stress into shear generating part and divergence free part  $\boldsymbol{\tau}^* = \boldsymbol{\alpha} + \boldsymbol{\beta}^*$ , where  $\boldsymbol{\beta}^*$  satisfies

$$\boldsymbol{\beta}^* = \frac{1}{2}(\nabla\mathbf{u}^* + (\nabla\mathbf{u}^*)^T), \quad (4.54)$$

and can be treated as the stress field induced by microscopic dumbbell spring deformation  $\mathbf{u}$ , and filed variable  $\mathbf{u}^*$  is determined by

$$\nabla^2\mathbf{u} + \nabla(\nabla \cdot \mathbf{u}) = 2\nabla \cdot \boldsymbol{\tau}^*, \text{ with } \mathbf{u}|_{\partial\Omega} = 0. \quad (4.55)$$

So we can update the deformation variable  $\mathbf{u}^*$  into divergence free space by first projection

$$\nabla^2\phi = -\nabla \cdot \mathbf{u}^*, \quad (4.56a)$$

and then

$$\mathbf{u}^{n+1} = \mathbf{u}^* + \nabla\phi. \quad (4.56b)$$

And finally the force carrying part of the stress tensor should be updated as

$$\boldsymbol{\tau}^{n+1} = \frac{1}{2}(\nabla\mathbf{u}^{n+1} + (\nabla\mathbf{u}^{n+1})^T) \quad (4.56c)$$

Now we are ready for the velocity update

$$Re\left(\frac{\mathbf{v}^* - \mathbf{v}^n}{\Delta t}\right) = \beta \nabla^2 \mathbf{v} - Re(\mathbf{v}^n \cdot \nabla) \mathbf{v}^n + \nabla \cdot \boldsymbol{\tau}^{n+1}. \quad (4.57)$$

And pressure is computed by

$$\nabla^2 p = \frac{Re}{\Delta t} \nabla \cdot \mathbf{v}^*, \quad (4.58)$$

and finally velocity is updated to the divergence free space

$$\mathbf{v}^{n+1} = \mathbf{v}^* - \frac{\Delta t}{Re} \nabla p^{n+1}. \quad (4.59)$$

The merit of this algorithm is explicit update for polymeric stress with respect to deformation field, which helps to maintain the incompressibility constraint and eliminate the violation caused by extra stress for every time step. Essentially, the longitudinal part of wave generated by numerical discretization is removed by this explicit treatment and we expect much more stable and accurate numerical results based on this algorithm.

And this analysis also sheds lights on further development of numerical scheme: the ones that do not generate spurious modes should be considered.

### 4.3.3 Analysis on the FENE-P model

The Hookean dumbbell gives explicit formula for bulk constitutive equation, but its drawback is obvious: in physical reality, the polymer chain can not be extended beyond its own length; and we can expect the force generated by spring will be greatly larger when polymer chain is in extended state. Hence the Hookean force law  $\mathbf{F} = H\mathbf{Q}$  is not appropriate and a nonlinear force is proposed (cf. [8])

$$\mathbf{F} = \frac{H\mathbf{Q}}{1 - (\langle Q \rangle / Q_0)^2} \quad Q < Q_0, \quad (4.60)$$

where  $Q_0$  is the maximum extension length of dumbbell polymer. This is called finitely extensible nonlinear elastic (FENE) spring force and the corresponding dumbbell is named FENE dumbbell. Due to the nonlinearity of spring force, the closed-form en-

semble average of force in calculation of stress can not be obtained, and the derivation of constitutive equation for FENE dumbbells then requires an approximation. The popular approximation due to Peterlin [8, 34] leads to the resulting constitutive law (FENE-P), formulated as

$$\boldsymbol{\tau} = \nu k_B T \lambda_H \overset{\nabla}{\boldsymbol{\alpha}}, \quad (4.61a)$$

where  $\nu$  is the number density of dumbbells and the *structural tensor*  $\boldsymbol{\alpha}$  [8]

$$\boldsymbol{\alpha} = H \frac{\langle \mathbf{Q}\mathbf{Q} \rangle}{k_B T}, \quad (4.61b)$$

is determined by

$$\frac{\boldsymbol{\alpha}}{1 - \frac{\text{tr}(\boldsymbol{\alpha})}{b}} + \lambda_H \overset{\nabla}{\boldsymbol{\alpha}} = \frac{b}{b+2} \mathbf{I}, \quad (4.61c)$$

where  $b = H Q_0^2 / k_B T$  and  $\text{tr}$  represents the trace operator for second order tensor.

From the formulation of constitutive equation of FENE-P, the stress tensor should have nonlinear dependence on gradient of deformation  $\mathbf{u}$  instead of just linear proportionality. To treat FENE-P model in a similar framework as we did for Hookean dumbbells, we want to expand the stress tensor linearly with respect to small physical parameter and apply the tool we already have. In [3], dimensionless parameter  $b$  is treated as *the ratio of squared end-to-end distance of chain to its equilibrium value*, so  $1/b$  is usually small number. Also, as showed in [3], the expansion of stress tensor  $\boldsymbol{\tau}$  with respect to  $1/b$  is presented,

$$\boldsymbol{\tau} = \boldsymbol{\tau}_0 + \frac{1}{b} \boldsymbol{\tau}_1 + \frac{1}{b^2} \boldsymbol{\tau}_2 + \cdots, \quad (4.62)$$

which makes a natural candidate for our purpose.

Actually, in [3], the expansion of structural tensor  $\boldsymbol{\alpha}$

$$\boldsymbol{\alpha} = \boldsymbol{\alpha}_0 + \frac{1}{b} \boldsymbol{\alpha}_1 + \frac{1}{b^2} \boldsymbol{\alpha}_2 + \cdots, \quad (4.63)$$

leads the expansion in (4.62).

From those expansions and the constitutive equations, in [3], explicit equations for

$\alpha_0$  and  $\alpha_1$  are given

$$\alpha_0 + \lambda_H \overset{\nabla}{\alpha}_0 = \mathbf{I}; \quad (4.64)$$

and

$$\alpha_1 + \lambda_H \overset{\nabla}{\alpha}_1 = \beta_0, \quad (4.65)$$

where

$$\beta_0 = (\text{tr}(\alpha_0))\alpha_0 + 2\alpha_0^2. \quad (4.66)$$

And the differential equations for  $\tau_0$  and  $\tau_1$  are also given

$$\tau_0 = \nu k_B T (\mathbf{I} - \alpha_0), \quad (4.67)$$

and

$$\tau_1 = -\nu k_B T (\alpha_1 + \beta_0). \quad (4.68)$$

If we plug  $\tau_0$  of (4.67) into equation for  $\alpha_0$  of (4.64), we clearly see  $\tau_0$  is actually the Hookean dumbbell stress and satisfies the Oldroyd-B constitutive law:

$$\lambda_H \overset{\nabla}{\tau}_0 + \tau_0 = \lambda_H \nu k_B T \mathbf{D}. \quad (4.69)$$

So higher order terms in (4.62) describe deviation of FENE-P stress tensor from Hookean dumbbell, and the leading order of structural tensor  $\alpha$  is the corresponding deformation field for Hookean dumbbell. After we rewrite the differential equation for  $\tau_1$

$$\tau_1 + \lambda_H \overset{\nabla}{\tau}_1 = \lambda_H (\nu k_B T) \overset{\nabla}{\beta}_0, \quad (4.70)$$

we see the only difference of (4.69) and (4.70) is in the right hand side, which can be seen as the source term of the stress, of the equations. And we also see the nonlinearity of stress tensor on the structure tensor is carried on by the source term of their equations.

When we devise a numerical scheme for FENE-P dumbbell model, we can take the expansion and truncate with finite terms (take two here,  $\tau = \tau_0 + \tau_1/b$ ). And then the numerical approximation scheme are proposed with minus modification from the one we have in section 4.3.2 for Hookean dumbbell.

So given previous step values for  $\mathbf{v}^n$ ,  $p$ , and  $\boldsymbol{\tau}^n = \boldsymbol{\tau}_0 + \boldsymbol{\tau}_1$ , we can advance  $\boldsymbol{\tau}_0^*$  by (4.69), and the corresponding deformation field can be obtained by solving (4.55) and the force carrying part of the stress is  $\boldsymbol{\tau}_0^{n+1} = \nabla \mathbf{u}_0^{n+1} + (\nabla \mathbf{u}_0^{n+1})^T$ .

To include higher order term  $\boldsymbol{\tau}_1$  of (4.62) from FENE-P stress, we should calculate the force carrying part with our decomposition technique applied again for  $\boldsymbol{\tau}_1$ . Also, note from  $\boldsymbol{\tau}_0^{n+1}$ , we can determine  $\boldsymbol{\alpha}_0$  by (4.67)

$$\boldsymbol{\alpha}_0^{n+1} = \mathbf{I} - \frac{1}{\nu k_B T} \boldsymbol{\tau}_0^{n+1}, \quad (4.71)$$

and then  $\boldsymbol{\beta}_0^{n+1}$  is up to date.

The  $\boldsymbol{\tau}_1^*$  can be advanced by (4.70), and the corresponding deformation field  $\mathbf{u}_1^{n+1}$  is obtained again by solving (4.55) with stress term of  $\boldsymbol{\tau}_1$ . And finally  $\boldsymbol{\tau}_1^{n+1} = \nabla \mathbf{u}_1^{n+1} + (\nabla \mathbf{u}_1^{n+1})^T$  is calculated. And the approximation  $\boldsymbol{\tau}^{n+1} = \boldsymbol{\tau}_0^{n+1} + \boldsymbol{\tau}_1^{n+1}/b$  is proceeded and plugged into (4.57) for velocity update. And the rest of the numerical scheme is again projection of velocity to divergence free space as what we have in 4.3.2 after (4.57).

We note the approximation to the nonlinear stress (4.62) could be carried on in this way of expansion, but we expect dramatically increase of computation work. We suspect it will be enough for most application to include just the first order correction of stress, and we will verify our conjecture in future work.



# Chapter 5

## Conclusions

In this dissertation, we first study the diffusive transport for micron-scale particles in viscoelastic fluids. A time-domain statistical framework is presented for two purposes: as an inversion toolkit for recovery of the diffusive transport modulus in a generalized Langevin equation from experimental time series of tracer positions; and, as a direct simulation toolkit for pathogen diffusion of single particles and statistical correlations. These direct and inverse algorithms combine into a general package for anomalous diffusive transport of pathogens in soft matter, which we anticipate to be complementary to the Mason-Weitz experimental and theoretical protocol [58, 57, 56]. These tools are presently being applied to characterization of pulmonary liquids and DNA solutions with our colleagues Superfine, Hill, and Cribb in the Virtual Lung Project at UNC.

An open question relates to the range of power law behavior that is possible for GLE models with the class of  $N$ -mode exponential kernels is considered in this work. So far, we have reproduced the classical Rouse and Zimm MSD scalings on intermediate timescales between the shortest and longest relaxation times for kernels with the Rouse and Zimm relaxation spectra. However, there are limited theoretical results for general exponential series kernels. Our preliminary numerical studies show a wide range of power law behavior is possible as the relaxation spectrum and the respective weights for each mode are varied.

These tools are viewed as a foundation for further extensions of the single-bead and two-bead models and experiments [16, 50]. The ability to separate local bead-fluid interactions from the bulk viscoelastic modulus, and to identify heterogeneity from single particle and two-particle statistical correlations, are key future applications of

these tools.

Also, we notice the fluctuation dissipation theorem for the GLE with time dependent external force applied is presented in [10]. When this modified F-D theory is combined with our statistical tools here, we will be able to model the microscopic diffusive transport coupled with time dependent chemical interactions, which will be a promising application to biological systems.

In the discussion of chapter 3, we have extended the Ferry shear wave analysis to include finite depth within linear viscoelasticity, and then to include nonlinearity with constitutive laws of Maxwell type, for purposes of inverse characterization experiments in low volume samples of biological fluids. The linear models are exactly solvable with the Fourier method, allowing for an explicit formula for the inverse characterization of a known viscoelastic material due solely to finite depth effects. At frequencies and bulk strains typical for conditions encountered by the airway surface liquid in the lung, errors in the recovery of storage and loss moduli are enormous when fitted to inappropriate theoretical models[60]. If the fluid behaves nonlinearly as controlled bulk strain from the driven plate is ramped up, either due to convective nonlinearity or shear thinning, we present the system of model equations and numerical method that solves them with high order of accuracy to make predictions. The boundary analysis for the resulting hyperbolic system sheds lights in numerical simulation of more general cases ( $2d$ ,  $3d$ , and unsteady), and we also notice that the application of asymmetric lower plate boundary condition predicts net transport with proper upper plate stress boundary conditions, which will be useful for future study of lung mucus clearance.

These modeling tools have been developed in context with a new device, a micro, parallel-plate rheometer, which allows both types of velocity controls to exist on the opposing flat interface to the driven plate. The present work has illustrated recovery of linear and nonlinear viscoelastic parameters as well as predictions of the onset of nonlinear effects at threshold values of the imposed strain from the driven plate. In future work, we will apply these modeling tools to experiments on biological liquids.

The last topic we discussed is the numerical analysis for viscoelastic fluid flow, which is important to the prediction of fluid transport for the lung mucus layer. We present detailed numerical analysis on the model system incorporating Oldroyd-B constitutive law. With the analysis of the underlying physical and mathematical interpretation of general numerical methods, we point out that the most plausible reason for the breakdown of convergence is the violation of the incompressibility during the update

of elastic stress of numerical procedures. Therefore the new double-projection method is proposed. The method is based on the decomposition of the stress tensor  $\boldsymbol{\tau}$ , and the separation of  $\boldsymbol{\tau}$  into two parts serves to eliminate from consideration the divergence free part. The force-carrying part of the decomposition is the one of interest. The key aspect of the double-projection method is to extract from this force-carrying part the elastic displacement. Then the elastic displacement is corrected to eliminate longitudinal modes. The extension of the double-projection to the FENE-P dumbbell model is also discussed. By applying expansion approximation to the stress in the FENE-P dumbbell, we can update the nonlinear stress and corresponding deformation field iteratively, and again we can maintain the incompressible condition satisfied. The implementation and application details of our new method will be our future work.

# Bibliography

- [1] F.T. Adler, W.M. Sawyer, and John D. Ferry. Propagation of transverse waves in viscoelastic media. *J. Appl. Phys.*, 20:1036–1041, 1949.
- [2] B. J. Alder and T. E. Wainwright. Velocity autocorrelations for hard spheres. *Phys. Rev. Lett.*, 18:988, 1967.
- [3] R. C. Armstrong and S. Ishikawa. A rheological equation of state for dilute solutions of nearly-hookean dumbbells. *J. Rheol.*, 24:143–165, 1980.
- [4] A.A. Barnes, J.F. Hutton, and K. Walters. *An introduction to rheology*. Elsevier, 1989.
- [5] J. B. Bell, P. Colella, and H.M. Glaz. A second order projection method for the incompressible navier-stokes equations. *J. Comput. Phys.*, 85:257–283, 1989.
- [6] P. G. Bhat, D. R. Flanagan, and M. D. Donovan. Drug diffusion through cystic fibrotic mucus: Steady-state permeation, rheologic properties, and glycoprotein morphology. *Journal of Pharmaceutical Sciences*, 85:624–630, 1996.
- [7] R. B. Bird, R. C. Armstrong, and O. Hassager. *Dynamics of Polymeric Liquids Volume 1: Fluid Mechanics*. John Wiley, 1987.
- [8] R. B. Bird, C. F. Curtiss, R. C. Armstrong, and O. Hassager. *Dynamics of Polymeric Liquids Volume 2: Kinetic Theory*. John Wiley, 1987.
- [9] Jean Pierre Boon and Sidney Yip. *Molecular Hydrodynamics*. McGraw-Hill, 1980.
- [10] G. Bossis, B. Quentrec, and J. P. Boon. Brownian dynamics and the fluctuation-dissipation theorem. *Molecular Phys.*, 45:191–196, 1982.
- [11] Peter J Brockwell and Richard A Davis. *Time Series: Theory and Methods*. Springer, New York, second edition, 1991.
- [12] Jonathon Celli, Brian Gregor, Bradley Turner, Nezam Afdhal, Rama Bansil, and Shyamsunder Erramilli. Viscoelastic properties and dynamics of porcine gastric mucin. *Biomacromolecules*, 6:1329–1333, 2005.
- [13] P. M. Chaikin and T. C. Lubensky. *Principles of Condensed Matter Physics*. Cambridge University Press, 1995.
- [14] A. J. Chorin and J. E. Marsden. *A Mathematical Introduction to Fluid Mechanics*. Springer-Verlag, third edition, 1992.

- [15] A.J. Chorin. Numerical solutions of the navier-stokes equations. *Math. Comp.*, 22:745–762, 1966.
- [16] John C. Crocker, M.T. Valentine, Eric R. Weeks, T. Gisler, P.D. Kaplan, A. G. Yodh, and D. A. Weitz. Two-point microrheology of inhomogeneous soft materials. *Phys. Rev. Lett.*, 85:888(4), 2000.
- [17] Michelle Dawson, Denis Wirtz, and Justin Hanes. Enhanced viscoelasticity of human cystic fibrotic sputum correlates with increasing microheterogeneity in particle transport. *The Journal of Biological Chemistry*, 278(50):50393–50401, 2003.
- [18] P. G. de Gennes. *Scaling Concepts in Polymer Physics*. Cornell University Press, Ithaca, NY, 1979.
- [19] R. Denton, M. Litt, and S. H. Hwang. Chemical engineering aspects of obstructive lung disease. In *Chemical Engineering Process, Symposium Series*, volume 62, pages 12–18, 1966.
- [20] M. Doi and S.F. Edwards. *The Theory of Polymer Physics*. Oxford University Press, 1986.
- [21] Weinan E and Jianguo Liu. Gauge finite element method for incompressible flow. *Int. J. Num. Meth. Fluids*, 34:701–710, 2000.
- [22] Weinan E and Jianguo Liu. Gauge method for viscous incompressible flow. *Comm. Math. Sci.*, 1:317–332, 2003.
- [23] J. D. Ferry. Studies of the mechanical properties of substances of high molecular weight i. a photoelastic method for study of transverse vibrations in gels. *Rev. Sci. Inst.*, 12:79–82, 1941.
- [24] J. D. Ferry. *Viscoelastic Properties of Polymers*. Wiley, third edition, 1994.
- [25] J. D. Ferry, W. M. Sawyer, and J. N. Ashworth. Behavior of concentrated polymer solutions under periodic stresses. *Journal of Polymer Science*, 2:593–611, 1947.
- [26] John Fricks, Lingxing Yao, Timothy C. Elston, and M. Gregory Forest. Time-domain methods for passive microrheology and anomalous diffusive transport in soft matter. *Submitted to SIAM J. Appl. Math.*, 2007.
- [27] G. Gardner, A. C. Harvey, and G. D. A. Phillips. An algorithm for exact maximum likelihood estimation of autoregressive-moving average models by means of kalman filtering. *Applied Statistics*, 29(3):311–322, 1980.
- [28] F. Gittes, B. Schnurr, P.D. Olmsted, F.C. MacKintosh, and C.F. Schmidt. Microscopic viscoelasticity: shear moduli of soft materials determined from thermal fluctuations. *Phys. Rev. Lett.*, 79:3286–3289, 1997.

- [29] Jean Pierre Hansen and Ian R. McDonald. *Theory of simple liquids*. Academic Press, 1986.
- [30] A. C. Harvey and G. D. A. Phillips. Maximum likelihood estimation of regression models with autoregressive-moving average distributions. *Biometrika*, 66(1):49–58, 1979.
- [31] Andrew C. Harvey. *Forecasting, structural time series models and the Kalman filter*. Cambridge University Press, Cambridge, 1989.
- [32] <http://www.amath.unc.edu/Faculty/mitran/research/viscelas/shear1d.shtml>.
- [33] <http://www.cs.unc.edu/Research/nano/vl/vlindex.html>.
- [34] R.R. Huilgol and N. Phan-Thien. *Fluid mechanics of viscoelasticity: general principles, constitutive modelling, analytical and numerical techniques*. Elsevier Science, 1997.
- [35] Daniel D. Joseph. *Fluid Dynamics of Viscoelastic Liquids*. Springer-Verlag, 1990.
- [36] J. Van Kan. A second-order accurate pressure-correction scheme for viscous incompressible flow. *SIAM J. Sci. Comput.*, 3:870–891, 1986.
- [37] D. E. Knuth. *Literate Programming*. CSLI Lecture Notes. Stanford, 1992.
- [38] J. Kocevar-Nared and J. Smid-Korbar. Evaluation of mucin viscoelastic behavior. In *World Meeting on Pharmaceuticals, Biopharmaceutics and Pharmaceutical Technology, 1st, Budapest*, pages 88–89, May 1995.
- [39] S. C. Kou and X. S. Xie. Generalized langevin equation with fractional gaussian noise: Subdiffusion with in a single protein molecule. *Phys. Rev. Lett.*, 93(18), October 2004.
- [40] R. Kubo. The fluctuation-dissipation theorem. *Rep. Prog. Phys. Part I*, 29:255, 1966.
- [41] R. Kubo. *Statistical Physics II : Nonequilibrium Statistical Mechanics*. Springer, 2nd edition, 1985.
- [42] Ryogo Kubo. Statistical-mechanical theory of irreversible processes. i. general theory and simple applications to magnetic and conduction problems. *J. Phys. Soc. Japan*, 12:570, 1957.
- [43] Samuel K. Lai, D. Elizabeth O’Hanlon, Suzanne Harrold, Stan T. Man, Ying-Ying Wang, Richard Cone, and Justin Hanes. Rapid transport of large polymeric nanoparticles in fresh undiluted human mucus. *PNAS*, 104:1482–1487, 2007.
- [44] L. D. Landau and E. M. Lifshitz. *Theory of elasticity*. Pergamon Press, third edition, 1986.

- [45] R. G. Larson. *Constitutive Equations for Polymer Melts and Solutions*. Butterworth-Heinemann, 1988.
- [46] R. G. Larson. *The Structure and Rheology of Complex Fluids*. Oxford University Press, 1998.
- [47] R. J. LeVeque. Wave propagation algorithms for multi-dimensional hyperbolic systems. *J. Comp. Phys.*, 131:327–353, 1997.
- [48] R. J. LeVeque. *Finite Volume Methods for Hyperbolic Problems*. Cambridge University Press, 2002.
- [49] A. J. Levine and T. C. Lubensky. One- and two-particle microrheology. *Phys. Rev. Lett.*, 85:1774(4), 2000.
- [50] Alex J. Levine and T. C. Lubensky. Response function of a sphere in a viscoelastic two-fluid medium. *Phys. Rev. E*, 63(4):041510, 2001.
- [51] M. Litt. Physicochemical properties of trancheobronchial mucus secretions. In *Saliva Dent. Caries Proc. Workshop*, pages 175–181, 1979.
- [52] M. Litt, M. A. Khan, and D. P. Wolf. Mucus rheology: relation to structure and function. *Biorheology*, 13:37–48, 1976.
- [53] R. J. Lutz, M. Litt, and L. W. Chakrin. Physical-chemical factors in mucus rheology. In *Rheol. Biol. Syst., Proc. Symp.*, pages 119–157, 1973.
- [54] Ch. W. Macosko. *Rheology: Principles, Measurements, and Applications*. Wiley, 1994.
- [55] C. Marriott, C. K. Chung, and M. Litt. Changes in gel properties of tracheal mucus induced by divalent cations. *Biorheology*, 16:331–337, 1979.
- [56] Thomas G. Mason. Estimating the viscoelastic moduli of complex fluids using the generalized stokes-einstein equation. *Rheologica Acta*, 39:371–378, 2000.
- [57] Thomas G. Mason, Hu Gang, and D.A. Weitz. Diffusing wave spectroscopy measurements of viscoelasticity of complex fluids. *Journal of the Optical Society of America A*, 14:139–149, 1997.
- [58] Thomas G. Mason and D.A. Weitz. Optical measurements of the linear viscoelastic moduli of complex fluids. *Phys. Rev. Lett.*, 74:1250–1253, 1995.
- [59] W. Min, G. Luo, B. J. Cherayil, S. C. Kou, and X. Sunney Xie. Observation of a power-law memory kernel for fluctuations within a single protein molecule. *Phys. Rev. Lett.*, 94(19), May 2005.

- [60] Sorin M. Mitran, M. Gregory Forest, Lingxing Yao, Brandon Lindley, and David B. Hill. Linear and nonlinear viscoelastic shear wave theory for small volume microbead rheology. *Submitted to JNNFM*, 2007.
- [61] Sorin M. Mitran and Lingxing Yao. Double projection method on computation of viscoelastic flow. *In preparation*, 2007.
- [62] Hazime Mori. A continued-fraction representation of the time-correlation functions. *Progr. Theo. Phys.*, 34:399, 1965.
- [63] Hazime Mori. Transport, collective motion and brownian motion. *Progr. Theo. Phys.*, 33:423, 1965.
- [64] S.M.F.D. Syed Mustapha and T.N. Phillips. A dynamic nonlinear regression method for the determination of the discrete relaxation spectrum. *J. Phys. D: Appl. Phys.*, 33:1219–1229, 2000.
- [65] J. T. Oden and J. N. Reddy. *Variational Methods in Theoretical Mechanics*. Springer, 1976.
- [66] Bernt Øksendal. *Stochastic Differential Equations*. Springer, New York, 5 edition, 1998.
- [67] R.G. Owens and T.N. Phillips. *Computational Rheology*. World Scientific, 2002.
- [68] Z. E. Puchelle, J. M. Zahm, C. Duvivier, J. Jacquot, and D. Quemada. Elastothixotropic properties of bronchial mucus and polymer analogs i- experimental result. *Biorheology*, 22:415–423, 1985.
- [69] P.E. Rouse. A theory of the linear viscoelastic properties of dilute solutions of coiling polymers. *J. Chem. Phys.*, 21:1272–1280, 1953.
- [70] M. Rubinstein and R. Colby. *Polymer Physics*. Oxford University Press, 2003.
- [71] Hermann Schlichting. *Boundary layer thoory*. McGraw-Hill, 1960.
- [72] F.G. Schmidt, F. Ziemann, and E. Sackmann. Shear field mapping in actin networks by using magnetic tweezers. *Eur. Biophys. J.*, 24:348, 1996.
- [73] K.S. Schweizer. Microscopic theory of the dynamics of polymeric liquids: General formulation of a mode mode coupling approach. *J. Chem. Phys.*, 91:5802–5821, 1989.
- [74] Robert H. Shumway and David S. Stoffer. *Time Series Analysis and Its Applications with R Examples*. Springer, 2006.
- [75] D. E. Smith and C. B. Harris. Generalized brownian dynamics i. *Journal of Chemical Physics*, 92(2):1304–, 1990.



- [76] D. E. Smith and C. B. Harris. Generalized brownian dynamics ii. *Journal of Chemical Physics*, 92(2):1312–1319, 1990.
- [77] D. J. Smith, E. A. Gaffney, and J. R. Blake. A viscoelastic traction layer model of mucus-ciliary transport. *Bull. Math. Biol.*, 69:289–327, 2006.
- [78] Richard L Smith. Time series. Course Notes, May 1999.
- [79] T. M. Squires and J. F. Brady. A simple paradigm for active and nonlinear microrheology. *Physics of Fluids*, 17:073101, 2005.
- [80] Michael E. Taylor. *Measure Theory and Integration*. Class notes, 2005.
- [81] R. Temam. *Navier-Stokes Equations. Theory and Numerical Analysis*. North Holland, 1984.
- [82] D. Trebotich, P. Colella, and G.H. Miller. A stable and convergent scheme for viscoelastic flow in contraction channels. *J. Comp. Phys.*, 205:315–342, 2005.
- [83] Minzhong Wang. Decomposition of symmetric tensor and its application. *Applied Mathematics and Mechanics*, 5:1813–1816, 1984.
- [84] David Williams. *Probability with martingales*. Cambridge University Press, 1991.
- [85] F. Brochard Wyart and P.G. de Gennes. Viscosity at small scales in polymer melts. *European Phys. Journal E*, 1:93–97, 2000.
- [86] S.C. Xue, N. Phan-Thien, and R.I. Tanner. Three dimensional numerical simulations of viscoelastic flows through planar contractions. *J. Non-Newtonian Fluid Mech.*, 74:195–245, 1998.
- [87] K.S. Zaner and P.A. Valberg. Viscoelasticity of f-actin measured with magnetic microparticles. *Journal of Cell Biology*, 109:2233–2243, 1989.
- [88] F. Ziemann, J. Radler, and E. Sackmann. Local measurements of viscoelastic moduli of entangled actin networks using an oscillating magnetic bead microrheometer. *Biophys. J.*, 66:2210–2216, 1994.
- [89] B. H. Zimm. Dynamics of polymer molecules in dilute solution: Viscoelasticity, flow birefringence and dielectric loss. *J. Chem. Phys.*, 24:269–278, 1956.
- [90] R. Zwanzig. Ensemble method in the theory of irreversibility. *J. Chem. Phys.*, 33:1338–1341, 1960.
- [91] R. Zwanzig. *Statistical Mechanics of Irreversibility*. Lectures in Theoretical Physics. Interscience Publishers, 1961.
- [92] R. Zwanzig. *Nonequilibrium Statistical Mechanics*. Oxford University Press, 2001.
- [93] R. Zwanzig and M. Bixon. Hydrodynamic theory of the velocity correlation function. *Phys. Rev. A*, 2:2005, 1970.